Master of Science Thesis

The Effect of Nozzle Length and Exhaust Plume on Transonic and Supersonic Axisymmetric Base Flows

An Experimental Study

Qais Payanda

November 15, 2017

Aerodynamics

TU Delft

Faculty of Aerospace Engineering

Delft University of Technology

The Effect of Nozzle Length and Exhaust Plume on Transonic and Supersonic Axisymmetric Base Flows

An Experimental Study

Master of Science Thesis

For obtaining the degree of Master of Science in Aerospace Engineering
at Delft University of Technology

Qais Payanda

November 15, 2017

Faculty of Aerospace Engineering · Delft University of Technology

Delft University of Technology

DELFT UNIVERSITY OF TECHNOLOGY
DEPARTMENT OF AERODYNAMICS

The undersigned hereby certify that they have read and recommend to the Faculty of Aerospace Engineering for acceptance the thesis entitled **"The Effect of Nozzle Length and Exhaust Plume on Transonic and Supersonic Axisymmetric Base Flows"** by **Qais Payanda** in fulfillment of the requirements for the degree of **Master of Science**.

Dated: November 15, 2017

Supervisors:

Dr. ir. B.W. van Oudheusden

Dr. ir. F.F.J. Schrijer

Ir. P.L. van Gent

Reader:

Dr .ir. G.E. Elsinga

An experiment is a question which science poses to Nature, and a measurement is the recording of Natures answer.

Max Planck, (1858-1947)

Acknowledgments

This thesis work marks the completion of my MSc studies at the Delft University of Technology and the end of twelve months of research on the effect of nozzle length and exhaust plume on the flow topology and mean pressure distribution of axisymmetric base flows at transonic and supersonic flows. It has been a long journey with ups and downs and a period of intense learning for me. Its now time to move to the next stage, but before doing that I would like to acknowledge here all the people who have supported, encouraged and helped me throughout this period.

Firstly, I would like to express my sincere thanks to my amazing daily supervisors, Dr.ir. Bas van Oudheusden, Dr.ir. Ferry Schrijer and Ir. Paul van Gent for their valuable instructions, inputs and constructive suggestions throughout my thesis and also for their encouragement and moral support during difficult times. Also I would like to offer my thanks to Dr.ir. Gerrit Elsinga for being in my committee and going through my thesis report. I also want to thank the technical staff of the high speed lab, Peter Duyndam, Frits Donker Duyvis, Dennis Bruikman, Nico van Beek and Eric de Keizer for their valuable technical support throughout my experiments. Special thanks to experimental team and incredible friends, Nick, Roberto, Summit and Yorin, with whom I spent the most joyful and challenging moments. Also I would like to express my thanks to the colleagues from Basement, Jordi, Ka Hin, Arun, Lluis, Sumedh, Werner, Jaydeep, Arti and many others. Outside of the basement, I would like to thank my incredible friends Amrien, Ibrahim, Hamza, Nabil, Serhat, Talha and Yama, with whom I spent most of my studies at the Aerospace faculty.

Finally, I would like to take this opportunity to sincerely thank my dear father, Faiz and my lovely mother, Wasima for providing me with love, prayers, continuous support and encouragement. Everything that I have and achieved up to this point would not have been possible without their effort. To them I dedicate this thesis. Special thanks to my lovely sister, Khatera and awesome brothers, Ismael and Ishak, my niece Wahida and her family and my uncles family for their love, support and encouragement. To end this, I would like to thank all of them in my mother tongue...

پدرجان ومادر جان عزیز و مهربان، خواهر و برادران عزیز و همه اعضای فامیل، یک جهان تشکر از حمایت، تشویق و دعا شما

قیس محمد پاینده

Abstract

A combined PIV and Schlieren measurements have been carried out in the transonic-supersonic wind tunnel (TST-27) to investigate the effect of exhaust plume and the variation in nozzle length on the flow topology and mean pressure distribution on the wake of axisymmetric backward facing step model at freestream Mach numbers of $M_\infty = 0.76$ and $M_\infty = 2.20$, respectively. Four different nozzle length configurations with and without the presence of a supersonic exhaust plume have been tested. Testing with different nozzle length configuration resulted in flow cases where the shear layer reattachment occurred on the nozzle (solid reattachment), on the flow downstream of the nozzle (fluidic reattachment), and intermittently on the nozzle and on the flow (hybrid reattachment).

A qualitative identification of the effect of exhaust plume and the variation in nozzle length on the flow topology on the wake of axisymmetric backward facing step model, at the above mentioned conditions, is successfully described by means of Schlieren visualization. The topological flow features for the subsonic and supersonic flow cases has been identified (i.e shock waves, Prandtl-Meyer expansion fan, boundary layer, separated shear layer, recompression and plume shocks). On the other hand, a quantitative identification of the effect of exhaust plume and the variation in nozzle length on the flow topology and mean pressure distribution on the wake of axisymmetric backward facing step model, at the above mentioned conditions, is successfully done by means of planar PIV. The planar PIV measurements in the wake region of the model provided detailed information of the mean flow field properties (i.e mean velocity, turbulent kinetic energy, Reynolds stresses and reverse flow). Using these mean flow field properties data, the mean pressure distribution is reconstructed based on the momentum equation.

It has been shown that an increase in nozzle length and the presence of an exhaust plume caused an increase in mean reattachment length at $M_\infty = 2.20$, while no significant change in mean reattachment length was noticed at $M_\infty = 0.76$. Significantly higher turbulent kinetic energy levels have been observed for $L/D = 1.8$ cases where solid reattachment occurred, at $M_\infty = 2.20$. In contrast to supersonic flow cases, the flow cases at $M_\infty = 0.76$ showed a significantly lower turbulent kinetic energy levels. Comparisons of flow cases with a long nozzle without a plume and flow cases with a short nozzle but with a plume suggest that the presence of the plume cannot accurately be modeled by replacing the plume with a solid geometry. From the pressure results it is observed that the location of the low-pressure region downstream of the base remained unchanged for different flow cases with and without exhaust

plume and for different nozzle lengths. Furthermore, it has been shown that an increase in nozzle length leads to higher local pressure at the nozzle exit and hence results in a less under-expanded for the supersonic flow cases or more over-expanded plume for the subsonic cases.

Table of Contents

List of Figures

List of Tables

Nomenclature

Abbreviations

2D	Two-Dimension
BFS	Backward facing step
BL	Boundary layer
CCD	Charge-coupled device
CFD	Computational fluid dynamics
CMOS	Complementary metaloxidesemiconductor
ESA	European space agency
EPR	Exit pressure ratio
FESTIP	Future European Space Transportation Investigation Program
FOV	Field of view
NASA	National Aeronautics and Space Administration
Nd:YAG	Neodymium-doped yttrium aluminium garnet
Nd:YLF	Neodymium-doped yttrium lithium fluoride
NPR	Nozzle pressure ratio
NS	Navier-Stokes
PIV	Particle image velocimetry
PME	Prandtl-Meyer expansion
PSP	Pressure sensitive paint
RMS	Root mean square
RFP	Reverse flow probability
SW	Shock wave
TKE	Turbulent kinetic energy
TST	Transonic supersonic tunnel
ZDES	Zonal detached eddy simulation

Latin Symbols

Symbol	Discription	Unit
A	Area	$[m^2]$
C_p	Pressure coefficient	$[-]$
D	Main body diameter	$[mm]$
L	Nozzle length	$[mm]$
M	Mach number	$[-]$
M_c	Convective Mach number	$[-]$
M	Magnification factor	$[-]$
N	Ensemble size	$[-]$
R	Specific gas constant	$[J/(kg \cdot K)]$
Re_D	Main body diameter based Reynolds number	$[-]$
Re_h	Step height Reynolds number	$[-]$
S	Sutherland's constant	$[-]$
Sr_L	Vortex shedding frequency	$[Hz]$
S_k	Stokes number	$[-]$
T	Temperature	$[K]$
U	Velocity	$[m \cdot s^{-1}]$
W	Window size	$[pixel]$
a	Acceleration	$[m \cdot s^{-2}]$
a	Speed of sound	$[m \cdot s^{-1}]$
a	Lapse rate	$[K \cdot m^{-1}]$
c	Speed of light	$[m \cdot s^{-1}]$
d	Focal distance	$[mm]$
d	diameter	$[mm]$
f	Frequency	$[Hz]$
f	Focal length	$[mm]$
$f_\#$	f-stop number	$[-]$
h	Step height	$[mm]$
g	Gravitational acceleration	$[m \cdot s^{-2}]$
k	Gladstone-Dale constant	$[-]$
n	Refractive index	$[-]$
p	Pressure	$[bar]$
r	Vortex radius	$[mm]$
s	Cost function	$[-]$
t	Time	$[sec]$
u	Streamwise velocity component	$[m \cdot s^{-1}]$
v	Radial velocity component	$[m \cdot s^{-1}]$
x	Streamwise distance	$[mm]$
y	Radial distance	$[mm]$

Greek Symbols

Symbol	Discription	Unit
γ	Specific heat ratio	$[-]$
δ	Boundary layer thickness	$[mm]$
ε	Uncertainty	$[-]$
κ	Image resolution	$[pix/mm]$
λ	Wavelength	$[m]$
ρ	Denisty	$[kg \cdot m^{-3}]$
μ	Dynamic viscosity	$[kg \cdot m^{-1} \cdot s^{-1}]$
μ	Mach angle	$[deg.]$
τ	Particle response time	$[\mu s]$

Subscripts

Symbol	Discription
e	Nozzle exit
0	Total
∞	Freestream
D	Main body diameter
cc	Cross-correletion
f	Fluid
p	Particle
$conv$	Convective
sr	Spatial resolution
R	Reattachmnent
r	Reattachmnent
p	Pressure
ref	Reference
t	Throat
$diff$	Diffraction

Superscripts

Symbol	Discription
$'$	Fluctuating
$-$	Mean
$*$	Nozzle throat

Chapter 1

Introduction

The investigation of the interaction between the base flow and exhaust plume is of fundamental importance for the aero-thermodynamic design of the next generation launch vehicles. One of the critical areas in the design of the launch vehicle is the quantification of pressure and thermal loads that occur as result of the interaction between the base flow and exhaust plume in the base region during ascent. Figure 1.1 show atmospheric ascent of Ariane 5 and Delta

Figure 1.1: Araine 5 (left) and Delta IV Heavy (right) during launch. Courtesy of *ESA* and *U.S. Air Force*

IV Heavy launcher. During the atmospheric ascent, the base region of a launch vehicle is identified by a large separation region due to an abrupt change in geometry. This separated region, where the pressure is relatively low, suffer from high base drag, which makes up

a significant part of the overall drag of the vehicle. Moreover, the inherent unsteadiness of the flow generates fluctuating pressure-induced side-loads on the external nozzle structure. In particular during the transonic flight regime, the low-frequency components of these oscillating side-loads may excite a structural response (*transonic buffeting*) and lead to structural failure. Also, the entrainment of the hot exhaust plume gasses in the recirculation zone may result in significant thermal loads on the external surface of the nozzle. In the view of the above, the quantification of pressure and thermal loads in the base region of launcher is relevant for the development of a reliable and efficient launch vehicle.

Since pressure and thermal loads are difficult to measure during a real life launch, quantification is commonly done using numerical simulation techniques and by means of wind tunnel experiments. A generic axisymmetric Backward Facing Step (BFS) geometry is commonly used as a simplification of a launch vehicle base to investigate the development of complex flow phenomena in the base region. Even though a number of past studies used scaled launcher model for the investigation, such as e.g. Schrijer et al. (2011), Reijasse and Delery (1994), Hannemann et al. (2011), a generic geometry is more commonly used in the context of academic research for reasons of simplicity. This generic geometry consist of a conical forebody, a cylindrical main body and a cylindrical afterbody that represent the main stage and the nozzle of a typical launch vehicle, respectively.

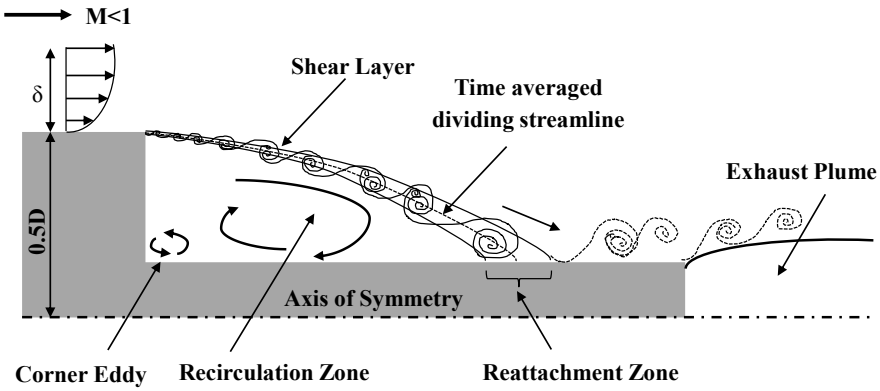

Figure 1.2: Schematic of mean flow topology of a subsonic BFS. Adapted from Driver et al. (1987)

As a result of sudden change in geometry, the external flow past the edge of the cylindrical main body starts to separate (see Figure 1.2). As result, a recirculation region is formed which is divided from the external flow by a shear layer that emanates from the edge. Depending on the length of the cylindrical afterbody (nozzle), the reattachment of the separated shear layer occur on the nozzle, on the flow downstream or on both the nozzle and on the flow. The occurence of these types of reattachments are reffered by Deprés et al. (2004) as solid, fluidic and hybrid reattachment, respectively. The introduction of an exhaust plume at the end of the nozzle has two significant impacts on the flow field in the base region. Firstly, the presence of exhaust plume leads to displacement of the outer flow as a result of the blockage and secondly, entrainment at the plume boundary causes the acceleration of the outer flow towards the base (Bergman, 1970). In addition, the blockage due to the presence of an exhaust plume result in an increase of pressure at the base whereas the entertainment

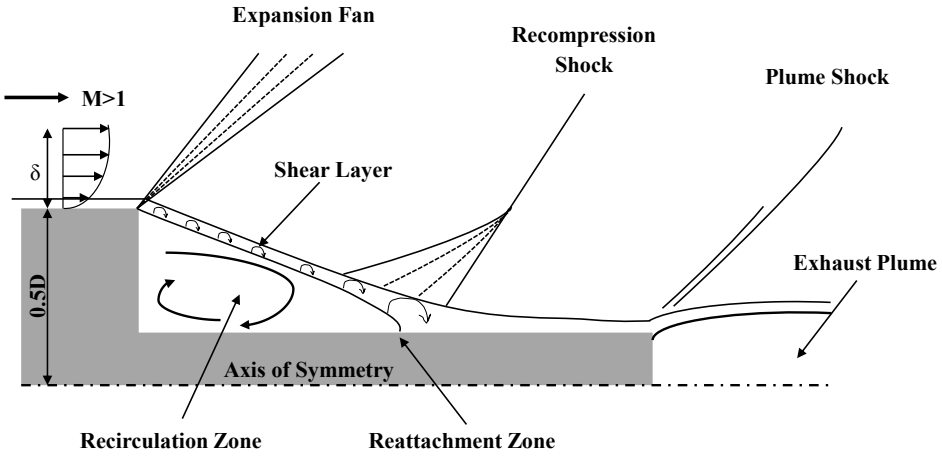

Figure 1.3: Schematic flow topology of supersonic BFS. Adapted from Loth et al. (1992) and Bannink and Schoones (1998)

tends to decrease it (Bergman, 1970). Furthermore, the effect of exhaust plume on the flow field depends on the reattachment location of the separated shear layer. This effect can be small for the solid reattachment, but it can be great if the shear layer reattachment is fluidic (Deprés et al., 2004).

The flight regime during ascent of a typical launch vehicle always covers subsonic, transonic, supersonic, and hypersonic flow velocities. At the transition from subsonic to supersonic flows, a Prandtl-Meyer expansion (PME) fan is developed at the edge of the cylindrical main body (see Figure 1.3). Shock waves are developed at the reattachment location due to the deflection of the flow in the direction of the freestream. Due to the presence of exhaust plume, additional shock wave is formed, which can be attributed to the displacement of the flow by an exhaust plume. As the flow velocity increase from subsonic to supersonic regimes, the ambient pressure and temperature decreases and the over-expanded exhaust plume becomes under-expanded.

Numerous experimental and numerical studies on the base flows has been done in the past that aimed to identify the driving mechanisms of the flow dynamics developing in the wake region of a BFS and to quantify the corresponding pressure loads. Most of these studies investigated base flows at the freestream Mach number of $M_\infty = 0.7$ (e.g. Deprés et al. (2004), Weiss et al. (2009), Hannemann et al. (2011), Scharnowski et al. (2015), Schrijer et al. (2014)) while others aimed at studying supersonic freestream Mach numbers (e.g. Scarano et al. (2005), Deck et al. (2007), Janssen and Dutton (2004), Statnikov et al. (2016)). A small number of these studies investigated both subsonic and supersonic flow cases (e.g. Bitter et al. (2011), Scharnowski et al. (2016a), Statnikov et al. (2016)). For quantification of the (fluctuating) pressure loads on the model surface, previous experimental studies used pressure transducers, which is unable to measure pressure in the flow away from the surface of the model. A number of studies employed PIV which provides instantaneous velocity vector measurements in a cross-section of a flow and also it is a whole-flow-field technique. PIV technique has been employed to study the unsteady nature of the flow (Schrijer et al. (2011), Scharnowski et al. (2015), Schrijer et al. (2014), Bitter et al. (2011)), to acquire mean flow field and Reynolds

stress distributions (Scharnowski et al., 2015) and to investigate the effect of control devices (Scharnowski et al. (2015), Schrijer et al. (2010)). Furthermore, it has been also used in base flow investiagtion with presence of an exhaust plume (e.g Scarano et al. (2005), Scharnowski et al. (2016a)).

PIV technique is good alternative for pressure transducers, however it does not provide direct measurement of the pressure in the flow. Pressure reconstruction in the wake of an axisymmetric BFS at subsonic and supersonic flow by means of PIV has been largely unexplored, with the exception of studies performed by Blinde et al. (2014) and van Gent et al. (2017). The pressure field is reconstructed by solving the Navier-Stokes (NS) equation where the velocity and acceleration are known variables from PIV measurement. The evaluation of instantaneous pressure field is done by means of time-resolved PIV measurements whereas the mean pressure field is determined from ensembles of uncorrelated PIV measurements (van Oudheusden, 2013). Using PIV technique is particularly beneficial when the model geometry introduces spatial limitations for the installation of pressure transducers on the surface.

In the view of the above, the present thesis will aim to investigate the effect of nozzle varying length and presence of an exhaust plume on subsonic and supersonic axisymmetric base flow by means of PIV. In particular, attention will be paid to the impact of these changes on the mean pressure distribution and unsteadiness.

1.1 Research Objectives & Methodology

The overall research goal of the present thesis is to investigate the effect of varying nozzle length and presence of an exhaust plume on the on the flow topology and mean pressure distribution on the wake of axisymmetric BFS at subsonic and supersonic flows. To achieve this goal, the research is divided into following objectives:

- To characterize the flow topology in the wake of axisymmetric BFS at subsonic and supersonic flows, for flow cases with and without exhaust plumes and for different nozzle lengths by means of planar (2D) PIV
- To carry out mean pressure reconstruction in the wake of axisymmetric BFS at subsonic and supersonic flows, for flow cases with and without exhaust plumes and for different nozzle lengths using PIV data
- To determine the effect of varying nozzle length and presence of exhaust plume on the flow topology and mean pressure distribution on the wake of axisymmetric BFS at subsonic and supersonic flows

In order to accomplish these objectives a wind tunnel experiment is carried out in the transonic-supersonic wind tunnel (TST-27) of the High Speed Lab at the TU Delft, on a generic rocket model in subsonic and supersonic flows. This model is a modified version of

the same model as used within the framework of FESTIP (Future European Space Transportation Investigation Program) (Hirschel, 1996). The afterbody of the model contains a nozzle that generates a (non-heated) exhaust plume. For the present study only the length of the nozzle is varied and not the step height of the base. Based on study performed by Gentile et al. (2016), an increase in step height (or nozzle diameter) result in a gradual shrinking of the recirculation region and upstream movement of the reattachment point. Planar PIV and Schlieren techniques are employed to investigate the wake region of an axisymmetric BFS in subsonic and supersonic flows. This will allow to characterize in great detail the flow topology and mean pressure distribution in the wake of an axisymmetric BFS and identify the effect of nozzle and exhaust plume on the flow topology and mean pressure distribution.

1.2 Thesis Outline

The structure of present thesis is as follow: In Chapter 2, the characteristic features of the BFS flows relevant for the present study are introduced. The basic principles of the measurement and pressure reconstruction techniques used are briefly outlined in Chapter 3, while practical matters related to experimental apparatus and setup for the present investigation are presented in Chapter 4. Chapter 5 is dedicated to the discussion of the experimental results. Finally, Chapter 6 presents major conclusions of thesis and outlines recommendations towards future works.

Chapter 2

Base Flow Characteristics

During atmospheric ascent of a launch vehicle, such as Ariane 5, complex flow phenomena develop at its base region (Figure 2.1). An understanding of the development of these complex flow phenomena is essential for the design of a reliable and efficient launch vehicle. As such, this chapter aims to familiarize the reader with the characteristic features of the base flows. Also, this chapter briefly reviews the effect of nozzle length and presence of an exhaust plume on high-subsonic and supersonic base flows.

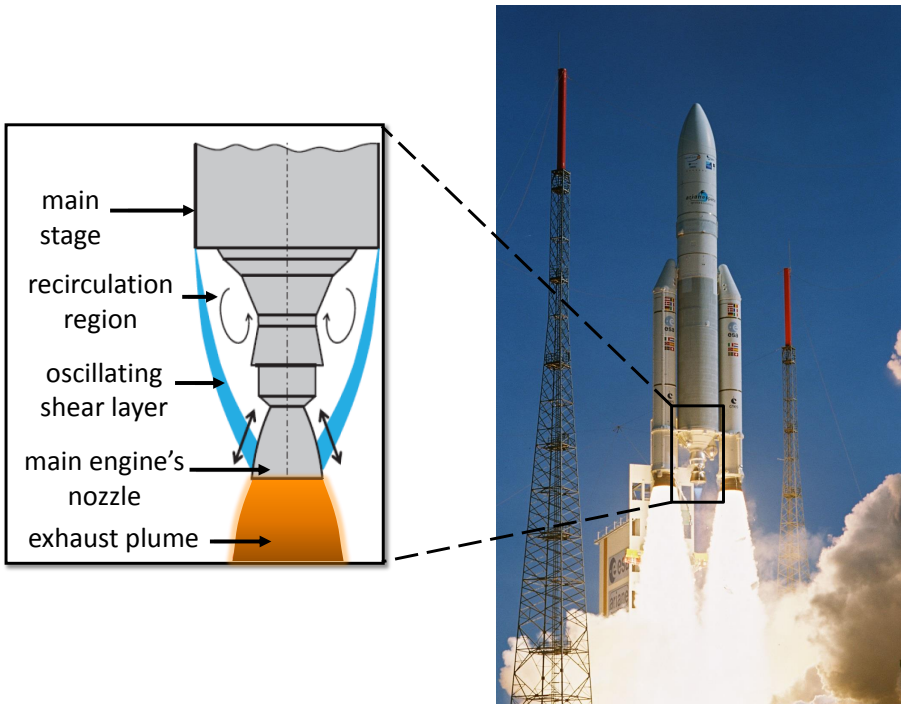

Figure 2.1: Development of complex flow phenomena during ascent of Ariane 5 (Scharnowski et al. (2016a), courtesy of *ESA*)

2.1 Base Flow Geometry

Figure 2.2(a) shows the base region of cryogenic main core stage of Ariane 5, which consist of the main stage and the nozzle. To study and understand the complex flow phenomena that develop in this region, the base geometry of Ariane 5 is commonly simplified to a cylindrical main body and a cylindrical afterbody, as shown in Figure 2.2(b). In literature, this simplified geometry, which resembles the base region of an actual Ariane 5 launcher, is typically referred to as the Backward Facing Step (BFS).

Many experimental and numerical studies have been performed on BFS geometry to investigate the characteristic flow features that also develop in the base region of a typical launcher such as Ariane 5. Although a number of studies investigated realistic scale models (e.g. Reijasse and Delery (1994) and Schrijer et al. (2011)), using such a generic geometry is a more common practice in the context of academic research. Many studies reported in the liter-

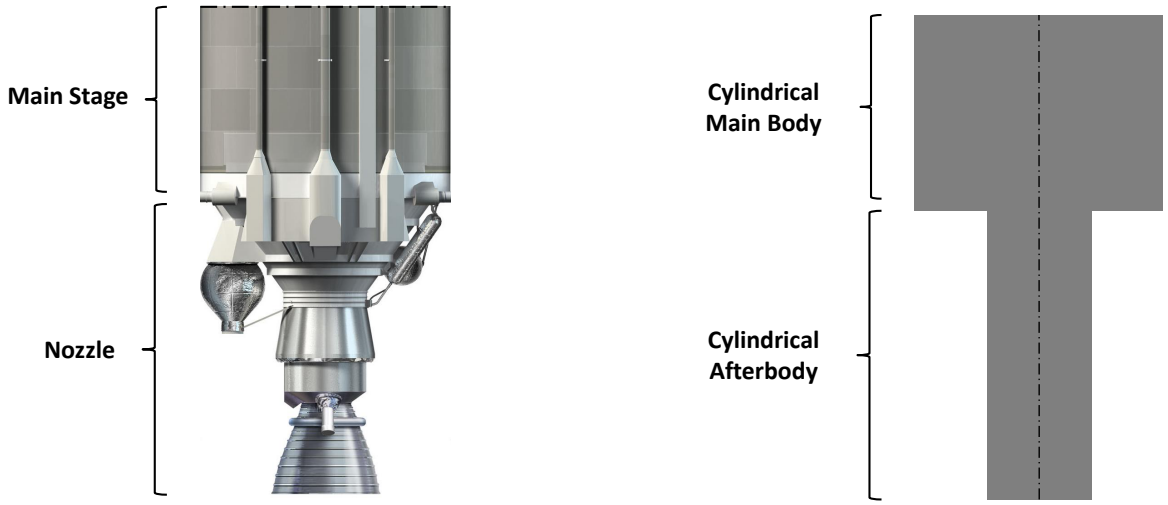

(a) Ariane 5 cryogenic main stage and the nozzle. Courtesy of *ESA*

(b) Simplified geometry of Ariane 5 base region

Figure 2.2: Actual and simplified base geometry of Ariane 5

ature are performed on the two-dimensional BFS geometries. The present thesis, however, studies three-dimensional, axisymmetric BFS geometry which provides a more realistic representation of the base region of a real Ariane 5 launcher. As shown in Figure 2.2(b), the three-dimensional axisymmetric BFS features an axis of symmetry around the BFS geometry with finite cylindrical afterbody extension.

2.2 Base Flow Topology

The flow field in the wake of the BFS geometry is complex and unsteady, involving numerous instability mechanisms. The mean flow topology of a generic BSF geometry, as shown in Figure 1.2, illustrate the most common flow features that develop the wake of the BFS. As can be seen from this figure, the wake of a (subsonic) BFS can be identified by three main zones, namely, the separated shear layer, a recirculation zone and a reattachment zone. The interaction between these flow features result in an unsteady low-frequency motion (Driver et al. (1987), Hudy and Naguib (2007), Spazzini et al. (2001)). The following sections will briefly discuss these flow features that develop in the wake of BFS at subsonic and supersonic flows.

2.2.1 Separated Shear Layer

Shear layer is a layer of fluid where a velocity gradient is present. As shown in Figure 1.2, the separated shear layer originates at the edge of BFS and curls down to impinge on the afterbody. As the upstream boundary layer separates at the edge of BFS, a strong velocity gradient, which is enclosed by the recirculation zone and external flow, induces a shearing force in the flow. This strong velocity gradient in the shear layer is subject to Kelvin-Helmholtz instabilities, which generates eddies that roll-up into spanwise orientation (Robinson (1991), Scharnowski et al. (2016b)). According to Browand (1966), Winant and Browand (1974) and Scharnowski et al. (2016b), as a result of viscous shearing these spanwise oriented eddies grow in size and pair while convecting downstream. In addition, for a BFS geometry it has been shown by Troutt et al. (1984) that eddies grow to a maximum size, proportionate to the step height while moving downstream and result in broadening of the shear layer.

Figure 2.3 show a model that was developed by Winant and Browand (1974) to explain the roll-up process of the eddied in the shear layer of BFS. As shown in Figure 2.3(a), the process of roll-up starts with application of a wave which causes a distortion of the boundary of a region that contains the vortices. This region with vortices generates vertical velocities which causes the disturbances to grow. As a result the region that contains edddies becomes flatter and thinner (with strong waves), as shown in Figure 2.3(b) and Figure 2.3(c). Finally, as the disturbances grow even more, the two shearing layers start to roll over each other forming a discrete eddies (see Figure 2.3(d)). According to Driver et al. (1987), the reattachment of the separated shear layer in the wake of the BFS results into a low-frequency flapping motion. As reported by Robinson (1991), the Kelvin-Helmholtz instabilities in the shear layer may increase for three-dimensional (axisymmetric) model.

2.2.2 Reattachment Zone

As shown in Figure 1.2, the separated shear layer that start at the edge of the BFS, flows downstream and eventually reattaches downstream of the step. This reattachment point is

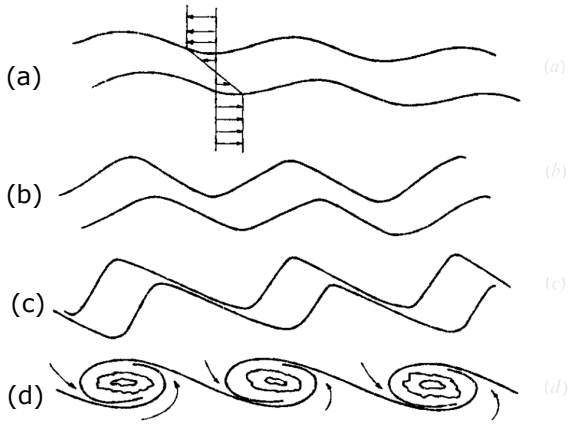

Figure 2.3: Schematic illustration of the initial instability of the shear layer, and the roll-up into discrete eddies (Winant and Browand, 1974)

not fixed at single point, it varies within a region called the reattachment zone. According to Eaton and Johnston (1982), this variation is related to the low-frequency flapping motion. For the present thesis four afterbody configurations with different lengths (L/D) are considered. Depending on the length of these afterbody configurations, the separated shear layer will reattach on the afterbody or on the flow further downstream. A special situation exists if, due to the unsteadiness of the flow, the reattachment intermittently occurs on the afterbody and on the flow. Deprés et al. (2004) refers to these different flow configurations as solid, fluidic and hybrid reattachment. These three different reattachment cases are shown in Figure 2.4.

The reattachment length, x_r is defined as distance between the base and the point where the shear layer impinges the external surface. In the literature, the reattachment length in case of a two-dimensional BFS is commonly made dimensionless using the step height h of the base. For (three-dimensional) axisymmetric BFS, however, the reattachment length is generally non-dimensionalized with the diameter D of the cylindrical main body. Schrijer et al. (2014) conducted an experiment on an axisymmetric BFS at freestream Mach number of 0.7. From statistical analysis of the flow field, a non-dimensionalized reattachment point of approximately $x/D = 1.0$ is observed for the time-averaged shear layer with $h/D = 1/3$. Figure 2.5 shows the comparison of the normalized reattachment length (x_r/h) as function of step height Reynolds number (Re_h) for axisymmetric and (two dimensional) planar cases. From this figure it can be observed that the reattachment length for axisymmetric BFS is shorter than for the two-dimensional case. Furthermore, for the planar case an increase in step height Reynolds number (Re_h) results in increase of normalized reattachment length (x_r/h), while for axisymmetric case an increase in step height Reynolds number result in decrease of the normalized reattachment length (Gentile et al., 2016), although for this configuration this is governed by the effect of an increasing h/D ratio.

According to Adams and Johnston (1988) and Eaton and Johnston (1982), the state of incoming boundary layer and Reynolds number has an effect on the mean reattachment length. Laminar boundary layer and low Reynolds number display increased unsteadiness in reattachement length (x_r) compared to turbulent bondary layer and higher Reyonolds num-

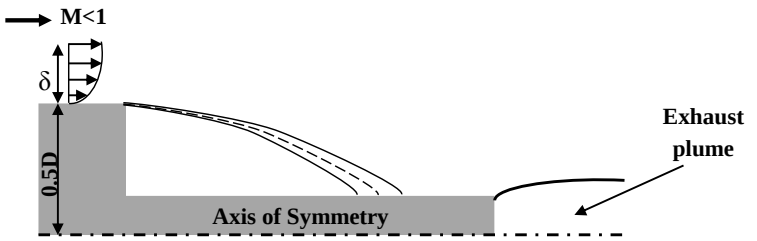

a) Solid reattachment

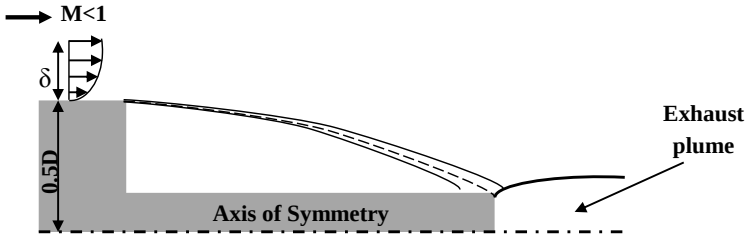

b) Hybrid reattachment

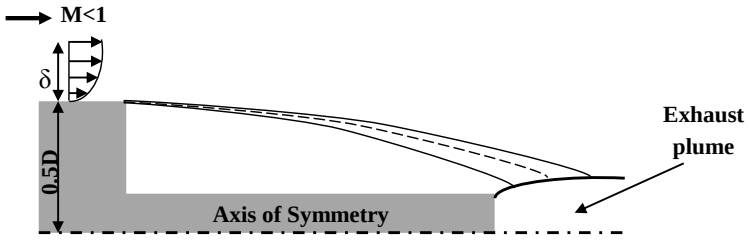

c) Fluidic reattachment

Figure 2.4: Schematic illustration of different reattachment cases

ber. Furthermore, a PIV experiment performed by Scharnowski et al. (2016a) on the two-dimensional BFS have shown that the reattachment length increases from $5.1h$ at freestream Mach number of 0.7 to $5.5h$ at freestream Mach number of 0.8.

2.2.3 Recirculation Zone

A schematic representation of the recirculation zone in the wake of a BFS is shown in Figure 1.2. This zone is bounded by the separating/reattaching shear layer and the external wall of the BFS. Past experimental studies on flow separation over BFS and bluff bodies performed by e.g Kim et al. (1979), Bradshaw and Wong (1972) and Abbott and Kline (1962) gives an insight into the physical aspects of recirculation region. According to Kaul and Frost (1976), the momentum diffusion from shear layer into the recircuation zone sets the wake fluid into motion. In reattachment zone the pressure increases due to the compression. As a result, this pressure increase generates a steep pressure gradient near the wall which returns part of

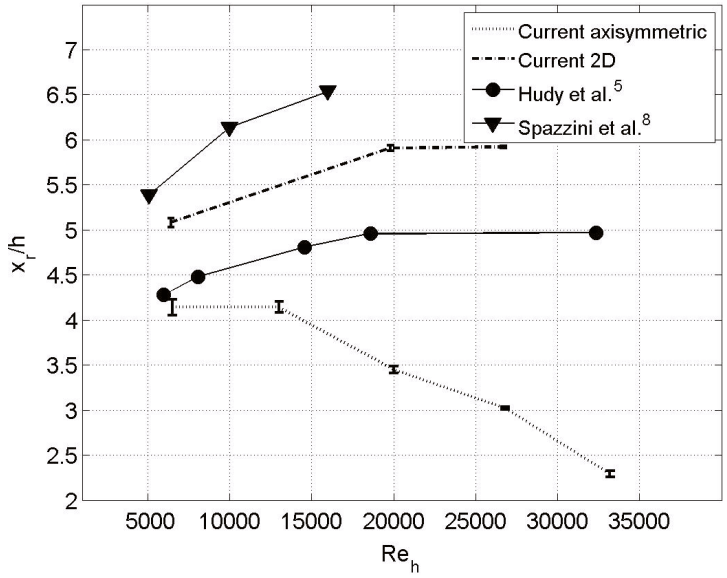

Figure 2.5: Normalized reattachment length (x_r/h) as a function of step height Reynolds number (Re_h) (Gentile et al., 2016)

of the flow near the wall upstream, in order to feed the recirculation zone (Kaul and Frost, 1976).

As shown in Figure 1.2, the recirculation zone consist of two counter-rotating vortices, a primary one at the center which rotates clockwise and a counter clockwise secondary vortex at the left corner of the base. The secondary vortex is a feature that typically occurs in low-subsonic flows. It has been observed in subsonic (e.g Deck and Thorigny (2007), Hall et al. (2003), Spazzini et al. (2001), Hudy and Naguib (2007), Scarano and Riethmuller (1999)) but also in supersonic flows (e.g Bitter et al. (2011)). Figure 2.6 show a time-averaged velocity field with streamlines as presented by Scarano and Riethmuller (1999), which clearly show the occurrence of the primary clockwise vortex that extends from the base of the BFS to the reattachment point and a secondary vortex which is located at the left corner of the BFS. This secondary vortex, commonly referred to as corner eddy, is formed as results of shear layer separation which is induced by the reverse flow now approaching the step as a forward facing step (Kaul and Frost, 1976). According to Hudy and Naguib (2007), the size of this corner eddy decreases as the Reynolds number increases.

The fluctuation of the flow reattachment point causes the recircuation zone to grow and shrink in a quasi-cyclic manner. According to Schrijer et al. (2014) this growing and shrinking is characterized by large-scale fluctuations that dominate the flow motions and the momentum exchange across the shear layer, as illustrated in Figure 2.7. Furthermore, according to Spazzini et al. (2001) the secondary vortex in the corners of BFS also grows in size and strength until it becomes as large as the step height and then break down.

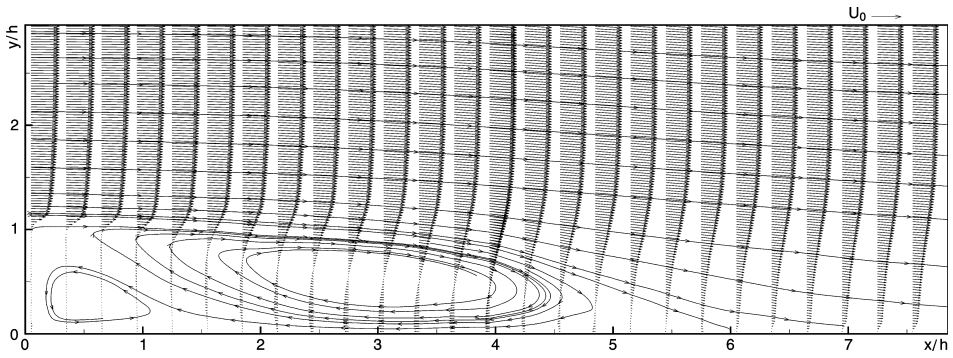

Figure 2.6: A time-average velocity field vector plot and stream-traces pattern in the wake of 2D BFS (Scarano and Riethmuller, 1999)

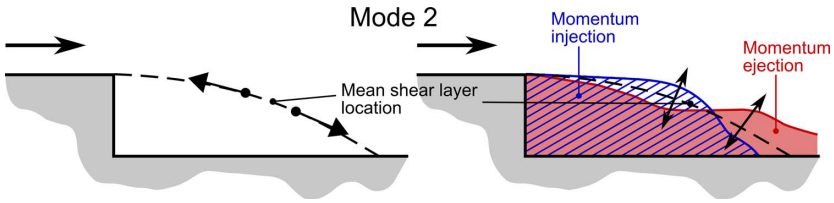

Figure 2.7: Contribution of mode 2 to the flow field (left) and its effect on the shear layer position (right) as indentified by Schrijer et al. (2014)

2.2.4 Supersonic BFS

Figure 1.3 show mean flow topology of a supersonic BFS. At the transition from subsonic ($M < 1$) to supersonic ($M > 1$) flow regimes a PME fan appears at the edge of the BFS. This expansion fan causes a strong deflection of the developing shear layer toward the afterbody wall compared to the subsonic case. As shown in Figure 1.3, as the shear layer impinges on the afterbody wall, the flow turns back in the direction of the freestream and as a result a recompression shock is developed (Loth et al., 1992). According to Simon et al. (2007), the adverse pressure gradient which emerges from the change in in lateral streamline curvature causes the development of the recompression shock. Furthermore, the incoming external flow, which is deflected by an expansion fan at the edge of a generic rocket model, again changes direction due to the expanding supersonic jet and an oblique shock, also called the plume shock develop in the supersonic external stream (e.g. Bannink and Schoones (1998)).

Supersonic BFS have been studied in numerous experimental and numerical investigations. In an experimental study conducted by Meliga and Reijasse (2007), a decrease in reattachment length have been observed when the freestream Mach number increased from 0.9 to 1.3, which can be related to the strong deflection of the shear layer due the centered expansion waves. Similar observation have also been noticed by e.g Chen et al. (2012) and Scharnowski et al. (2016a). According to Simon et al. (2007), the major differences between subsonic and supersonic BFS flows appears to be the decrease of the shear layer growth and the turbulent Reynolds stress magnitude. Furthermore, It has been found that this decrease in shear layer growth and turbulent Reynolds stress magnitude is a result of the compressibility, with the

convective Mach number M_c as a scaling parameter (Simon et al., 2007). Using isentropic flow assumption, the convective Mach number is defined as follow:

$$M_c = \frac{U_1 - U_2}{a_1 + a_2} \tag{2.1}$$

where U_1 and U_2 are the velocities of the high- and the low-speed streams and a_1 and a_2 the corresponding speed of sound.

2.3 Effect of Nozzle Length and Exhaust Plume

As outlined in section 1.1, the goal of the present thesis is to investigate the effect of varying nozzle length and presence of an exhaust plume on the on the flow topology and mean pressure distribution on the wake of axisymmetric BFS at subsonic and supersonic flows. As such, this section aims to provide a brief review of the past studies that have been performed by other researchers to investigate these effects.

2.3.1 Varying Nozzle Length

The effect of nozzle length and presence of exhaust plume on the mean and unsteady surface pressure field in the wake of an axisymmetric BFS have been investigated experimetally by Deprés et al. (2004) using pressure tap. Four model configuration were tested, with and without supersonic exhaust plume at freestream Mach number of 0.85. Two of these model configurations were with extended cylindrical rear-body (nozzle), having a length of $L/D = 0.6$ and 1.2. From these experiments, it is observed that the nozzle length (L/D) play an important role in the mean and unsteady flow features in the wake of a transonic axisymmetric BFS compared to the configuration with presence of exhaust plume. The effect of exhaust plume will be discussed in section 2.3.2. Similar observation have been also noted by Scharnowski et al. (2016a), where a two-dimensional BFS model with an exhaust plume was investigated in subsonic, transonic and supersonic external flows using PIV technique.

Depending on the length of the nozzle, L/D the separated shear layer will impinge on the nozzle wall (solid reattachment), the flow (fluidic reattachment) or on the nozzle wall and flow (hybrid reattachment) (Deprés et al., 2004) (Figure 2.4). For $L/D = 1.2$, it is observed that the presence of exhaust plume has little effect on both the mean and unsteady pressure because it is located farther downstream and it is not interacting immediately with the subsonic recirculation zone. When $L/D = 0.6$, the presence of exhaust plume causes the static pressure for a given nozzle pressure ratio (NPR) to decrease by approximately a constant value compared to the case without exhaust plume. This reduction in pressure, which is due to the jet suction effect, alters the attached boundary layer up to $x/D = -0.4$. Furthermore, for $L/D = 0.6$, the exhaust plume directly interacts with the recirculation bubble, resulting in higher rms pressure levels on the nozzle. Despite the fact that the exhaust plume forms an obstacle in the wake, the production of large-scale vortices still persists. For $L/D = 1.2$, the separated shear layer impinges near the end of the nozzle, with the predominant vortex shedding frequency of $Sr_L \approx 0.6$, which is related to the transportation of the eddies in the

separated shear layer. For $L/D = 0.6$, the separated shear layer impinges on the exhaust plume, with the dominated large scale vorticies at a shedding frequency of $Sr_D \approx 0.2$. A numerical investigation on a similar model configuration as used by Deprés et al. (2004), have been carried out by Weiss et al. (2009). A vortex shedding frequency of $Sr_D \approx 0.2$ have been found which is in agreement with the frequencies that was also found by Deprés et al. (2004) (for $L/D = 0.6$) and Meliga and Reijasse (2007).

Deprés et al. (2004) also observed a reduction of the predominance of the antisymmetric mode $m = 1$ for increasing nozzle length. An another experiment was conducted by Wolf et al. (2012), who investigated the effect of the perturbing afterbody, with L/D of 1.2 on the bluff body geometry in subsonic freestream conditions. The result of this investigation showed that the mean wake flow topology stay unaffected when the nozzle is present. However, it has a stabilizing effect on the flow field which is due to a decrease of the static turbulent level and the elimination of the large-scale dynamic modes.

2.3.2 Presence of Exhaust Plume

Wind tunnel experiments were conducted by Bergman (1970) to investigate the effect of exhaust plume on the boat-tail pressure drag. From this experiment it is concluded that the exhaust plume has two substantial effect on the local flow field and pressure drag, namely, it leads to the displacement of the outer flow as a results of blockage and it causes the acceleration of the outer flow due to entrainment at the plume boundary. Furthermore, it is shown that the blockage causes the pressure in the base regions to increase while the entrainment at the plume boundary results in decrease (Bergman, 1970).

As noted in section 2.3.1, the presence of exhaust plume has little effect on the mean and unsteady presures compared to the variation of the nozzle length. This effect can be small if the separated shear layer reattaches on the nozzle (solid reattachment), well upstream of the exhaust plume. The effect is significant if the nozzle is short enough to allow fluidic reattachment (Deprés et al., 2004). An experimental investigation on base flow and exhaust plume interaction in supersonic flow regimes have been carried out by Bitter et al. (2012). By employing pressure sensitive paint (PSP), it is found that the pressure distribution in the wake region of the FESTIP model is not affected for changing nozzle pressure ratio (NPR). Also, Scharnowski et al. (2016a) concluded that the presence of an exhaust plume is not affecting the reattachment point of the separated shear layer. The findings by Bitter et al. (2012) and Scharnowski et al. (2016a) are in accordance with the results found by Deprés et al. (2004). Furthermore, according to Wolf et al. (2012), the presence of exhaust plume in the near wake of the BFS has a stabilizing effect and also leads to the elongation of the recirculation zone, which is due to the acceleration of the shear layer caused by the exhaust plume.

Chapter 3

Measurement and Pressure Reconstruction Techniques

This chapter aims to provide the reader with the basic principles of the flow diagnostics that will be used in the present thesis: Particle Image Velocimetry (PIV) and Schlieren visualization. For the present thesis the quantitative investigation of the axisymmetric base flows will be done using two component PIV (2C-PIV), therefore the discussion of the basic principle will be limited to planar PIV only. Also, this chapter aims at setting out the numerical technique which is necessary to reconstruct the mean pressure from the obtained PIV data.

3.1 Particle Image Velocimetry

PIV is a whole-flow-field imaging based measurement technique which provides instantaneous velocity vector measurements in a cross-section of a flow. Nowadays it is one of the most successful measurement technique used in education and industrial research. In modern aerodynamic studies this technique is very attractive for the reason that it helps to investigate unsteady flow phenomena as, for example, in separated flows that occurs at the trailing edge of a typical BFS geometry (Raffel et al., 2007). In the following sections, the basic working principle of PIV will be described briefly.

3.1.1 General Working Principles

PIV is a non-intrusive measurement technique where light scattering micron-sized tracer particles are employed to track the fluid flows. These micron-sized tracer particles are said to be *ideal* when they (1) accurately follow the motion of the fluid, (2) do not alter the fluid

motion or its properties, (3) do not interact with each other and (4) scatter enough light (Westerweel, 1997). Figure (4.14) illustrates a typical experimental setup of a planar (2C) PIV measurement in a wind tunnel and its working principle. This setup consist of a laser, imaging and laser sheet optics and high resolution digital camera. Light scattering tracer particles are inserted to the flow, upstream of the measurement plane. Using laser optics and mirror, the light beam coming from the laser is formed into a light sheet illuminating tracer particles twice with a short time interval Δt (LaVision GmbH, 2012). This time interval is dependent on the mean flow velocity and the magnification at imaging (Raffel et al., 2007). The light that is scattered by the tracer particles are captured onto two consecutive frames by a charged-couple device (CCD). By knowing the displacement of the two captured particle

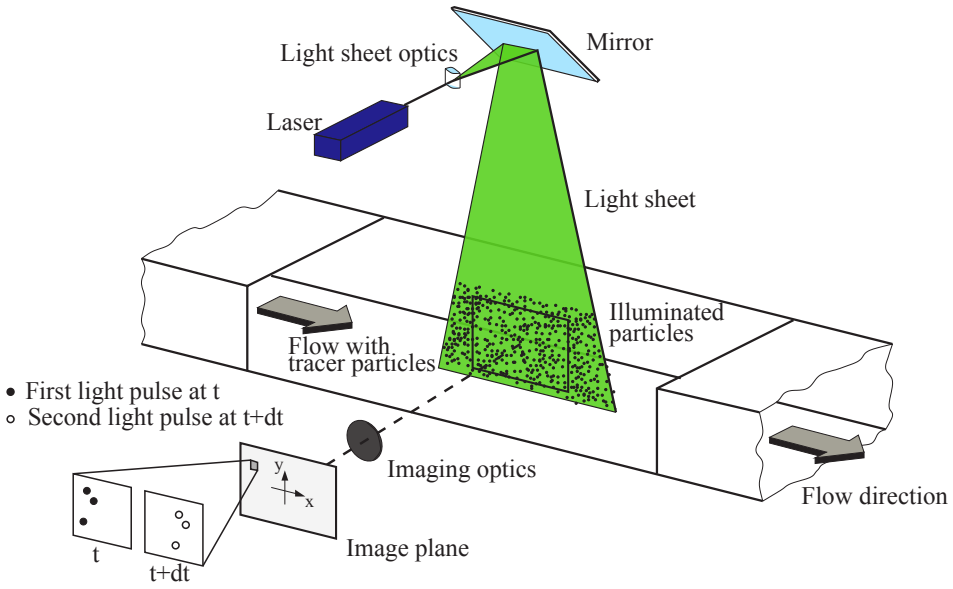

Figure 3.1: Schematic representation of a two-dimensional PIV-setup in the wind tunnel. Adapted from Raffel et al. (2007)

images and the time interval, one can calculate the particle velocity with a central finite difference (de Kat, 2012),

$$u\left(t\right) = \frac{x\left(t+\Delta t\right) - x\left(t\right)}{\Delta t} + o\left(\Delta t^2\right) \tag{3.1}$$

where u is the tracer particle velocity, x is the position of the tracer particle and Δt is time separation between the two pulses. Rather applying this approach to estimate the particle velocity, PIV software performs statistical analysis and cross-correlation to obtain displacement of a group of particles images within an interrogation window (de Kat, 2012). Figure (3.2) shows how the particle velocity is obtained by cross-correlation of two particles images. This is done by subdividing the particle image into small interrogation windows. Afterwards, by performing cross-correlation and localization of the correlation peak, the average particle image separation (Δx, Δy) is obtained. With the given magnification (M) of the camera, the two velocity components, u and v can obtained as follow (LaVision GmbH, 2012)

$$u = \left(\frac{1}{M}\right)\left(\frac{\Delta x}{\Delta t}\right) \tag{3.2}$$

$$v = \left(\frac{1}{M}\right)\left(\frac{\Delta y}{\Delta t}\right) \tag{3.3}$$

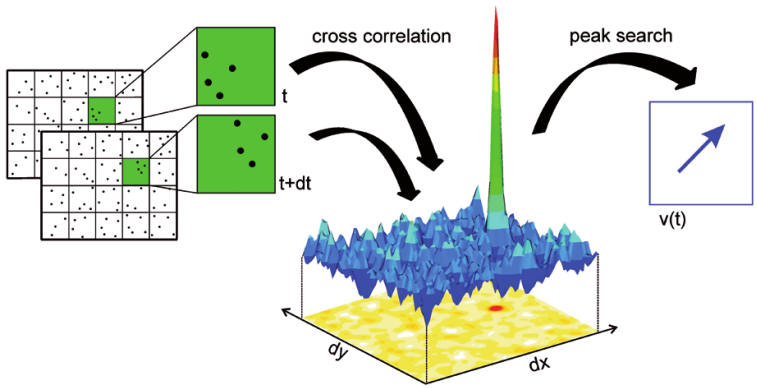

Figure 3.2: Evaluation of two images by cross-correlation. Adapted from LaVision GmbH (2012)

3.1.2 Tracer Particles

PIV is an indirect measurement technique which computes the tracer particle velocity rather than fluid velocity. For this reason the fluid mechanical properties of the tracer particles have to be carefully investigated in order to be certain that they faithfully follow the flow.

The accuracy of PIV measurements is primarily affected by the choice of flow tracer particles. For an accurate PIV measurements, it is required that the tracer particles are small enough to follow the flow but large enough to scatter enough light. These two requirement oppose one another, requiring a trade-off solution to acquire an optimum. Raffel et al. (2007) provides an estimate for the velocity lag of a particle in a continuously accelerating fluid to be:

$$\mathbf{U}_s = \mathbf{U}_p - \mathbf{U} = d_p^2\left(\frac{(\rho_p - \rho)}{18\mu}\right)\mathbf{a} \tag{3.4}$$

where $\mathbf{U_p}$ is the tracer particle velocity, $\mathbf{U}$ is the flow velocity, μ is the dynamic viscosity of the fluid, ρ_p and ρ are the density of the particle and fluid, d_p is the diameter of the particle and finally $\mathbf{a}$ the acceleration of the flow. When the density of the particle is lager than the fluid density, the step response of a particle velocity is given by

$$\mathbf{U}_p\,(t) = \mathbf{U}\left[1 - \exp\left(-\frac{t}{\tau_p}\right)\right] \tag{3.5}$$

where τ_p is particle time response given by:

$$\tau_p = d_p^2\frac{\rho_p}{18\mu} \tag{3.6}$$

This response time is the time after which the particle velocity changes to 1-e^{-1} = 63% of the new flow velocity (Scarano, 2013). The value of this should be kept below the smallest time scale of the flow, yielding a critical conditions for the cases where turbulent flows are considered.

For the present experiment titanium dioxide ($TiO2$) particles of type Kemira P580 will be used, which are known to accurately follow the flow. These particles have a primary crystal size of 30 nm, a nominal density of 150 kgm^{-3} and a particle response time of τ_p = 2.56 μs (Ragni et al., 2011). However, since the current experiment will be performed in high-speed flow regimes where shock waves are present, the faithful flow tracing can never be accomplished, at least inside limited regions of the flow directly downstream of a shock wave where the flow unexpectedly slows down. The particle tracing fidelity in turbulent flows is evaluated by Stokes number S_k, defined as follow:

$$S_k = \frac{\tau_p \cdot U_\infty}{D} \tag{3.7}$$

Tropea et al. (2007) states that the condition S_k <1 returns an acceptable flow tracing accuracy with errors below 1%. The free stream velocities for the current experiment will be approximately 239 ms^{-1} for high subsonic cases and 534 ms^{-1} for supersonic cases. These freestream stream velocities, particle response time of τ_p = 2.56 μs and main body diameter of D = 50 mm, result in Stokes number of S_k = 0.01 for subsonic cases and S_k = 0.03 for supersonic cases, respectively.

As mentioned before, small tracer particles are necessary to achieve the fluid mechanical requirements and flow fidelity. However, small particles scatter less light and are more difficult to detect. The scattering efficiency of a tracer particle is computed by the scattering cross section which depends on the ratio of refractive index, the wavelength of light λ^{-4} and the particle diameter d_p (Scarano, 2013). A common way to solve the issue with less scattering light behavior of smaller particle is to use larger particles, provided they still follow the flow accurately (Scarano, 2013).

3.1.3 Imaging of Particles

Imaging of the tracer particles in the light sheet require imaging system. This system consist of cameras and photographic lenses and it is characterized by its focal length f, f-number ($f_\#$) and image magnification M. The photographic lenses are used to focus the image of particles on an imaging plane. The distances from the object plane Z_0 to the photographic lens and from the photographic lens to the image plane z_0 are related by thin lens formula (See Figure (3.3)) (Raffel et al., 2007):

$$\frac{1}{f} = \frac{1}{z_0} + \frac{1}{Z_0} \tag{3.8}$$

By knowing the distances Z_0 and z_0, one can determine the magnification, M with the following equation:

$$M = \frac{z_0}{Z_0} \Rightarrow M = \frac{\text{pixelsize} \times \#\text{ofpixels}}{FOV} \tag{3.9}$$

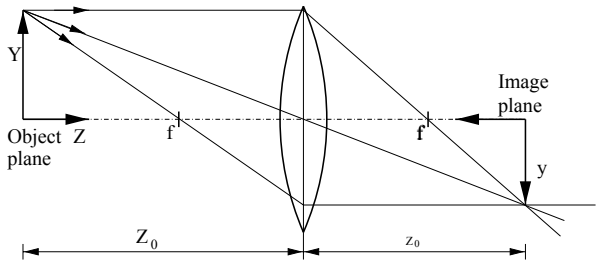

Figure 3.3: Schematic representation of the object plane, lens and image plane. Adapted from Raffel et al. (2007)

Furthermore, by knowing the focal length (f) and the aperture diameter (D) of the lens, one can define the f-number ($f_\#$) to be

$$f_\# = \frac{f}{D} \tag{3.10}$$

By knowing the the magnification, M and the effective particle diameter d_p, the diameter of particle images can be obtained by

$$d_{geom} = M \cdot d_p \tag{3.11}$$

But, due to diffraction effects the minimum particle image diameter is limited to

$$d_{diff} = 2.44 \cdot f_\# \cdot \lambda\,(M+1) \tag{3.12}$$

where λ is the wave length of the laser light. With Euclidean sum of d_{geom} and d_{diff}, an approximation of the resulting particle image diameter is given by

$$d_\tau = \sqrt{(M \cdot d_p)^2 + (d_{diff})^2} \tag{3.13}$$

For considerably small particles, the expression of d_τ is generally dominated by the diffraction limit, meaning that $d_\tau \approx d_{diff}$. This is an important parameter that should be carefully considered when perfoming PIV experiments. Scarano (2013) reports an optimum situation that is accomplished when d_τ is approximately 2-3 pixels. When $d_\tau < 1$, the particle position and the measurement displacement tend to be locked to integer values, also commonly referred to as as peak locking. According to Scarano (2013), the focal depth δ_z, which gives the range in which the particles are in focus, can be determined with Equation (3.14) (Scarano, 2013)

$$\delta_z = 4.88 \cdot \lambda \cdot f_\#^2 \left(\frac{M+1}{M}\right)^2 \tag{3.14}$$

In this equation the $f_\#$ is the only parameter that can be adjusted. This parameter can be used to optimize the particle image size, which is vital for the accuracy of the PIV measurement. The light intensity captured on the sensor of the camera and velocity measurement errors depends on this parameter. Selecting low values for $f_\#$ will result in an increase of light intensity. This however, decreases the depth of focus and therefore making it difficult to focus.

3.1.4 Illumination and Image Recording

Lasers Nowadays pulsed lasers are the standard choice as a light source for PIV applications. These light sources have the capacity to provide monochromatic light with high energy density. The provided monochromatic light can be easily shaped into a thin light sheet without being affected by chromatic aberrations (Raffel et al., 2007). The Neodym-YAG (Nd:YAG) and Neodym-YLF (Nd:YLF) are the most common lasers used for PIV applications. Table (3.1.4) provides the specification of these two types of lasers. The choice of laser depends on the type of PIV experiment to be conducted. For high-speed (time-resolved) PIV experiments, which requires significantly higher recording rates, the Nd:YLF laser is preferred. This laser has a much higher repetition rate but a lower pulse energy compared to Nd:YAG laser. The Nd:YAG laser is commonly used for low-speed PIV experiments where the recording rate is not requirement.

Type	Wavelength $[nm]$	Pulse Energy $[mJ]$	Repetition Rate $[Hz]$
Nd:YAG	532	20 - 500	10 - 30
Nd:YLF	526	10 - 30	1,000 - 10,000

Table 3.1: Specification of lasers for PIV application. Adapted from Scarano (2013)

Camera The most common used camera for PIV measurements are Charge Coupled Device (CCD) and Complementary Metal Oxide Semiconductor (CMOS). A perfomance comparison of these two cameras can be found in Hain et al. (2007). According to Raffel et al. (2007), CCD cameras are extensively used in PIV experiments compared to CMOS. However due to repaid development of chip technology the CMOS cameras are more frequently used for high-speed PIV.

3.2 Schlieren Visualization

Schlieren is an experimental technique that is used to visualize the flow field of varying density by using refraction of the light. The schlieren system shown in Figure (3.4) is by far the most popular arrangement, also known as *z-type* Herschellian system. It consist of consists of a focused light source, two field mirrors, a display screen/board and a knife edge. This technique relies on the principle of light refraction due to the variation of the refractive, which can be described by Snells law as:

$$n_1 \cdot \sin(\alpha_1) = n_2 \cdot \sin(\alpha_2) \tag{3.15}$$

Where 1 and 2 refer to different physical media, n_i is the refraction index and α_i is the incidence angle of the light beams. Equation (3.15) describes the change of the direction of light beam when entering a material with a different refraction index as illustrated in Figure 3.5. The value of the refractive index of a transparent medium is given by:

$$n = \frac{c_0}{c} \tag{3.16}$$

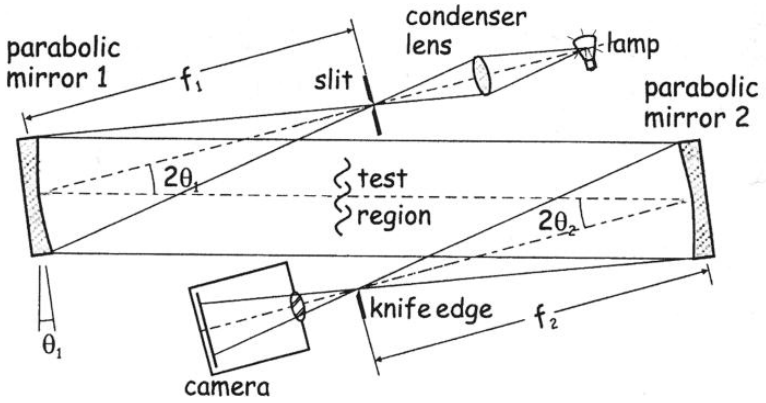

Figure 3.4: Z-type schlieren arrangement (Settles, 2001)

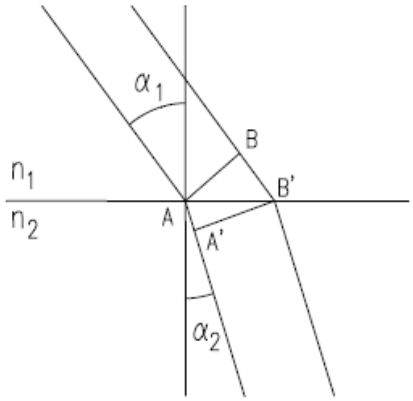

Figure 3.5: Refraction effect of light beam

where c_0 is the speed of light in vacuum (3×10^8 m/s) and c is the local speed of light. The refractive index for air and other gases is given by (Settles, 2001):

$$n = 1 + k\rho \tag{3.17}$$

where k is Gladstone-Dale constant (2×10^{-4} m3/kg for air) and ρ is the local density. From this equation it can stated that variations of density directly translate into variations of the refractive index. This basically what Schlieren visualization technique does.

According to Settles (2001) the optical inhomogeneities tends to refract light rays in proportion to their gradients of refractive index in an x-y plane. The curvature of a refracted light ray is given in Equation (3.18).

$$\frac{\partial^2 x}{\partial z^2} = \frac{1}{n}\frac{\partial n}{\partial x} \qquad \frac{\partial^2 y}{\partial z^2} = \frac{1}{n}\frac{\partial n}{\partial y} \tag{3.18}$$

Integration of Equation (3.18) once, gives the components of the angular light ray deflection in the x-y directions:

$$\varepsilon_x = \frac{1}{n}\int \frac{\partial n}{\partial x}\partial z \qquad \varepsilon_y = \frac{1}{n}\int \frac{\partial n}{\partial y}\partial z \tag{3.19}$$

With the refractive index n given in Equation (3.17), the expressions in Equation (3.18) and Equation (3.19) can be written as:

$$\varepsilon_x = \frac{k}{1+k\rho}\int \frac{\partial \rho}{\partial x}\partial z \qquad \varepsilon_y = \frac{k}{1+k\rho}\int \frac{\partial \rho}{\partial y}\partial z \tag{3.20}$$

The light intensity gradients of the images acquired with Schlieren are related to the density gradients in the flow according to:

$$\frac{\Delta I}{I} \propto \frac{K f_2}{a}\int_{x_1}^{x_2} \frac{\partial \rho}{\partial x} dz \tag{3.21}$$

where f_2 is the focal length of the parabolic mirrors and a is the light offset. Now that the working principle of the Schlieren visualization id known, the Schlieren setup can be made. This setup will be discussed in section 4.4

3.3 Pressure Reconstruction

For the current investigation, the main flow variable of interest is the pressure in the base region of an axisymmetric BFS. There are numerous way to obtain pressure field experimentally, such as using pressure orifices or pressure sensitive paint. However, the applicability of these techniques are limited for the study of the dynamics fluid phenomena due to their intrusive nature and the limitation to provide a characterization of the mean flow field only (van Oudheusden, 2013). To overcome these limitations, the present thesis will implement the state-of-the-art method in which the pressure field is determined from the velocity data obtained from the PIV experiments. The principle of this method relies on combining the velocity field data obtained from PIV experiment with the governing flow equations. This method will be discussed in this chapter.

Pressure field determination based on the instantaneous velocity field data obtained from PIV have been studied by Gurka et al. (1999). In this study two incompressible low-speed flow problems haven been tested; a water flow in a pipe and an impinging air jet. The pressure field is computed using pressure Poisson equation which was derived by applying the divergence operator on the incompressible Navier-Stokes equation (Gurka et al., 1999). The current thesis, however, deals with high-speed compressible flows. An extension of the pressure field computation for high-speed compressible flows are outlined in van Oudheusden et al. (2007), Van Oudheusden (2008a), van Oudheusden (2013) and Souverein et al. (2007).

PIV based pressure field determination shows some similarity with Computational Fluid Dynamics (CFD) based computation. Both methods use Reynolds-averaged Navier Stokes equation to determine time-averaged flow variables. The main difference, however, is that for a CFD based computation the velocity field data is determined numerically rather than being obtained experimentally as it is in the case of PIV based computation. Also CFD approach for compressible flows requires momentum, continuity and energy equations to form a closed system whereas PIV based approach only requires the momentum equation.

3.3.1 Governing Equations

For incompressible flows the Navier-Stokes equations can be employed to determine the pressure gradient from the momentum equation, with the assumption that density and viscosity are known (van Oudheusden, 2013):

$$\nabla p = -\rho \frac{D\vec{U}}{Dt} + \mu \nabla^2 \vec{U} \tag{3.22}$$

In Equation (3.22) $\frac{D\vec{U}}{Dt}$ is the acceleration of a fluid particle followed from Lagrangian perspective. From an Eulerian perspective (stationary reference frame), the material derivative can be expressed as:

$$\frac{D\vec{U}}{Dt} = \frac{\partial \vec{U}}{\partial t} + \left(\vec{U} \cdot \nabla\right) \vec{U} \tag{3.23}$$

Inserting Equation (3.23) into Equation (3.22), the following expression is obtained for the momentum equation:

$$\frac{\nabla p}{p} = -\rho \left(\frac{\partial \vec{U}}{\partial t} + \left(\vec{U} \cdot \nabla\right) \vec{U} \right) + \mu \nabla^2 \vec{U} \tag{3.24}$$

Since the current investigation deal with high-subsonic (transonic) and supersonic flow regimes, the momentum equation, as shown in Equation (3.24), has to be adapted in order to account for the compressibility effects. For compressible flows the density and viscosity show up as an extra unknowns in the momentum equation. Therefore to solve for pressure, additional relations (flow equations) have to be invoked. These additional equations are invoked by using ideal gas law and the adiabatic flow assumption (van Oudheusden et al. (2007), Van Oudheusden (2008a), van Oudheusden (2013) and Souverein et al. (2007)). The ideal gas law, as defined in Equation (3.25), is employed to replace density with pressure and temperature:

$$\rho = \frac{p}{RT} \tag{3.25}$$

The adiabatic flow assumption on the other hand is employed to express the temperature in terms of velocity:

$$\frac{T}{T_\infty} = 1 + \frac{\gamma - 1}{2} M_\infty^2 \left(1 - \frac{\vec{U}^2}{U_\infty^2} \right) \tag{3.26}$$

where γ is the specific hear ratio ($\gamma = 1.4$ for air), M_∞ is the freestream Mach number which is derived from the known flow conditions and $\vec{U} \Big/ U_\infty$ is the velocity ratio which is obtained from PIV data. Using isentropic flow assumption, the pressure ratio (p/p_∞) can be obtained from temperature ratio derived in Equation (3.26) as follow:

$$\frac{p}{p_\infty} = \left(\frac{T}{T_\infty} \right)^{\frac{\gamma}{\gamma - 1}} \tag{3.27}$$

It should be noted that Equation (3.27) is only valid for the regions of isentropic flow and not in the wake of an axisymmetric BFS, which is the region of interest for the current investigation. As will be discussed in section 3.3.3, the pressure ratio as seen in Equation (3.27) will be used as boundary condition for solving the mean pressure field.

Using ideal gas law and adiabatic flow assumption, Equation (3.24) can be written as:

$$\frac{\nabla p}{p} = -\nabla \ln\left(\frac{p}{p_\infty}\right) = -\frac{\gamma M_\infty^2}{U_\infty^2 + M_\infty^2\left(\frac{\gamma-1}{2}\right)\left(U_\infty^2 - \vec{U}^2\right)}\left(\frac{\partial \vec{U}}{\partial t} + \left(\vec{U}\cdot\nabla\right)\vec{U}\right) + \mu\nabla^2\vec{U} \tag{3.28}$$

The aim of the present investigation is to determine the mean pressure field for high-subsonic (transonic) and supersonic BFS flows. Mean pressure field is invariant in time. Therefore, the unsteady time derivative term in Equation (3.28) can be canceled. Also for high Reynolds numbers flows, the viscous term in Equation (3.28) can be neglected (van Oudheusden et al., 2007). As a result, the momentum equation can be written as:

$$\frac{\nabla p}{p} = -\nabla \ln\left(\frac{p}{p_\infty}\right) = -\frac{\gamma M_\infty^2}{U_\infty^2 + M_\infty^2\left(\frac{\gamma-1}{2}\right)\left(U_\infty^2 - \vec{U}^2\right)}\left(\left(\vec{U}\cdot\nabla\right)\vec{U}\right) \tag{3.29}$$

From PIV experiment only the velocity data can be obtained. Therefore, to formulate the pressure gradient components only in terms of velocity, for steady flow conditions the non-conservative formulation of the momentum equation as given in Equation (3.30) is followed (Van Oudheusden, 2008a).

$$\frac{1}{p}\frac{\partial p}{\partial x_i} = \frac{\partial \ln\left(\frac{p}{p_\infty}\right)}{\partial x_i} = -\frac{1}{RT}u_j\frac{\partial u_i}{\partial x_j} \tag{3.30}$$

For turbulent flows the contribution of turbulent stresses are included in the pressure gradient formulation by Reynolds-averaged form of the momentum equation (Equation (3.29). The idea behind Reynolds-averaging is to decompose an instantaneous quantity into its mean and fluctuating quantities. As outlined by Van Oudheusden (2008a), the Reynolds-averaged (non-conservative form) momentum equation can be expressed as seen in Equation (3.31). Here the effect of density fluctuation have been neglected, as well as the viscous stresses.

$$\left(\delta_{ij} + \frac{\overline{u_i' u_j'}}{RT}\right)\frac{\partial \ln(\bar{p}/p_\infty)}{\partial x_j} = -\frac{1}{RT}\left(\bar{u}_j\frac{\partial \bar{u}_i}{\partial x_j} + \frac{\partial \overline{u_i' u_j'}}{\partial x_j} - \frac{\overline{u_i' u_j'}}{T}\frac{\partial T}{\partial x_j}\right) \tag{3.31}$$

A theoretical order-of-magnitude analysis performed by van Gent et al. (2017b), showed that the Reynolds-averaging formulation for unsteady flows as seen in Equation (3.31), can be simplified to:

$$\frac{\partial \ln(\bar{p}/p_\infty)}{\partial x_i} = -\frac{1}{RT}\left(\bar{u}_j\frac{\partial \bar{u}_i}{\partial x_j} + \frac{\partial \overline{u_i' u_j'}}{\partial x_j}\right) \tag{3.32}$$

Here p is the pressure, u_i denotes the velocity in the x_i direction, T is the temperature and R is the specific gas constant. Equation (3.32) does not consider the spatial gradient of the mean density and the effect of density fluctuations (Jeon et al., 2015), as a preliminary investigation showed that inclusion of the related terms does not lead to more accurate results.

3.3.2 Sequential Least-Square Pressure Field Reconstruction

To solve Equation (3.32) for pressure, similar discretisation technique as proposed by Jeon et al. (2015) is used. The discretization of sub-domains and the corresponding pressure gradient fields resulted in a linear system of equations, which is then solved using the Matlab algorithm *mldivide*.

According to Jeon et al. (2015), the cost function s is defined as a sum of squares of the difference between the measured and the reconstructed pressure gradients over the certain integration domain D as follows:

$$s = \sum_{\mathrm{x}\in\mathrm{D}} |\nabla p_{\mathrm{PIV}} - \nabla p| \tag{3.33}$$

Here ∇p_{PIV} is the measured pressure gradient from PIV, ∇p is the reconstructed pressure gradient and x is the position of grid point. In contrast to Jeon et al. (2015), the solver does not use a staggered grid for both calculating the pressure at each PIV grid point and considering the pressure gradient between the grid points.

3.3.3 Boundary Conditions

Solving for pressure as outlined in section 3.3.2, requires specification of appropriate boundary conditions on the region of interest. Two types of boundary conditions can be employed, either Dirichlet boundary condition or Neumann boundary conditions. For the current investigation, pressure gradients were used implicitly as Neumann boundary conditions on all sides of the domain except for the top of the domain for -0.1 $< x/D <$ 0.5, as shown in Figure (3.6)(red line). In the top of the domain the logarithm of the pressure ratio (Equation (3.27)) obtained from isentropic flow relations was prescribed as a boundary condition, as indicated in Figure (3.6)(blue line). The validity of assuming isentropic flow at distances larger than two step-heights from the afterbody was demonstrated in van Gent et al. (2017). Neumann boundary condition are employed in the wake of the BFS where the isentropic flow assumption is invalid.

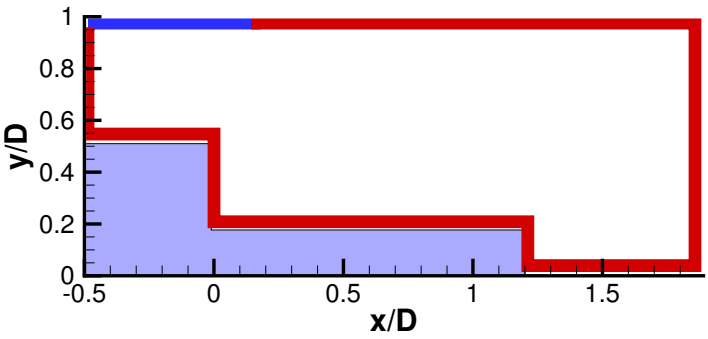

Figure 3.6: Application of boundary conditions for pressure reconstruction. Red lines indicate the Neumann type while the blue line indicate logarithm of the pressure ratio type boundary condition

Chapter 4

Experimental Apparatus and Arrangements

In order to accomplish the research objectives of the present thesis, a planar PIV experiment in combination with Schlieren visualization have been conducted in the transonic-supersonic wind tunnel (TST-27) of the High-Speed Aerodynamics Laboratories at the Delft University of Technology.

This chapter discusses the experimental apparatus that are used for the PIV and Schileren experimental campaigns and their corresponding arrangements. The discussion start with the introduction of the flow facility and the wind tunnel model, followed by a discussion of experimental campaigns and flow conditions. Next, the Schlieren and planar PIV experimental apparatus and setup are discussed, followed by PIV image acquisition and processing. Finally, this chapter ends with PIV uncertainty analysis.

4.1 Flow Facility

A picture of the TST-27 wind tunnel is shown in Figure 4.1. The TST-27 wind tunnel is used to study flows in transonic and supersonic regimes. It is a blowdown type wind tunnel with a test section width of 280 mm and a height varying from 250 mm to 270 mm depending upon the Mach number. The freestream Mach number (M_∞) in the test section range from 0.5 to 0.85 (subsonic) and from 1.15 to 4.2 (supersonic). The supersonic Mach numbers at the test section are achieved by a continuously variable throat and a flexible upper and lower nozzle walls, with a possibility to vary the Mach number during a run (Figure 4.2). For subsonic flows the Mach numbers are set by means of a variable choke section in the outlet diffusor, as shown in Figure 4.2.

Small deviations of the Mach number during a run are corrected by automatic fine adjustment of the choke. For generating dry oil free air in the wind tunnel, a 300 m^3 vessel which is pressurized to 40 bar is used. The maximum running time of the wind tunnel is up to 300

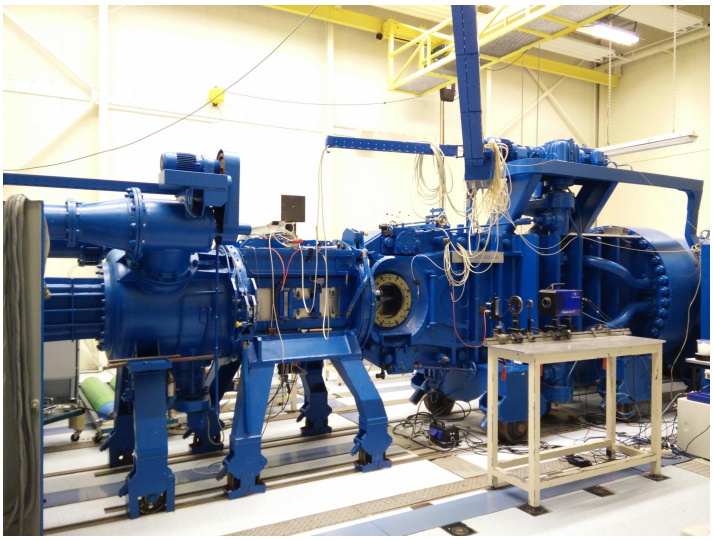

Figure 4.1: The TST-27 wind tunnel

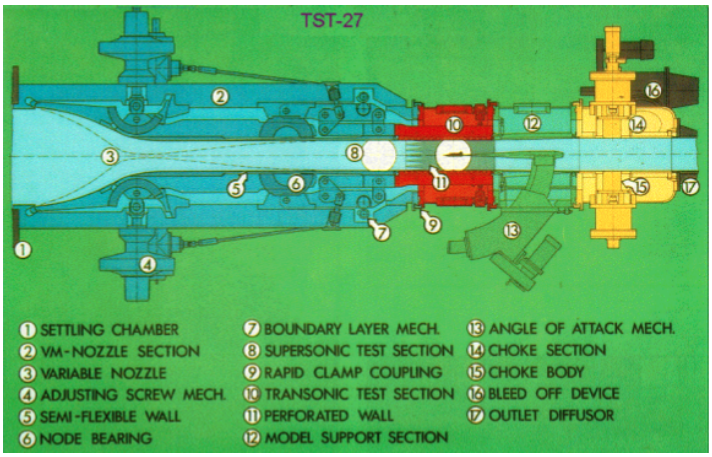

Figure 4.2: Schematic layout of the TST-27 wind tunnel, top view (Bannink and Schoones, 1998)

seconds and allows to investigate the flow field over a model. This wind tunnel is designed such that the maximum unit Reynolds number varies from $3.8 \cdot 10^7$ m^{-1} in the transonic range to $1.30 \cdot 10^8$ m^{-1} at Mach number of 4. As can be seen from Figure 4.1, circular quartz glass windows on either side of the wind tunnel are provided for the optical access to the test section.

4.2 Wind Tunnel Model

The wind tunnel model used for the present investigation is a modified version of the original FESTIP (Future European Space Transportation Investigations Program) model that was used by Bannink et al. (1997) and Scarano et al. (2005) to study experimentally and

numerically the base flow and exhaust plume interaction. As shown in Figure 4.3, the modified model is axisymmetric consisting of a conical forebody with a length of 97 mm and a cylindrical afterbody with a length of 90 mm.

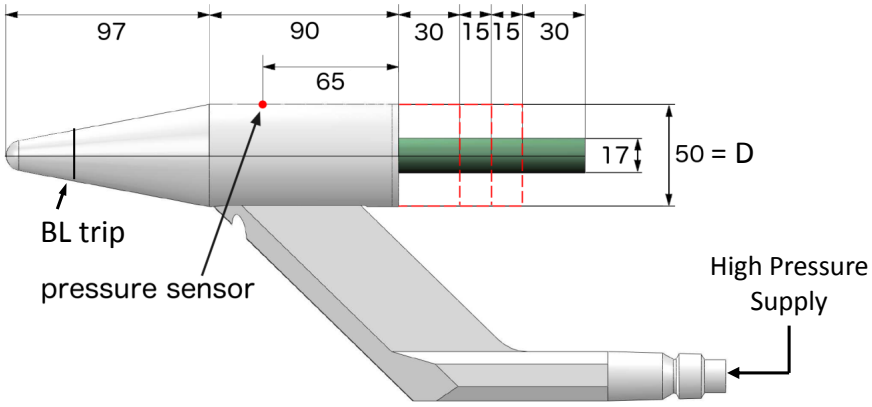

Figure 4.3: Modified FESTIP Model

The conical forebody has a semi-apex angle of 11° and a nose bluntness radius of 7.5 mm. The cylindrical main body has a diameter (D) of 50 mm. The nozzle that generates cold exhaust plume of dry air, protrudes from the center of the cylindrical main body. The nozzle is conical with a divergence of 15° (half angle of 7.5°). As shown in Figure 4.3, the model is supported in the wind tunnel at the lower side of the cylindrical main body. Through tubes in the model support compressed air from four 50 liter bottles is supplied to the nozzle for the generation of a cold exhaust plume. Each of these compressed air bottles are filled up to a pressure of 300 bar using a compressor (Figure 4.4)

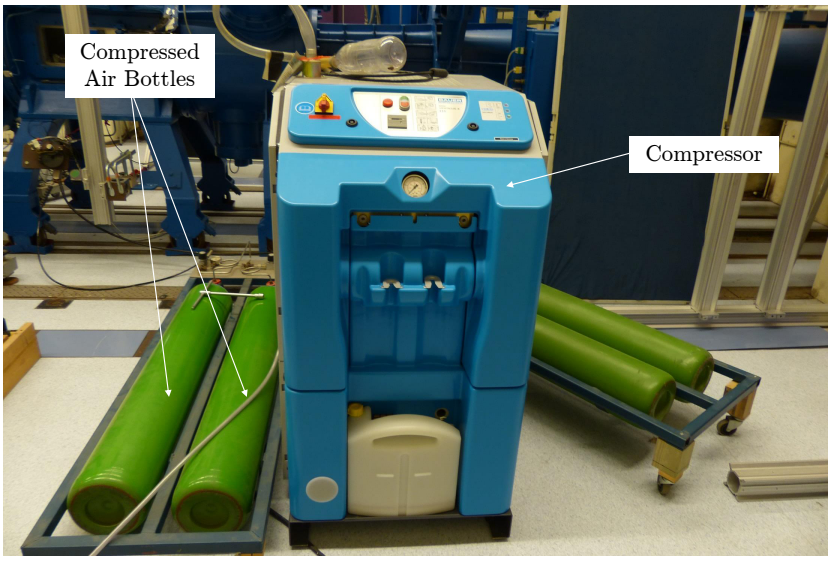

Figure 4.4: Compressed air bottles and the compressor

In order to investigate the effect of varying nozzle length, the nozzle length of the original FESTIP model has been modified. In Figure 4.3 the modified nozzle with extended length is

shown in dark green. The effective nozzle length is varied by sliding three different collars of the size 30 mm and 15 mm over the nozzle. In Figure 4.3, the position of these collars are indicated with red dotted lines. With these sliding collars, the present thesis investigate the following nozzle lengths: $L/D = 1.8$, 1.2, 0.9 and 0.6. As shown in Figure 4.3, a BL trip strip of 0.15 mm in diameter have been applied at about 40% of the nose in order to assure a fully developed, turbulent boundary layer. Furthermore, at the top the cylindrical main body is equipped with nine pressure taps. These pressure taps are connected to a Druck Ltd PDCR-22, 0-15 psi differential pressure transducer and used to determine the effective freestream Mach number. For the present experiment the number 8 pressure transducer (indicated as a red dot in in Figure 4.3), which is connected to the most upstream pressure tap at a distance of 65 mm from the base step corner, is used for the determination of the free stream Mach number during the experiments.

4.2.1 Exhaust Plume Simulation

Compressed air is used to simulate the exhaust plume during the wind tunnel experiments. It is relatively simple in setup and operation and it is more appealing when the simulation of jet temperature plays less importance. The nozzle of the modified FESTIP model has an area ratio between the nozzle exit and throat diameters of $A_e/A^* = 11.67$. This generates a supersonic jet with an exit Mach number of $M_{e,jet} = 4$. For the present investigation the goal was to simulate an exhaust plume that was similar to that of the Ariane 5 during its ascent at high-subsonic and supersonic speeds. During the wind tunnel experiments this was achieved by selecting a total jet pressure so that the ratio of static pressure at the nozzle exit and static freestream pressure was similar to the Ariane 5 when traveling at Mach 0.70 and 2.20. The total pressure in the settling chamber of the jet is regulated by the HP1000 computer system via a main valve, as seen in Figure 4.5.

According to Pindzola (1963), the pressure ratio and the Mach number are the most important flow parameters to be duplicated to achieve a similar initial inclination angle of the jet which is important to achieve a similarity in the pressure distribution in the base region. The following paragraph discusses in detail the calculations that has been performed to determine the selected total jet pressure during experiments.

Total Jet Pressure

To have a similar ratio of static pressure at the nozzle exit and static free stream pressure ($p_{e,jet}/p_\infty$) as during the actual ascent of the Ariane 5 traveling at $M_\infty = 0.70$ and $M_\infty = 2.20$, first the static pressure at the nozzle exit of the Ariane 5 ($p_{e,arian5}$) and the static free stream pressure ($p_{\infty,Ariane5}$) are determined. The static pressure at the nozzle exit of Ariane 5 is determined as follow:

$$p_{e,ariane5} = p_c \cdot \left(\frac{p_e}{p_c}\right) \tag{4.1}$$

In this equation p_c is the combustion chamber pressure of the Vulcian-2 rocket engine that

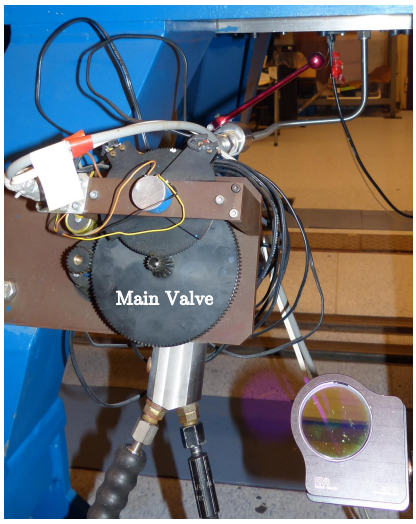

Figure 4.5: The main jet valve

powers the Ariane 5 ESC-A core stage and $\frac{p_e}{p_c}$ is the ratio between the pressure in nozzle exit and in reaction chamber. Using the expression for nozzle expansion ratio (A_e/A^*), as given in Equation (4.2) (Zandbergen, 2016), one can determine the pressure ratio $\frac{p_e}{p_c}$.

$$\frac{A_e}{A^*} = \frac{\sqrt{\gamma}\left(\frac{2}{\gamma+1}\right)^{\frac{\gamma+1}{2(\gamma-1)}}}{\sqrt{\frac{2\gamma}{\gamma-1}\cdot\left(\frac{p_e}{p_c}\right)^{\left(\frac{2}{\gamma}\right)}\left(1-\left(\frac{p_e}{p_c}\right)^{\left(\frac{\gamma-1}{\gamma}\right)}\right)}} \tag{4.2}$$

With specific heat ratio of $\gamma = 1.4$ for combustion gases, combustion chamber pressure of $p_c = 117.3$ bar for Vulcian-2 and nozzle expansion ratio of $A_e/A^* = 58.2$ (Coulon, 2000), a pressure ratio of $p_e/p_c = 0.0012$ is obtained using a numerical method. Inserting this obtained value into Equation (4.1) gives the static pressure at the nozzle exit of the Ariane 5 of $p_{e,ariane5} = 0.14$ bar.

The static free stream pressure and temperature during ascent of Ariane 5 at $M_\infty = 0.70$ and $M_\infty = 2.20$ depends on the altitude. The altitude at which Ariane 5 travel at $M_\infty = 0.70$ and $M_\infty = 2.20$ is obtained from the launch profile of the Ariane 5 (SpaceFlight101.com, Arianespace (2016)). Figure 4.6 show the launch profile (velocity as function of altitude) of the Ariane 5. Using the standard atmosphere, pressure and temperature are determined at the certain altitude (h), with the following equations (Anderson, 2004):

- For h $\leq$ 11000 m

$$p_1 = p_s\left(1 - a\frac{h_1}{T_s}\right) \tag{4.3}$$

$$T_1 = T_s + a\,(h_1 - h_0) \tag{4.4}$$

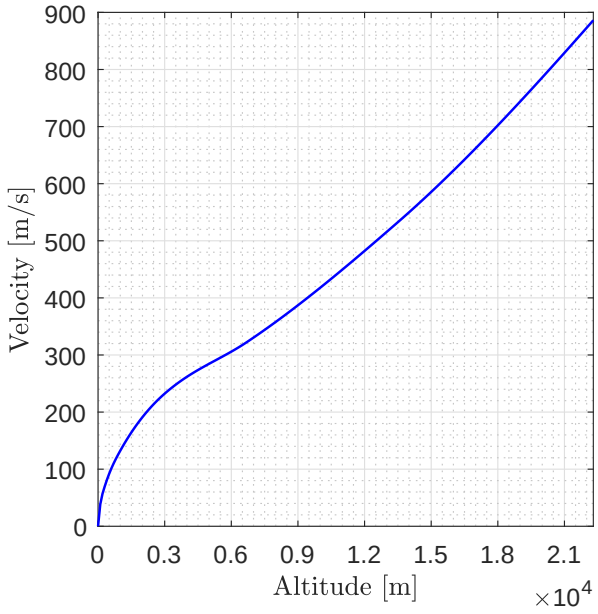

Figure 4.6: Ariane 5 launch profile

- For 11000 m $\leq$ h $\leq$ 25000 m

$$p_2 = p_1 \cdot e^{-\left(\frac{g_0}{RT_2}\right)(h_2 - h_1)} \tag{4.5}$$

$$T_2 = const = 216.66K \tag{4.6}$$

where a is the lapse rate, g_0 is the gravitational acceleration at sea level and R is the specific gas constant. From sea level (h = 0 m) up to an altitude of h = 11000 m, the lapse rate is equal to $a = -0.0065K/m$. The gravitational acceleration at sea level is 9.80 m/s^2 and the specific gas constant of air is $R = 287J/(kg * K)$. Furthermore, p_s and T_s are the pressure and temperature at sea level (h = 0 m). The determined values of the static free stream pressure and temperature as function of altitude (h), as well as the velocity of Araine 5 and its corresponding Mach number, are provided in Appendix A.

The exit pressure ratio (EPR) of the Ariane 5 is defined as follow:

$$EPR = \frac{p_{e,ariane5}}{p_{\infty,ariane5}} \tag{4.7}$$

This pressure ratio is used to obtain similar ratio of static pressure at the nozzle exit and static freestream pressure as during the ascent of the Ariane 5. From Equation (4.7), it follows that at $M_\infty = 0.70$ and $M_\infty = 2.20$ the exit pressure ratios are $EPR = 0.1982$ and $EPR = 1.5280$, respectively. By setting the ratio $p_{e,jet}/p_\infty$ equal to EPR of the Ariane 5, the following expression is obtained for the static jet pressure at the nozzle exit during the wind tunnel experiments:

$$\frac{p_{e,jet}}{p_\infty} = EPR \Rightarrow p_{e,jet} = p_\infty \cdot EPR \tag{4.8}$$

where the free stream static pressure in the wind tunnel (p_∞) is determined as follow:

$$p_\infty = p_0 \cdot \left(1 + \frac{\gamma - 1}{2} \cdot M_\infty^2\right)^{\left(-\frac{\gamma}{\gamma-1}\right)} \tag{4.9}$$

where p_0 is the total pressure in the settling chamber of the tunnel and M_∞ the freestream Mach number in the tunnel. The value of these two parameters are set during the wind tunnel experiments. Using isentropic relations and Equation (4.9), the total jet pressure that is selected during the experiment is computed as follow:

$$p_{0,jet} = p_{e,jet} \cdot \left(1 + \frac{\gamma - 1}{2} \cdot M_{jet}^2\right)^{\left(\frac{\gamma}{\gamma-1}\right)} \tag{4.10}$$

PIV and Schlieren experiments were carried out at $M_\infty = 0.70$ and $M_\infty = 2.20$, with total pressure of $p_0 = 2.0bar$ and $p_0 = 2.5bar$, respectively. For these flow conditions a total jet pressure of $p_{0,jet} = 43.40$ bar and $p_{0,jet} = 54.24$ bar is computed which will result in similar ratio of static pressure at the nozzle exit and static free stream pressure as during the ascent of the Ariane 5 traveling at $M_\infty = 0.70$ and $M_\infty = 2.20$, respectively. However, as will be discussed in the following paragraph, the computed total jet pressures caused condensation in the exhaust plume.

4.2.2 Exhaust Plume Condensation

From the PIV measurement with freestream Mach number of $M_\infty = 2.20$, total pressure of $p_0 = 2.5$ bar and total jet pressure of $p_{0,jet} = 54.24$ bar, condensation in the plume can be observed in the recording, as shown in Figure 4.2.2. In the recording the condensation in the plume is recognized as region with highest number of counts. This poses serious problems during the processing of the PIV data.

Condensation of plume, which consists of dry air (78.1 % N_2 and 20.9 % O_2) occur when total pressure in settling chamber is too high, which makes the expansion of jet flow of such magnitude that the temperature drops below the condensation temperature of air. When the (static) pressure in the plume goes beyond the vapor pressure of air, then condensation of the air in the plume may occur.

As such, in order to avoid condensation in the plume the vapor pressure of air is studied. The vapor pressure of air, which consist of 78.1 % N_2 and 20.9 % O_2, is determined using Antoine equation, as given in the following equations (NIST):

$$p_{vapor,N_2} = \left(10 \cdot \exp\left(A_{N_2} - \frac{B_{N_2}}{C_{N_2} + T}\right)\right) \tag{4.11}$$

$$p_{vapor,O_2} = \left(10 \cdot \exp\left(A_{O_2} - \frac{B_{O_2}}{C_{O_2} + T}\right)\right) \tag{4.12}$$

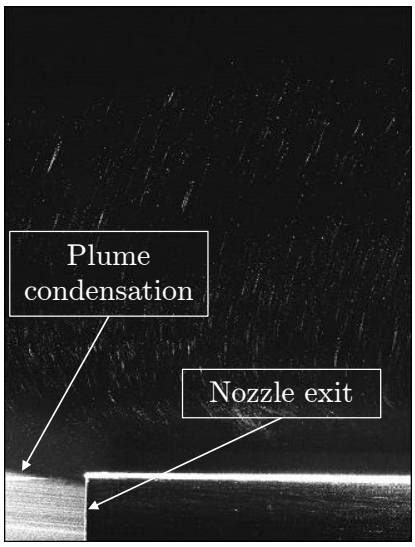

Figure 4.7: Condensation in the exhaust plume during PIV measurement

Gas	Temp. range [K]	A	B	C
Nitrogen (N_2)	63.14-126	3.7362	264.651	-6.788
Oxygen (O_2)	54.36-154.33	3.9523	340.024	-4.144

Table 4.1: Antoine equation parameters for nitrogen and oxygen

where T is the temperature and the Antoine equation parameters A, B and C for oxygen and nitrogen are given in Table 4.1. Using Dalton's law, the total vapor pressure of a mixture of nitrogen and of oxygen is expressed as follow:

$$p_{vapor,total} = p_{vapor,N_2} \times 0.781 + p_{vapor,O_2} \times 0.209 \tag{4.13}$$

In order to determine the occurrence of condensation in the plume, first the static temperature in the jet is determined as follow:

$$T_{e,jet} = T_{0,jet} \cdot \left(1 + \frac{\gamma - 1}{2} M_{jet}^2\right)^{-1} \tag{4.14}$$

where $T_{0,jet}$ is total jet temperature, which is 288 K. This temperature is then used to determine the vapor pressure of mixture of nitrogen and oxygen in the plume. In Figure 4.8 the total jet pressure as function of static jet pressure at the nozzle exit is provided, which illustrate the conditions for different jet Mach numbers at the nozzle exit. Condensation in the plume occur if the vapor pressure of mixture of nitrogen and oxygen is smaller than the static jet pressure ($p_{e,jet}$). Using Equation (4.14), for the nozzle with $M_{jet} = 4$, a static jet temperature of $T_{e,jet} = 67.4$ K is obtained. Inserting this computed temperature into Equation (4.11) and (4.12) and afterwards using Equation (4.13), a vapor pressure of $p_{vapor,total} = 0.19$ bar is obtained for the mixture of nitrogen and oxygen. Using Equations (4.8) and (4.9), a static jet pressure of $p_{e,jet} = 0.29$ bar and $p_{e,jet} = 0.36$ bar is computed for $M_\infty = 0.70$ and $M_\infty = 2.20$, respectively. The computed vapor pressure of mixture of nitrogen and oxygen is smaller than

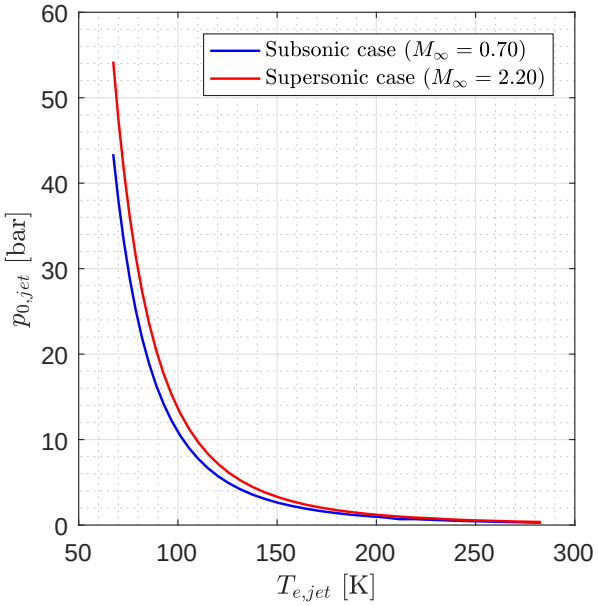

Figure 4.8: Total jet pressure ($p_{0,jet}$) as function of static jet temperature $T_{e,jet}$ at nozzle exit

the static jet pressures for both flow cases, therefore condensation in the plume occur. A way to avoid condensation in the plume is to have $p_{vapor,total} > p_{e,jet}$, but without changing $p_{e,jet}$ to maintain jet similarity. This can be achieved by lowering the jet Mach number at the nozzle exit from $M_{jet} = 4$ to $M_jet = 3.5$. For $M_{jet} = 3.5$ the vapor pressure of mixture of nitrogen is $p_{vapor,total} = 1.37$ bar, which is lager than for $M_{jet} = 4$ and thus condensation is avoided. It should be noted that for total jet pressure ($p_{0,jet}$) calculation for $M_{jet} = 3.5$ nozzle the same EPR is used as for $M_{jet} = 4.0$ case. A decrease in M_{jet} is achieved by increasing the throat diameter (d_t) of current the nozzle. Nozzle area ratio relation, as given in Equation (4.15) is used to determine the increased nozzle throat diameter corresponding to $M_{jet} = 3.5$.

$$\frac{A_e}{A^*} = \left(\frac{\gamma+1}{2}\right)^{-\frac{\gamma+1}{2(\gamma-1)}} \frac{\left(1+\frac{\gamma-1}{2}M_{jet}^2\right)^{\frac{\gamma+1}{2(\gamma-1)}}}{M_{jet}} \tag{4.15}$$

$$d_t = \sqrt{\frac{4}{\pi}\cdot A^*} \tag{4.16}$$

Inserting $M_{jet} = 3.5$ give an nozzle area ratio of $A_e/A^* = 6.79$. With known value of the nozzle exit area of $A_e = 16.40\ mm$, the nozzle throat area becomes $A^* = 31.112\ mm^2$. Finally, using Equation (4.16) a throat diameter of $d_t = 6.294\ mm$ is obtained. A redesign of the nozzle with increased throat diameter (d_t) is provided in Appendix B.

An overview of all the known and calculated parameters for Ariane 5 nozzle and current nozzle configurations with $M_{jet} = 3.5$ and $M_{jet} = 4.0$, are provided in Tables 4.2, 4.3, 4.4 and 4.5.

Ariane 5	**Mach = 0.70**	**Mach = 2.20**
Chamber Pressure (p_c)	117.3 bar	-
Pressure Ratio ($\frac{p_e}{p_c}$)	0.0012	-
Exit pressure ($p_{e,ariane5}$)	0.14 bar	-
Expansion ratio (A_e/A^*)	58.2	-
Height (h)	2900 m	16700 m
Temperature (T)	269.30 K	216.65 K
Ambient pressure (p)	0.71 bar	0.09 bar
EPR	0.1982	1.5280

Table 4.2: Araine 5 nozzle parameters

	M_{jet} **= 3.5**		M_{jet} **= 4.0**	
	Tunnel (nominal)	**Plume (nominal)**	**Tunnel (nominal)**	**Plume (nominal)**
Mach	0.70	3.5	0.70	4.0
Total pressure	2.5 bar	27.2 bar	2.5 bar	54.25 bar
Static pressure	1.80 bar	0.36 bar	1.80 bar	0.36 bar
Total temperature	283 K	-	283 K	-
Static temperature	257.74 K	82.03 K	257.74 K	67.38 K

Table 4.3: Nozzle flow properties for $M_\infty = 2.20$ flow case

	M_{jet} **= 3.5**		M_{jet} **= 4.0**	
	Tunnel (nominal)	**Plume (nominal)**	**Tunnel (nominal)**	**Plume (nominal)**
Mach	2.20	3.5	2.20	4.0
Total pressure	2.0 bar	21.80 bar	2.0 bar	43.40 bar
Static pressure	0.19 bar	0.29 bar	0.19 bar	0.29 bar
Total temperature	283 K	-	283 K	-
Static temperature	143.80 K	82.03 K	143.80 K	67.38 K

Table 4.4: Nozzle flow properties for $M_\infty = 0.70$ flow case

		M_{jet} **= 3.5**		M_{jet} **= 4.0**	
Component	**Composition share**	p_{vapour} **[bar]**	**Condensation [Yes/No]**	p_{vapour} **[bar]**	**Condensation [Yes/No]**
Nitrogen (N_2)	0.78	1.66	No	0.23	Yes
Oxygen (O_2)	0.21	0.39	No	0.04	Yes
Total vapour pressure	0.99	1.37	No	0.19	Yes

Table 4.5: Vapour pressure results for $M_{jet} = 3.5$ and $M_{jet} = 4.0$

4.3 Experimental Campaigns and Flow Conditions

The experimental investigations for the present thesis were divided into two campaigns, the first campaign being Schlieren and the second one planar PIV. The main purpose of the Schlieren campaign was to identify the topological flow features in the wake of an axisymmetric BFS but also to investigate the proper start-up of the wind tunnel. The main purpose of the PIV campaign was to obtain velocity fields in the wake of an axisymmetric BFS at subsonic and supersonic flows in order to be able to determine the mean flow field properties, such as mean velocity field and mean pressure distribution. Section 4.3.1 discusses the relevant flow conditions for the Schlieren and PIV campaigns. In section 4.3.2 the test matrices for the Schlieren and PIV experimental campaigns are provided.

4.3.1 Flow Conditions

Table 4.6 provides the most relevant flow conditions for the Schlieren and PIV experimental campaigns. The 'freestream' conditions, denoted by ∞, refers to the flow conditions over the cylindrical main body of the model. The freestream Mach number (M_∞) and the total pressure (p_0) in the settling chamber was set by the wind tunnel operator. The total temperature (T_0) in the settling chamber was measured before the wind tunnel run. The freestream pressure (p_∞) was measured via a pressure sensor in the cylindrical main body located 65 mm upstream of the base edge (see Figure 4.3). For the present investigation, the wind tunnel was operated at nominal Mach numbers of $M_{nom} = 0.70$ and $M_{nom} = 2.20$. As a result of blockage effects, the effective freestream Mach number (M_∞) for the subsonic case was $M_\infty = 0.76$. Knowing these, all the other freestream parameters have been determined using isentropic relations and Sutherlands law of viscosity.

With the known freestream Mach number, total pressure and temperature in the settling chamber, the freestream static temperature have been calculated using isentropic relatios:

$$\frac{T_0}{T_\infty} = 1 + \frac{\gamma - 1}{2} M_\infty^2 \tag{4.17}$$

Where $\gamma = 1.4$ is the specific heat ratio of air. Using ideal gas law, with the assumption that the gas is calorically perfect, the density in the freestream is computed as follow

$$\rho_\infty = \frac{p_\infty}{R T_\infty} \tag{4.18}$$

In this equation R = 287.058 $J \cdot \left(kg^{-1}K^{-1}\right)$ is the ideal gas constant of air. The dynamic viscosity in the freestream is determined using Shuterlands law:

$$\mu_\infty = \mu_{ref} \cdot \left(\frac{T_\infty}{T_{ref}}\right)^{1.5} \cdot \left(\frac{T_{ref} + S}{T_\infty + S}\right) \tag{4.19}$$

Where μ_{ref} and T_{ref} are the reference dynamic viscosity (μ_{ref}) and temperature and S is the Sutherlands constant. According to White (2005), $\mu_{ref} = 1.716 \times 10^{-5}$ $J \cdot \left(kg^{-1}K^{-1}\right)$,

$T_{ref} = 273\ K$ and $S = 111\ K$. Finally, the freestream velocity and the Reynolds number based on the diameter ($D = 50mm$) of the cylindrical main body are computed as follow:

$$U_\infty = M_\infty \cdot \sqrt{\gamma R T_\infty} \tag{4.20}$$

$$\mathrm{Re}_D = \frac{\rho_\infty U_\infty D}{\mu_\infty} \tag{4.21}$$

Parameter	Symbol	Units	Subsonic	Supersonic
Free stream Mach number	M_∞	[-]	0.76 ± 0.01	2.20 ± 0.01
Total pressure	p_0	[bar]	1.98 ± 0.01	2.48 ± 0.01
Free stream pressure	p_∞	[bar]	1.38 ± 0.01	0.23 ± 0.01
Total temperature	T_0	[K]	273 ± 3	277 ± 3
Free stream velocity	U_∞	$[m \cdot s^{-1}]$	239 ± 3	534 ± 3
Reynolds number	Re_D	[-]	1.5×10^6	3.3×10^6
Jet Mach number at nozzle exit	$M_{e,jet}$	[-]	3.5	3.5
Total jet pressure	$p_{0,jet}$	[bar]	22 ± 2	27 ± 2
Static jet pressure at nozzle exit	$p_{e,jet}$	[bar]	0.28 ± 0.01	0.36 ± 0.01
Total jet temperature	$T_{0,jet}$	[K]	< 288	< 288
Nozzle pressure ratio	$NPR = \frac{p_{0,jet}}{p_{e,jet}}$	[-]	76	75

Table 4.6: Flow conditions

4.3.2 Test Matrices

Table 4.7 show the experimental test matrix for the Schlieren and PIV experimental campaigns. During the Schlieren campaign, four different nozzle configuration ($L/D = 0.6$, 0.9, 1.2, 1.8) have been tested at $M_\infty = 0.76$ (subsonic) and $M_\infty = 2.20$ (supersonic) with and without the exhaust plume. For the subsonic cases, the total pressure in the settling chamber was set to $p_0 = 2.0$ bar, whereas for the supersonic cases it was set to $p_0 = 2.5$ bar. For the subsonic case with exhaust plume, the total jet pressure was set to $p_{0,jet} = 22$ bar whereas for the supersonic it was set to $p_{0,jet} = 27$ bar. The same experimental flow conditions have used during the PIV campaign.

Campaign	Technique	Config. (L/D)	$p_{0,jet}$ [bar]	M_∞ [-]	p_0 [bar]
1	Schlieren	0.6	off	0.7	2.0
			22		
		0.9	off		
			22		
		1.2	off		
			22		
		1.8	off		
			22		
		0.6	off	2.2	2.5
			27		
		0.9	off		
			27		
		1.2	off		
			27		
		1.8	off		
			27		
2	PIV	0.6	off	0.7	2.0
			22		
		0.9	off		
			22		
		1.2	off		
			22		
		1.8	off		
			22		
		0.6	off	2.2	2.5
			27		
		0.9	off		
			27		
		1.2	off		
			27		
		1.8	off		
			27		

Table 4.7: Experimental test matrix for the Schlieren and PIV campaigns

4.4 Schlieren Apparatus and Setup

A *z-type* schlieren setup for the present experiment is shown in Figure B. A photograph of the Schlieren setup from both sides of the wind tunnel are shown in Figures 4.11 and 4.12, respectively. As shown, the setup consist of Xenon flash lamp (spark light) as a light source, two large parabolic mirrors with focal length of 3.5 m, two plane mirrors, a pinhole, two lenses with $f = 200$ and $f = 180$, a knife edge and a high speed camera.

The Instantaneous flow features, such as separated shear layer, generates a very strong den-

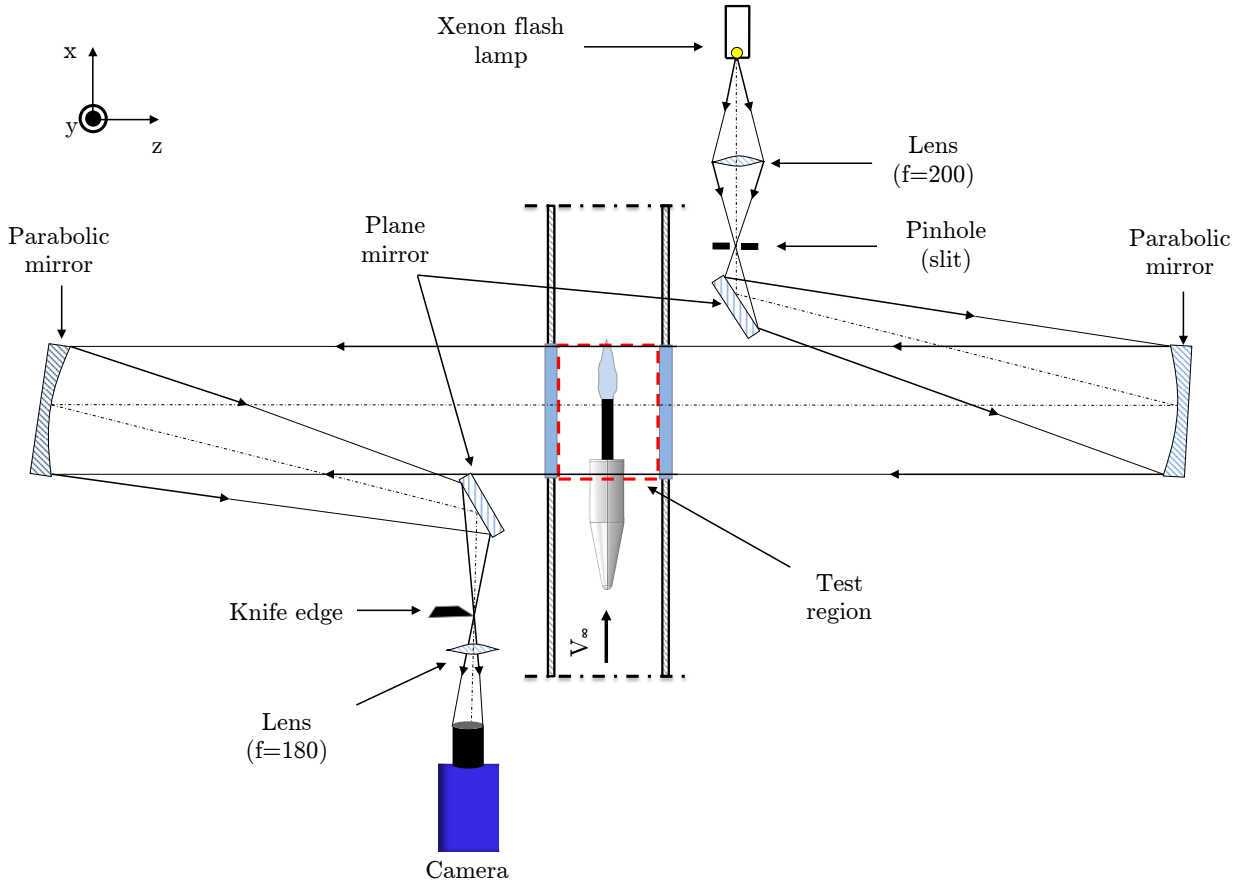

Figure 4.9: Schematic of the Schlieren setup, top view

sity gradient in the wake of an axisymmetric BFS as a result of vortex roll-up and pairing mechanisms. The speed of the convective vorticies are very high. In order to record these high-speed convective vorticies in great detail, a Xenon flash lamp (spark light) is used. This flash lamp has a low exposure time of 20 ns and it acts as point light source. The *MINISTROBOKIN* generator is used to operate Xenon flash lamp on external triggering up to 10 kHz at approximately 220 V. In order to avoid loss of the light, a tube insulation with length of 10 cm is used. Using a lens with $f = 200$ and a pinhole, the light coming from the Xenon flash lamp (point source) is converted into a beam of light. The lens is used to focus the light coming from the light sources and the purpose of the pinhole is to control the thickness of the light beam. The back side of the pinhole is covered with a transparent tape in order to avoid diffusion. A plane mirror directs the light beam passing the pinhole into the direction of the parabolic mirror. A collimated beam of light, formed by the parabolic mirror, crosses through the test region. A second parabolic mirror and a plane mirror is used to focus the collimated beam of light passing through the test region at the location where the knife edge is placed. This knife edge blocks the light which is bent due to the density field resulting into a visualization of the density gradient of the flow field. Horizontal Schlieren knife orientation is used for the present experiment in order to visualize vertical gradients

(e.g. shock/expansion systems, boundary layer). Directly after the knife edge a lens with $f = 180$ placed in order to focus the light beam into the lens of high-speed camera. The camera used for the Schlieren setup is Lavision Imager pro HS 4M (Figure 4.10). It has a 4 Megapixel resolution (2016 $\times$ 2016 pixels) and 12 bit CCD sensor. The recorded images from

Figure 4.10: Lavision Imager pro HS 4M camera. Courtesy of *Lavision*

the camera are transferred via CAT-5 ethernet cable to a PC. Furthermore, the camera and the *MINISTROBOKIN* generator are connected via RG-56 cable and BNC connectors to a Lavision High Speed Controller PTU which triggers the camera and the light source. The controller is also connected to a PC via USB cable. DaVis 8.3.1 software from Lavision is used to control the camera and the light source and also to process the recorded data.

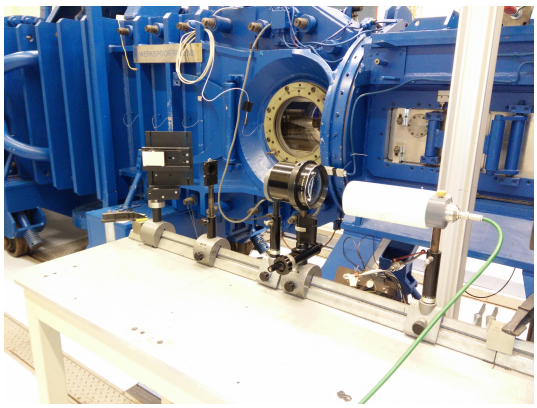

Figure 4.11: Schlieren setup

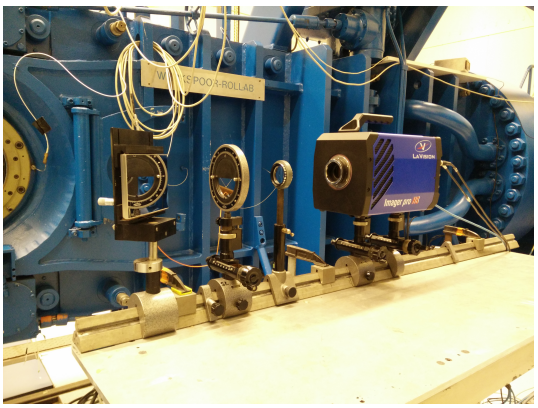

Figure 4.12: Schlieren setup

4.5 Planar PIV Setup and Apparatus

Planar PIV measurements were conducted in the base region of the modified FESTIP model (Figure 4.3). The field of view (FOV) of the base region that is investigated during the PIV measurements is shown in Figure 4.13. The size of this FOV, which is the region with orange grid lines, is 140 *mm* by 50 *mm* (width×height), which is similar for all the 16 cases considered for the present investigation (4 nozzle lengths; 2 Mach numbers; with and without exhaust plume). The size of the FOV is also selected such that both the in-flow boundary layer on top of the model before the step and the presence of an exhaust plume is investigated. Figure 4.14 show the planar PIV setup installed in the TST-27 wind tunnel to investigate

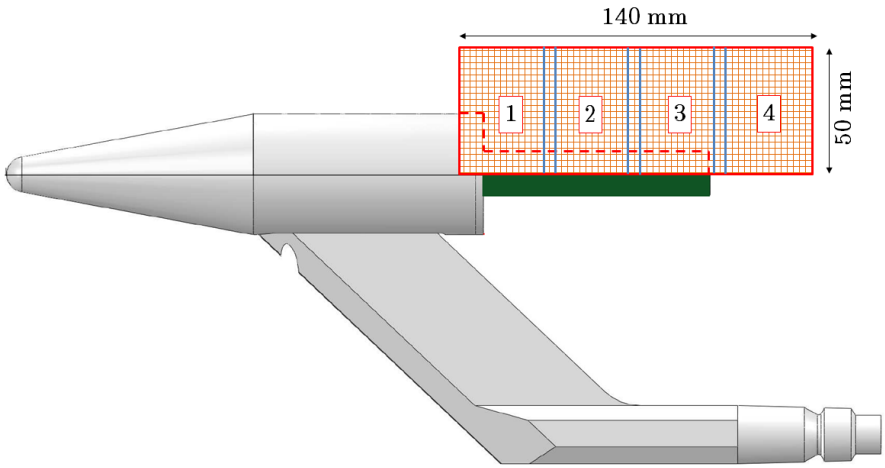

Figure 4.13: The Field of View (FOV)

the FOV shown in Figure 4.13. This setup consist of the following components: 4 cameras, modified FESTIP model, an illumination source (not shown in Figure) and a seeding system (not shown in Figure). The 4 camera setup is used to obtain a large FOV in the base region of the model without losing the spatial resolution. As such, the FOV as shown in Figure 4.13 is divided into four equal sizes of 35 *mm* with an overlap of approximately 4 *mm*.

4.5.1 CCD Cameras

For the planar PIV experiments, 4 LaVision Imager LX 2MP interline CCD cameras, fitted with a Nikon lens of 105 *mm* is used to capture the flow field of interest (Figure 4.15). This camera has a maximum resolution of 1628 by 1236 pixels with a pixel pitch of 4.40 μm and lowest shutter speed of 1.0 μs. It record 14 bits images and the recorded images are transferred via CAT-5 cable to a PC. The camera is connected via RG-56 cable and BNC connectors to the LaVision external PTU (Figure 4.16). This external PTU which is connected to a PC via an USB cable, triggers the camera (and the laser). Lavision DaVis software, versions 8.1.2 and 8.3.1, respectively are used to control the camera (and the laser) and also to process the recorded data.

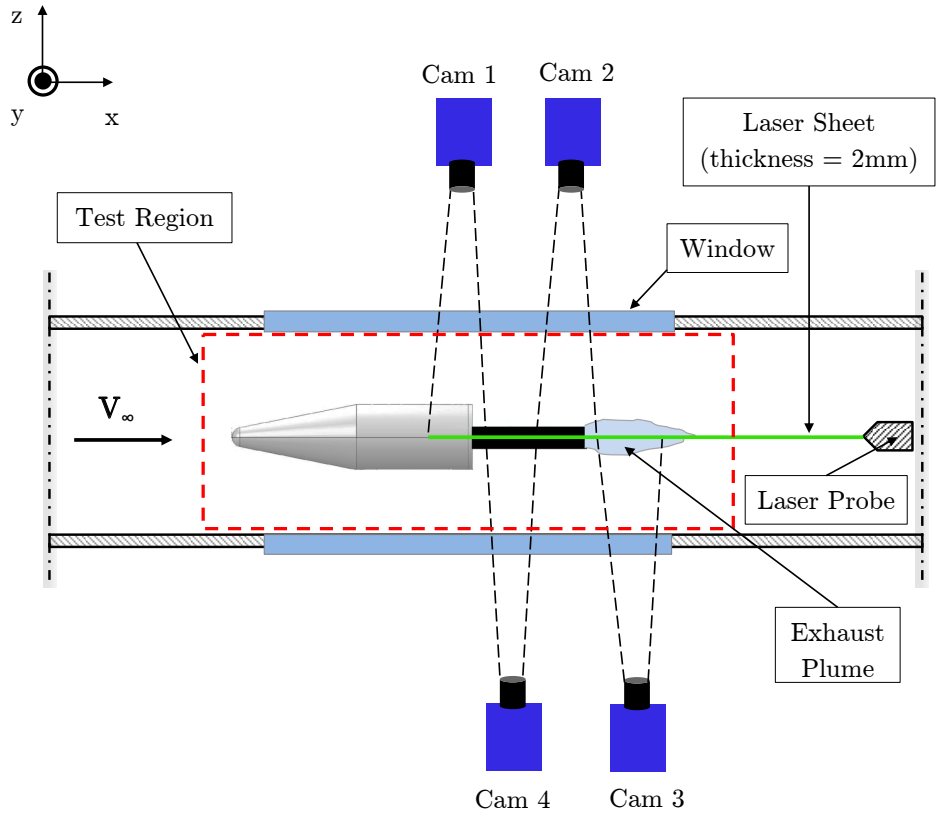

Figure 4.14: Planar PIV setup, top view

4.5.2 Illumination

For the PIV experiments, a Spectra Physics Quanta-Ray PIV-400 Neodymiumdoped Yttrium Aluminium Garnet (Nd:YAG) laser is used to illuminate the required FOV. This laser emits green light with wavelength of 532 nm by converting the infra red light with a wavelength of 1064 nm. The maximum energy provided by this laser is 400 mJ per pulse. Its pulse duration for $\lambda = 532nm$ is between 5-10 ns and the repetition rate increases up to 10 Hz. A control unit together with a remote control are used to turn the laser system on & off (Figure 4.17). Triggering of the laser during a measurement campaign happens via a LaVision external PTU and DaVis 8.3.1 software. During the operation of the laser, water is used to cool down the system and nitrogen gas is used to keep the optical components of the laser system dry and clean.

As shown in Figure 4.17 and 4.18, the laser beam is guided inside the wind tunnel through a series of mirrors that are mounted outside the tunnel and a laser probe that is installed downstream of the test region. The laser probe is equipped with set of lenses and mirrors to form a diverging laser sheet from the laser beam.

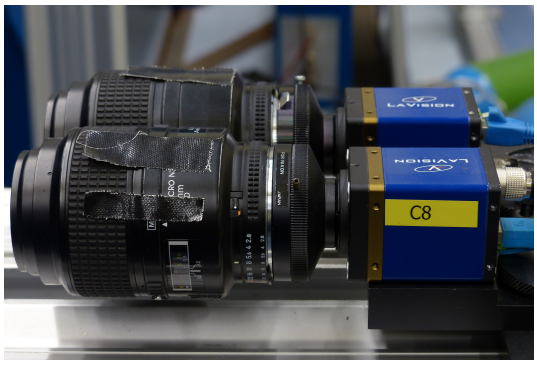

Figure 4.15: LaVision Imager LX 2MP camera with 105mm Nikon lens

Figure 4.16: LaVision external PTU

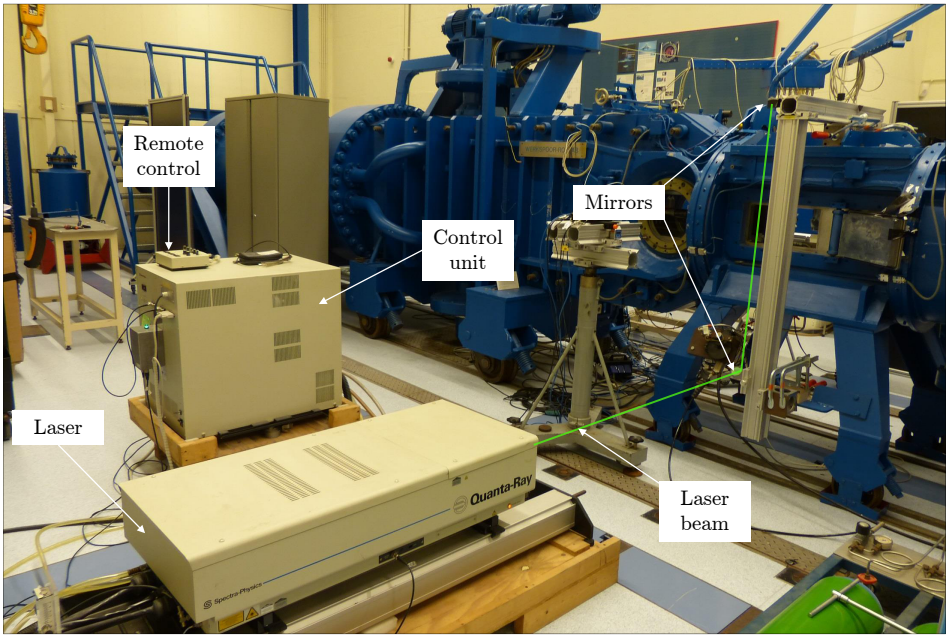

Figure 4.17: Spectra Physics Quanta-Ray PIV-400 system and illustration of the laser beam path

4.5.3 Seeding

Throughout the PIV experiments the flow in the wind tunnel was seeded with Titanium Oxide ($TiO2$) particles of the type Kemira P580. The particles have a primary crystal size of 30 nm (the actual particles form agglomerates of approximately 500 nm (Schrijer et al., 2006)), a nominal density of 150 kgm^{-3} and a particle response time of $\tau_p = 2.56$ μs (Ragni et al., 2011).

The $TiO2$ particles were injected into the wind tunnel via a seeding rake placed in the settling chamber, which was connected via a hose to a high-pressure cyclone seeding generator

Figure 4.18: Laser probe inside the wind tunnel

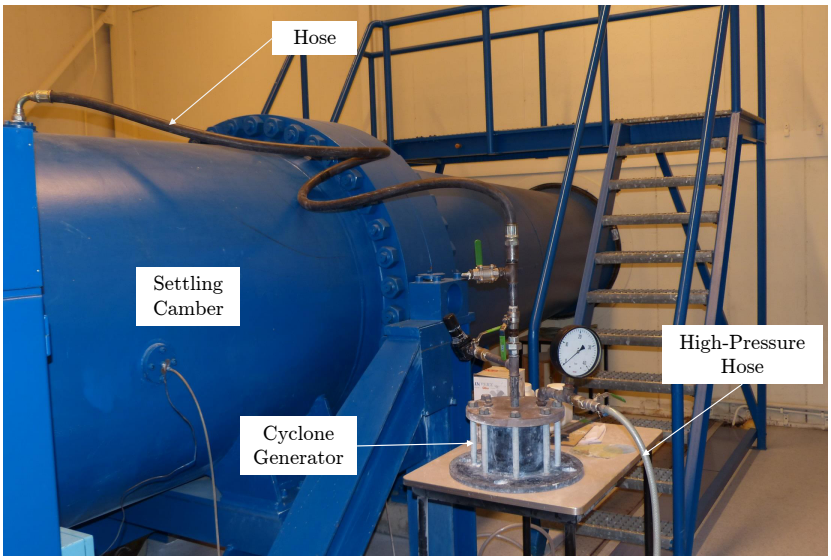

Figure 4.19: $TiO2$ seeding system

operating at 10 bars (see Figure 4.19). The high-pressure inside the cyclone generator is created through a hose which was connected to the pressurized air system of the TST-27 wind tunnel. The valve that controls the pressurized air system is located in the control room of the TST-27 wind tunnel.

4.5.4 PIV Parameters

Table 4.8 summarizes the PIV experimental parameters.

Parameter	Unit	Subsonic	Supersonic
FOV	mm^2	140×50	140×50
FOV overlap	mm	4.0	4.0
Focal length	mm	105	105
$f_{\#}$	-	8.0	8.0
Digital resolution	$pixel/mm$	30.3	30.3
Magnification factor	-	0.19	0.19
f_{acq}	Hz	5.0	5.0
Δt	μs	2.5	1.0
Image pairs	-	500	500
Measuring time	s	15.0	15.0
Laser power	%	70/75	70/75
Window size	$pixels$	48 × 48	48 × 48
Vector spacing	mm	0.40	0.40

Table 4.8: Planar PIV parameters

4.5.5 Reflection Problems and Solution

When conducting PIV measurements, it is very important to have good image quality. The illuminated particle images that are recorded during the PIV experiments should have higher intensity than the background or the camera noise.

Figure 4.20(a) shows a raw image of single exposure PIV recording that was captured by one of the four cameras during the PIV measurement. In this figure, a strong reflection above the external surface of the nozzle is observed. This region with reflection arises due to the impingement of the laser light on the external surface of the model. It has higher intensity than the surrounding scattering $TiO2$ particles. The region with reflection causes undesirable effect during the analysis of the recorded images performed by cross-correlation. According to Sciacchitano and Scarano (2014) these regions with reflection dominate the correlation map introducing a self-correlation stripe-like region of high intensity that typically precludes the detection of the displacement peak. Because the light reflection dominates the pixel intensity with respect to particles peak, even when the correlation window minimally includes the reflection region, the cross-correlation signal degrades and an erroneous vector estimate (outlier) is produced. Figure 4.20(b) shows an instantaneous vertical velocity vector field contour that was obtained by using filters at an image pre-processing stage to deal with the undesired effect of laser light reflections. However, still outliers can be observed in the region with reflections.

Since the filters used during pre-processing did not solve the issues related to reflections, the following methods haven been used during the experiments to avoid reflection.

- Spraying the model with black paint and using black tape
- Reducing the laser power

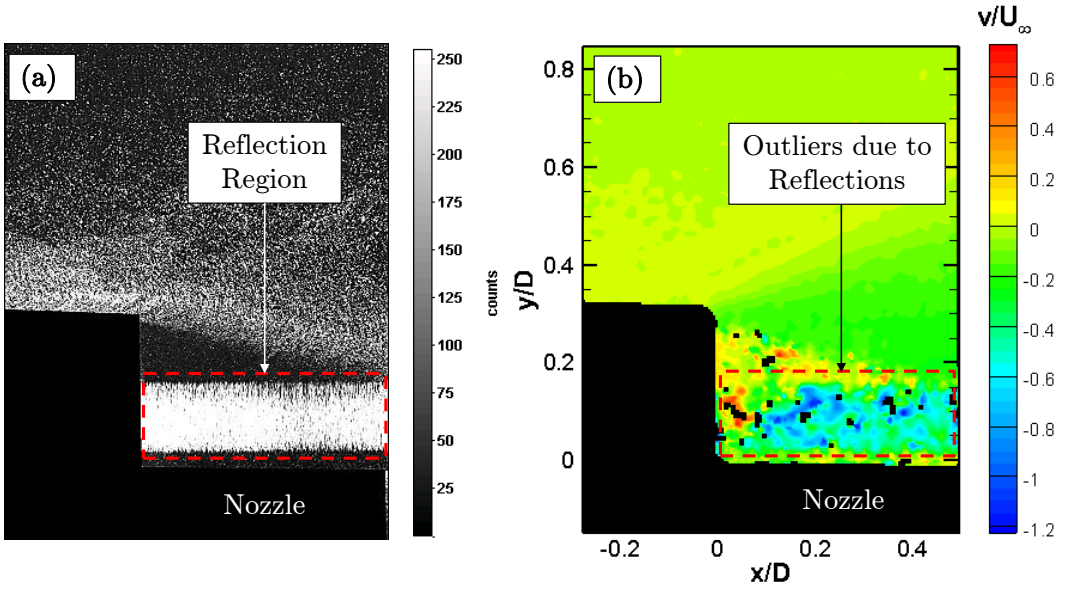

Figure 4.20: (a) Raw image of single exposure PIV recording. (b) Instantaneous vertical velocity vector field contour

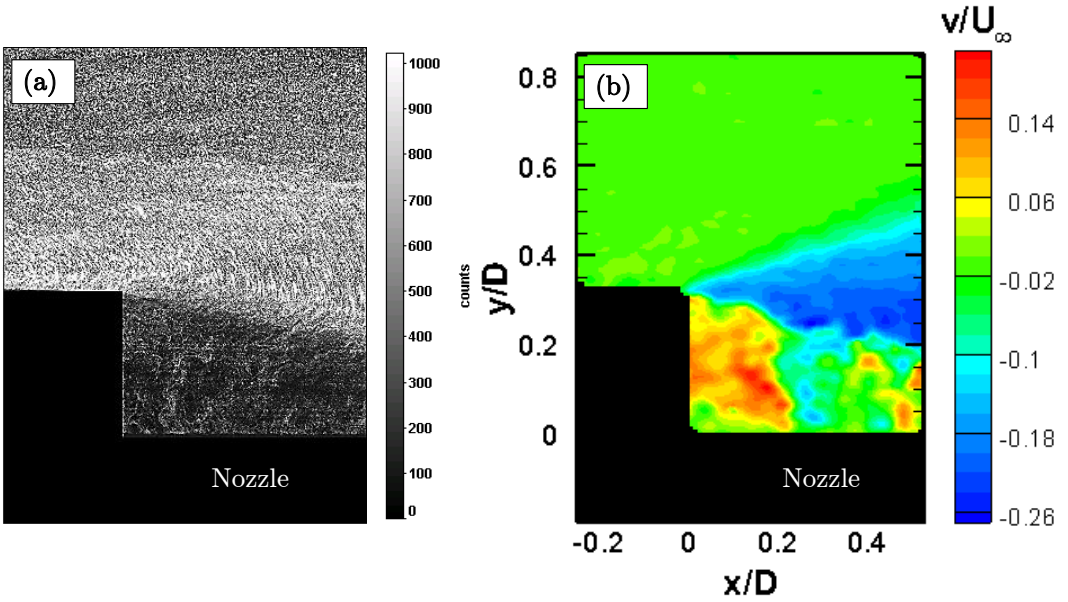

Figure 4.21: (a) Raw image of single exposure PIV recording without reflection. (b) The corresponding instantaneous vertical velocity vector field contour

- Cleaning the surface of the model and windows after each wind tunnel run
- Changing the height of the laser probe
- Positioning the camera at a small angle

The model and support sting are made of stainless steel, which has a high reflectivity. In order

to mitigate laser light reflection, the nozzle is sprayed with black paint and the cylindrical main is covered with black tape (Figure 4.22). The main body is not painted due to the

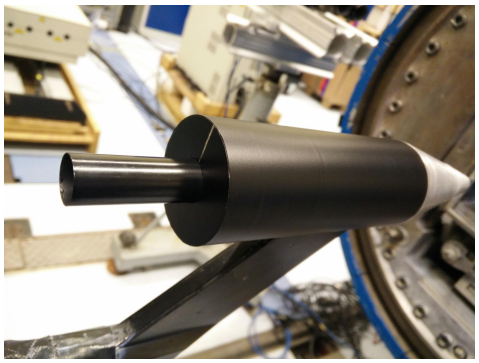

Figure 4.22: Painted nozzle and taped main body

presence of pressure taps on the upper part. For the future experiments it is recommended to use models made of aluminum materials with a highly polished surface because of its very low diffuse reflectivity with respect to steel or other materials. After each wind tunnel run the surface of model, both windows and the laser probe mirror were cleaned from the seeding with ethanol in order to minimize reflection. Additionally, by lowering the height of the laser probe and positioning the cameras, not perpendicular to the region of interest but with small angle ($\approx 1^{\circ}$), the reflection problems have been solved.

4.6 PIV Image Acquisition & Processing

4.6.1 Image Acquisition

Before recording, the 4 LaVision Imager LX 2MP cameras were calibrated. A self made calibration plate made of millimeter graph paper was used to calibrate the cameras (see Figure 4.23). The cameras were calibrated everyday before the PIV measurements by first aligning the calibration plate with laser sheet and then taking a picture of the FOV corresponding to each camera. A perspective image calibration of Davis, with a polynomial of 3rd order was performed on the taken pictures until all the 4 camera achieved RMS fit lower than 0.25 pixels. After the calibration procedure, the PIV experiments were conducted where 500 images were recorded in four runs of 125 images for each of the 16 cases studied.

4.6.2 Image Pre-processing & Vector Computation

This paragraph explain the steps followed to pre-process the raw PIV images. The recording and pre-processing of the PIV images were done using Lavision DaVis software, versions 8.1.2 and 8.3.1, respectively.

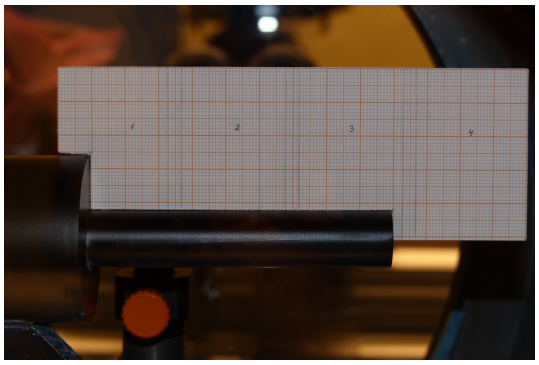

Figure 4.23: Millimeter graph paper calibration plate

Image pre-processing is of considerable importance before performing vector computation. Its main purpose is to remove background illumination but also to reduce the effect of noise and the reflections that is captured by the cameras. As a result of this image pre-processing, the quality of raw images enhances. In the following, the pre-processing step performed on the raw PIV images are explained.

1. **Subtract time filter** In order to enhance the contrast of the raw PIV images, the obtained local minimum intensity in each run is subtracted from all the raw images of that particular run. The local minimum intensity is single image.

2. **Add geometric mask** The model is geometrically masked to mitigate regions with reflections and other artifacts that has negative impact on the derived results. To make sure that each run from the same case to be pre-processed has the same mask, the added geometric mask was saved.

3. **Make mask permanent** Permanent mask is applied on the geometric mask to set the disabled pixel values to zero.

4. **Subtract sliding minimum** The contrast of the resulting intensity is enhanced by subtracting the minimum intensity within 16 pixel-sized kernels.

5. **Min-max filter for intensity normalization** This filter is applied to normalize the resulting intensity with a kernel of 6 pixels.

The effect of these performed pre-processing steps on raw PIV images can be seen in Figure 4.24.

After completing the pre-processing steps of the PIV data, the computation of the velocity vector fields is performed. For this purpose DaVis software is used. Velocity vector fields were computed using multi-pass correlation procedure of decreasing window size. The initial iteration starts with an interrogation window size of 96×96 pixels, with no window weighting function (square) and an overlap of 75%. The final three iterations were carried out with an interrogation window size of 48×48 pixel, with Gaussian window weighting function (Elliptical,

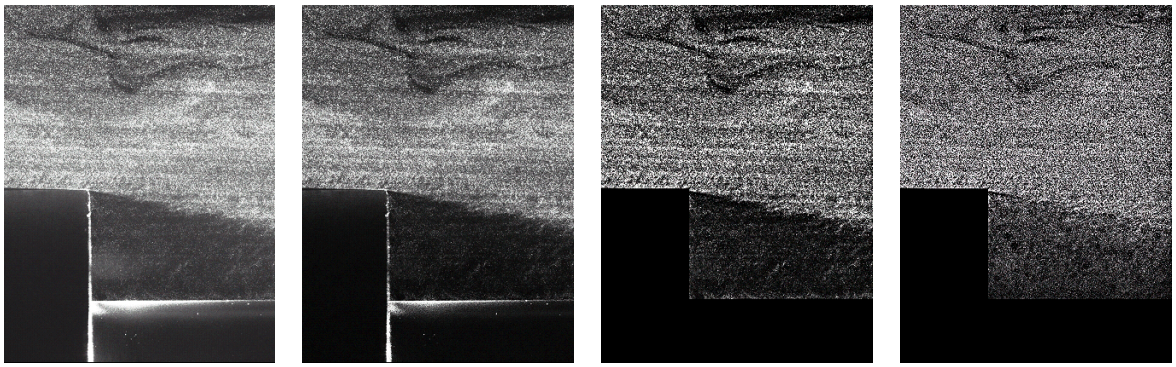

(a) Raw PIV image

(b) Subtract time filter

(c) Masking + Subtract sliding minimum

(d) Min-max filter for intensity normalization

Figure 4.24: The effect of pre-processing steps on raw PIV images

2:1) and an overlap of 75%, resulting in a vector spacing of 0.40 mm. The multi-pass post-processing is performed with the universal outlier detection of DaVis. It detects the spurious vector that are outside the standard deviation of a filter region of 5×5. After computation of the velocity vector field, based on visual inspection it is observed that approximately 5 - 15% of the computed velocity vector fields were deemed to suffer from insufficient seeding quality, depending on the case considered. As such, before performing post-processing with Davis, these velocity vector fields which suffered from insufficient seeding quality, haven been removed manually.

After completing the computation of velocity vector field, the post-processing of the vector fields are performed in order to discard the outliers. This is done by using the universal outlier detection with same filter region as used for velocity vector computation but now the groups with less 5 vectors are discarded and replaced. Figure 4.25 show the computed velocity vector field snapshot before and after performing vector post-processing with universal outlier detector. After completion of vector post-processing, the average velocity vector fields, the Reynolds stresses (Re_{xy}, Re_{xx}, Re_{yy}), turbulent kinetic energy and standard deviations of the set of post-processed vector fields have been obtained using DaVis.

4.6.3 Merging of Vector Fields

The vector fields that were obtained from 4 cameras after post-processing are 4 separate vector fields. These 4 vector fields were merged to each other using Tecplot software. The merged vector fields were transferred to a common grid by applying linear interpolation with Tecplot. Before merging the separate vector field, first approximately 5 vectors at left and right side of each vector field is removed. During merging of the vector fields the same overlap of 4 mm minus the vectors that were removed from left and right side was used. The final grid consists of 420×137 (L×H) points with a similar spacing as in the original vector fields.

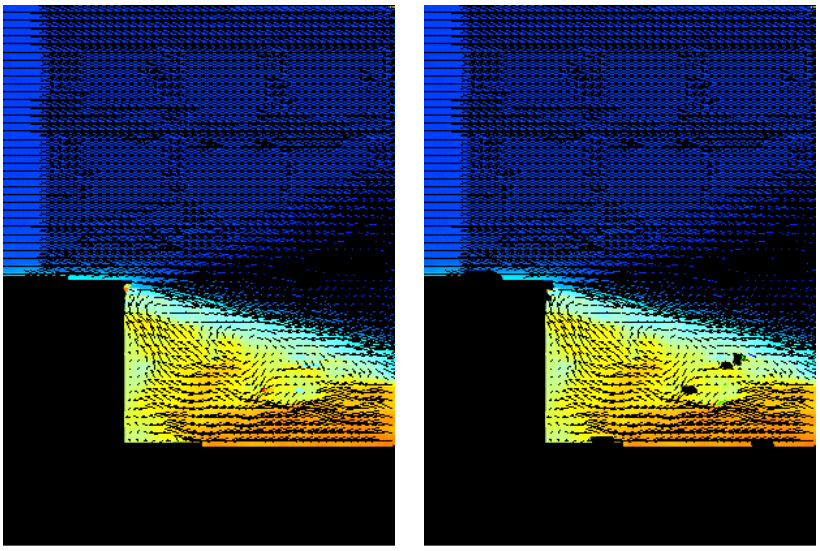

(a) Multi-pass post-processing (b) Vector post-processing

Figure 4.25: Velocity vector field before and after post-processing with outlier detection

4.7 PIV Uncertainty Analysis

This section outlines the uncertainty analysis of the measured properties obtained from the PIV experiments. Uncertainty analysis of the obtained experimental data is a crucial part, which is required to evaluate the accuracy of the measured properties. The accuracy indicates the difference between experimentally measured value of a quantity and the true value. This difference is defined as an error and is used to quantify the uncertainty (Stern et al., 1999). Two significant sources of uncertainty in the present planar PIV experiments are the limited ensemble size and the uncertainty resulted from the planar PIV measurements, such as cross-correlation, particle slip and spatial resolution. These main sources of uncertainties will be defined and discussed in the following sections. In the last section a summary of the results of the discussed sources of uncertainties will be provided.

4.7.1 Uncertainty From Ensemble Size

The present thesis investigated the mean flow properties and mean pressure distribution. These mean flow field properties were obtained from the ensemble average of all the PIV recorded images. The mean flow field uncertainties associated to the limited ensemble size will be discussed here.

The uncertianty analyses of mean velocities, RMS velocity fluctuations and Reynolds shear stress, related to the finite ensemble size (N) follow those introduced by Benedict and Gould (1996). These expression are also discussed by Sun (2014) and Humble (2009). The uncer-

tainties associated to the mean streamwise and radial velocity components ($\bar{u}$, $\bar{v}$) can be seen in Equation (4.22).

$$\varepsilon_{\bar{u}} = \frac{\sqrt{\overline{u'^2}}}{\sqrt{N}} = \frac{\langle u' \rangle}{\sqrt{N}} \qquad \varepsilon_{\bar{v}} = \frac{\sqrt{\overline{v'^2}}}{\sqrt{N}} = \frac{\langle v' \rangle}{\sqrt{N}} \tag{4.22}$$

Where N is the ensemble size, u' and v' are the streamwise and radial velocity components fluctuations, $\langle u' \rangle$ and $\langle v' \rangle$ are the RMS of velocity fluctuations. The intensity of the fluctuation in the wake region of BFS is higher than in the freestream. As such, higher uncertainties of the mean velocities in that region is expected.

The expressions for the uncertainty of the RMS of the streamwise and radial velocity components fluctuation are given in Equation (4.23).

$$\varepsilon_{\langle u' \rangle} = \frac{\sqrt{\overline{u'^2}}}{\sqrt{2N}} = \frac{\langle u' \rangle}{\sqrt{2N}} \qquad \varepsilon_{\langle v' \rangle} = \frac{\sqrt{\overline{v'^2}}}{\sqrt{2N}} = \frac{\langle v' \rangle}{\sqrt{2N}} \tag{4.23}$$

The uncertainty of the Reynolds-averaged shear stress is given Equation (4.24)

$$\varepsilon_{\overline{u'v'}} = \frac{\sqrt{1 + R^2_{\overline{u'v'}}}\sqrt{\overline{u'^2}}\sqrt{\overline{v'^2}}}{\sqrt{N}} \tag{4.24}$$

where the term $R_{\overline{u'v'}}$ is the correlation coefficient, defined as:

$$R_{\overline{u'v'}} = \frac{\overline{u'v'}}{\sqrt{\overline{u'^2}}\sqrt{\overline{v'^2}}} \tag{4.25}$$

The uncertainty in turbulent kinetic energy (TKE) is estimated through Equation (4.26) (Sciacchitano and Wieneke, 2016):

$$\varepsilon_{TKE} = \frac{\langle u' \rangle^2 + \langle v' \rangle^2}{\sqrt{2N}} \tag{4.26}$$

4.7.2 Uncertainty of PIV Measurement

This section discusses the uncertainties that are produced from the PIV measurement technique, such as uncertainties as a result of tracer particle slip, cross-correlation and spatial resolution.

Uncertainty as a result of particle slip

The accuracy of the measured properties from the PIV experiments depend on how well the seeding particle follow the flow and how accurately the displacement of these particles can be computed from the recorded images. *TiO2* particles are used during the PIV experiments. These particles have different density and velocity than that of the surrounding fluid. This

difference between fluid and particle velocity is called the particle slip velocity, u_{slip}. It is defined as a product of the particle response time, τ_p and the particle acceleration, a_p (Sun, 2014):

$$u_{slip} \approx \tau_p \cdot a_p = \varepsilon_{\tau_p} \tag{4.27}$$

The uncertainty related to particle slip velocity, (ε_{τ_p}) is determined by normalizing Equation (4.27) with the freestream velocity, U_∞. $TiO2$ particles have particle response time of $\tau_p = 2.56\ \mu s$ (Ragni et al., 2011). According to Melling (1997), for large density ratio ($\frac{\rho_p}{\rho_f} \gg 1$), the particle acceleration (equation of motion) can be simplified to:

$$\frac{du_p}{dt} = a_p = \frac{u_p - u_f}{\tau_p} \tag{4.28}$$

Where u_p and u_f are the instantaneous particle and fluid velocity. According to Ragni (2012), when steady flow is assumed, Equation (4.28) can be simplified to Equation (4.29).

$$a_p = \overrightarrow{U} \cdot \nabla \overrightarrow{U} \tag{4.29}$$

Inserting Equation (4.29) into Equation (4.27), the particle slip velocity is obtained as seen in Equation (4.30).

$$u_{slip} \approx \tau_p \cdot \left(\overrightarrow{U} \cdot \nabla \overrightarrow{U} \right) \tag{4.30}$$

It is noted that the particle slip velocity given in Equation (4.30) is only used as an estimate for regions without the presence of strong vortices, such as free stream. According to Sun (2014), for regions with presence of strong vortices, such as recirculation and reattachment region, the uncertainty due to the particle slip velocity is estimated through Equation (4.31)

$$\varepsilon_{\tau_p} = u_{slip} \approx \tau_p \cdot \left(\frac{\left| \vec{U}^2 \right|}{r} \right) \tag{4.31}$$

Where r is the vortex radius and is of the same magnitude as the step height (h) of the BFS. According to Sun (2014), the velocity magnitude $\overrightarrow{U}$ can be estimated through Equation (4.32).

$$\left| \overrightarrow{U} \right| = U_\infty - U_{conv} \tag{4.32}$$

Where U_∞ is the free stream velocity and U_{conv} is the convective shear layer velocity.

Uncertainty as a result of cross-correlation

The instantaneous velocity uncertainty produced as a result of image cross-correlation operation is estimated by Equation (4.33) (Humble, 2009).

$$\varepsilon_u = \frac{\varepsilon_{cc}}{\kappa \Delta t} \tag{4.33}$$

Where κ is image resolution in pix/mm, Δt is the pulse separation time of the laser and ε_{cc} is the uncertainty associated to the cross-correlation operation. According to Humble (2009), ε_{cc} is of the order of 0.1 $pixel$ for planar PIV and 0.2 $pixel$ for tomographic PIV.

Uncertainty as a result of spatial resolution

The uncertainty produced as a result of spatial resolution is estimated by the quantity $l^* = \left(\frac{WS}{\lambda}\right)$, also referred to as normalized window size. In this ratio WS is interrogation window size and λ is the spatial wavelength of the relevant flow structure. The ratio of the of of measured velocity and true velocity (u/u_0) with the normalized window size $\frac{WS}{\lambda}$ can be modelled through *sinc* function, as defined in Equation (4.34) (Schrijer and Scarano, 2008).

$$\varepsilon_{sr} = \frac{u}{u_0} = \text{sinc}\left(\frac{WS}{\lambda}\right) \tag{4.34}$$

According to de Kat and van Oudheusden (2012), the spatial wavelength (λ) can be determined by taking $l^* = 0.5$. As a result, the the spatial wavelength (λ) will be twice the final window size (WS) of 48×48 for the present PIV experiment.

4.7.3 Summary of Uncertainty Results

In this section the results of the uncertainties as defined and discussed in sections 4.7.1 and 4.7.2 are provided in Table 4.9. All uncertainty values in this table are normalized with freestream velocity of $U_\infty = 239\ ms^{-1}$ for subsonic case and $U_\infty = 534\ ms^{-1}$ for the supersonic case. Additionally, the normalized absolute values of the uncertainties are given as percentage. For both, subsonic and supersonic case, the uncertainties are calculated for $L/D = 1.8$ with exhaust plume at a point in the region where shear layer reattaches. For subsonic case the ensemble size was $N = 250$ images and for supersonic case $N = 476$ images. Now that all the uncertainties are computed, the total errors for each of the variables $\bar{u}$, $\langle u' \rangle$

	Subsonic		Supersonic	
Uncertainty parameter	**Value**	**Percentage**	**Value**	**Percentage**
Mean streamwise velocity $(\varepsilon_{\bar{u}})$	3.8 m/s	1.6 %	6.4 m/s	1.2 %
Mean radial velocity $(\varepsilon_{\bar{v}})$	2.7 m/s	1.1 %	2.9 m/s	0.5 %
Streamwise velocity fluctuation $(\varepsilon_{\langle u' \rangle})$	2.7 m/s	1.1 %	4.5 m/s	0.9 %
Radial velocity fluctuation $(\varepsilon_{\langle v' \rangle})$	1.9 m/s	0.8 %	2.0 m/s	0.4 %
Reynolds-averaged shear stress $(\varepsilon_{\overline{u'v'}})$	199.3 m^2/s^2	0.4 %	515.2 m^2/s^2	0.2 %
Turbulent kinetic energy (ε_{TKE})	244 m^2/s^2	0.4 %	760.2 m^2/s^2	0.3 %
Particle slip velocity (ε_{τ_p})	4.9 m/s	2.1 %	13.3 m/s	2.5 %
Cross-correlation (ε_u)	1.3 m/s	0.6 %	3.3 m/s	0.6 %
Spatial resolution effect (ε_{sr})	1.5 m/s	0.6 %	3.4 m/s	0.6 %

Table 4.9: Summary of normalized uncertainty results for subsonic and supersonic cases

and $\overline{u'v'}$ is estimated through standard error propagation relation given by:

$$\varepsilon_{total} = \sqrt{\varepsilon^2_{ensemble} + \varepsilon^2_u + \varepsilon^2_{\tau_p} + \varepsilon^2_{sr}} \tag{4.35}$$

For the subsonic case $\varepsilon_{total,\bar{u}} = 1.98\%$, $\varepsilon_{total,\langle u' \rangle} = 1.60\%$ and $\varepsilon_{total,\overline{u'v'}} = 1.23\%$. While for supersonic case $\varepsilon_{total,\bar{u}} = 2.9\%$, $\varepsilon_{total,\langle u' \rangle} = 2.8\%$ and $\varepsilon_{total,\overline{u'v'}} = 2.65\%$.

Chapter 5

Experimental Assessment

This chapter presents and discusses the results that were obtained from the Schlieren and the planar PIV experimental campaigns. Section 5.1 presents the Schlieren results, where the topological flow features and the issues related to wind tunnel start-up are briefly discussed. In section 5.2 the results of the planar PIV experiments are presented; this entails discussion of instantaneous and mean flow results. The analysis of mean flow results include discussion of inflow conditions, velocity distribution, turbulent kinetic energy (TKE), pressure field and reverse flow probability (RFP).

5.1 Schlieren Results

For the present thesis investigation, Schlieren visualization is used to qualitatively identify the effect of varying nozzle length and the presence of an exhaust plume on the topological flow features in the wake of an axisymmetric BFS at subsonic and supersonic flows. Additionally, Schlieren experiments are used to select subsonic and supersonic test conditions (M_∞, p_0) at which the wind tunnel starts properly. In section 5.1.1 the topological flow features of an axisymmetric BFS at subsonic and supersonic flows are discussed. Section 5.1.2 discusses the wind tunnel start-up investigation.

5.1.1 Topological Flow Features

Supersonic Case

Figure 5.1 show Schlieren results for $M_\infty = 2.20$ for $L/D = 0.6, 0.9, 1.2, 1.8$, with and without exhaust plume, respectively. In all cases shown, the incoming flow is from left to right. As discussed in section 4.4, a vertical knife edge, which allows to obtain horizontal density

gradient, was used during the Schlieren campaign in order to better visualize the shock waves (SW) system. A downside of using vertical knife edge is that the boundary layer (BL) at the top of the main body is not clearly visible.

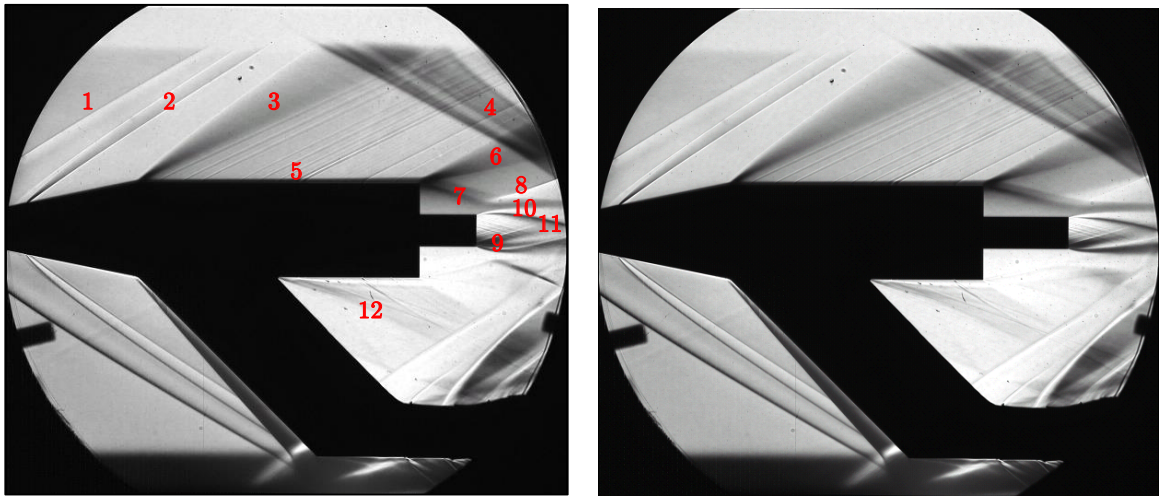

(a) $L/D = 0.6$ (b) $L/D = 0.9$

(c) $L/D = 1.2$ (d) $L/D = 1.8$

Figure 5.1: Schlieren mean flow field results for $M_\infty = 2.20$, $p_0 = 2.5$ bar and $p_{0,jet} = 27$ bar

As shown in Figure 5.1(a), a number of distinct features can be observed from the Schlieren mean flow field images. The shock waves (SW) (indicated by 1 and 2), which originate from the nose and the tripping wire of the model are reflected off the upper and lower tunnel walls (indicated by 4). At the location where the model geometry changes from canonical forebody to cylindrical main body, the first Prandtle-Mayer Expansion (PME) fan (indicated by 3) can be observed. A turbulent boundary layer (BL) (indicated by 5) that develop due

to the tripping wire, can be seen flowing over the upper part of the model. The second PME (indicated by 6) develop at the edge of the BFS due to an abrupt increase in flow area as a result of abrupt change in geometry. Furthermore, at the edge of the BFS the shear layer separates (indicated by 7). The second PME fan causes the separated shear layer to deflect downwards and impinge on the exhaust plume. Upon impingement, the deflected shear layer changes the direction again due to the expanding jet resulting in development of a plume shock (indicated by 8). An expansion fan (indicated by 9) at the nozzle lip can be seen for the nozzle operating at $M_{e,jet} = 3.5$. Furthermore, between the expansion fan (9) at the nozzle lip and the jet boundary (indicated by 10), a barrel shock (indicated by 11) develop. The configurations without exhaust plume, which are provided in Appendix C (Figure C.2), have similar shock/expansion wave system as the configuration with exhaust plume except in the region near the nozzle exit. The shock/expansion wave system for $L/D = 0.9$, $L/D = 1.2$ and $L/D = 1.8$ configuration with exhaust plume are shown in Figures 5.1(b), 5.1(c) and 5.1(d), respectively. For $L/D = 1.2$ and $L/D = 1.8$ configurations the separated shear layer impinges on the nozzle, resulting in a recompression shock more upstream of the exhaust plume compared to $L/D = 0.6$, where the recompression shock (plume shock) occur right above the exhaust plume. As can be seen in Figure 5.1, the exhaust plume for all nozzle configurations is under-expanded. However, as can be seen, the under-expansion of the exhaust plume for $L/D = 1.8$ configuration is less compared to $L/D = 0.6$. This can be attributed to presence of higher pressure region in the plume region caused by the development of recompression shock more upstream of the exhaust plume. It should be noted that the precise shape of the exhaust plume (over-expanded or under-expanded) is not defined by the ratio of the static jet pressure and the pressure in the freestream, but by the ratio of the static jet pressure and local static pressure at the location of the exhaust plume. The difference between both ratios depends on the geometry of the model, in particular the nozzle length.

The support sting mounted at the lower part of the cylindrical main body disturbs the flow behind it. In Figure 5.1(a) this region is indicated by (12). As the flow reaches the trailing edge of the support sting, an abrupt increase in flow area results in development of a PME fan. A numerical study on base flow of a blunted cone-cylinder rocket model in the presence of supersonic exhaust jet at $M_\infty = 2.98$, has been conducted by Dharavath et al. (2010). From this study it has been observed that due to the presence of support sting, the recirculation patterns in the upper and lower portions in the base region are different, as seen in Figure 5.2. In addition, it is found that the lower portion of the base experiences lesser base pressure compared to the upper portion due to the presence of a support sting. Also, it has been shown that the radial variation of base pressure in the lower portion is less compared to the radial variation of base pressure in the upper portion (see Figure 5.3). The maximum difference in base pressure between the lower portion and the upper portion was about 50% (Dharavath et al., 2010). Ottens et al. (2001) also conducted a numerical study of support influence on base flow of the FESTIP model in supersonic flow. This study concluded that the expansion fan emanating from the trailing edge of the support sting causes a decrease of the base pressure and that the flow around the FESTIP model with a support sting cannot be treated as axisymmetric. Moreover, a PIV investigation conducted by Oudheusden and Scarano (2008b), also on the FESTIP model in supersonic flow showed that at the lower part of the model a significantly higher turbulence level is observed, which can be attributed to the presence of support sting.

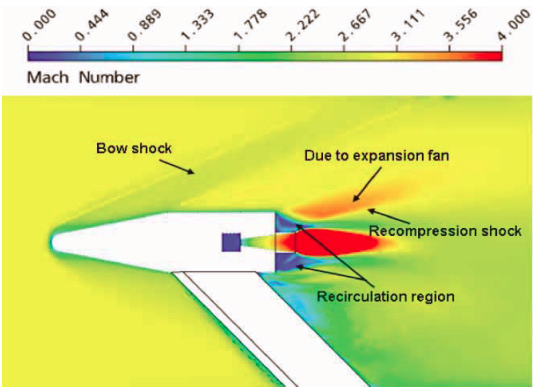

Figure 5.2: Mach number contour for $M_\infty = 2.98$. Adapted from Dharavath et al. (2010)

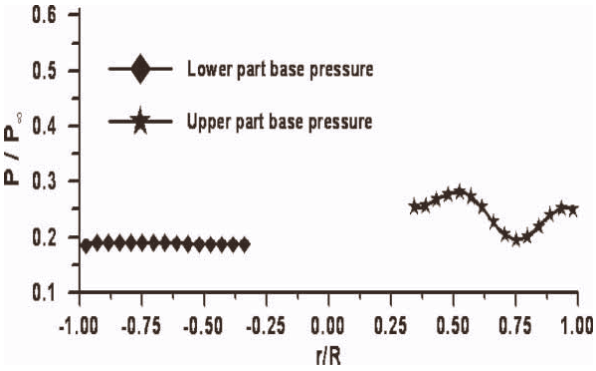

Figure 5.3: Radial variation of the base in lower and upper portions of the base. Adapted from Dharavath et al. (2010)

Subsonic Case

Figure 5.4 show the Schlieren results for $M_\infty = 0.76$ for $L/D = 0.6, 0.9, 1.2, 1.8$, with and without exhaust plume, respectively. By comparing the subsonic case with the supersonic case as shown in Figure 5.1, it can be observed that the boundary layer in subsonic case is thinner. Also, due to the absence of the expansion fan at edge of the BFS, the deflection of the separated shear layer towards the nozzle or plume is not as sharp as it was in the supersonic case, which results in larger recirculation region compared to supersonic case.

As can be observed from Figure 5.4, the exhaust plume of the subsonic cases is over-expanded. This over-expansion can be attributed to the lower static jet pressure at the nozzle exit ($p_{e,jet}$) compared to the free stream pressure (p_∞). As provided in Table 4.6, the static jet pressure at the nozzle exit is $p_{e,jet} = 0.28$ bar for $M_\infty = 0.76$, which significantly lower than the free stream pressure of $p_\infty = 1.38$ bar. According to Sutton and Bibarz (2001), if the free stream pressure placed on the supersonic nozzle is sufficiently larger than the static jet pressure at the nozzle exit, shock-induced flow separation will occur inside the divergent portion of the nozzle, as shown in Figure 5.5. Furthermore, Summerfield et al. (1954) reports that the flow separation inside the nozzle occurs as soon as the ratio of nozzle exit pressure to ambient pressure ($p_{e,jet}/p_\infty$) drops below 0.35-0.45. For the present case, with $p_{e,jet} = 0.28$ bar and $p_\infty = 1.38$ bar, the pressure ratio is $p_{e,jet}/p_\infty = 0.20$. This pressure ratio is below the Summerfield separation criterion of 0.35-0.45 and therefore on basis of this it can be concluded that the flow sepatation indeed occur inside of the nozzle. Also, Zandbergen (2016) reports that in case of an over-expanded exhaust plume, where (oblique) shock waves exist at the nozzle exit, this shock waves may propagate upstream and cause flow separation inside of the nozzle. By visual inspection of the mean Schlieren images as shown in Figure 5.4, it can be seen that the oblique shock waves for all nozzle configurations appears to emanate slightly upstream of the nozzle exit, especially for $L/D = 0.9$ (Figure 5.4(b)) where the oblique shocks seems to occur further upstream of the nozzle exit. Therefore, this also suggest flow separation in the nozzle. Although there seems to be flow separation in the nozzle, it is however difficult to see whether there is more of less flow separation for one or other nozzle configurations.

Earlier investigations on supersonic rocket nozzles (e.g. Lawrence (1967), Verma (2002)) have shown that the development of shock wave/boundary layer interaction in an over-expanded nozzle display strong unsteadiness which can result in symmetrical or asymmterical flow separation. The shock-induced flow separation in rocket nozzles is considered undesirable because an asymmetry in the ow can induce dangerous lateral forces, the so-called side-loads, which may damage the nozzle (Frey and Hagemann, 2000). From the mean Schlieren images, as shown in Figure 5.4, the flow separation in the nozzle appears to be axisymmetric, which according to Sutton and Bibarz (2001) can be attributed to steady flow in the nozzle. By further inspection of the instantaneous Schlieren images, a slight back and forth movement of the separation shock is observed. Furthermore, it can be observed that the diameter of the supersonic exhaust plume is smaller than the exit diameter of the nozzle. At the exit of the nozzle the flow in the inner core is supersonic, but is enclosed by an annular shaped region of subsonic flow. An overview of the results without exhaust plume are provided in Appendix C (Figure C.1).

5.1.2 Wind Tunnel Start-Up

At the beginning of the Schlieren campaign several experiments were conducted to investigate proper start-up of the wind tunnel for the selected flow condition (M_∞ and p_0). Additionally, for the supersonic case these experiments were used to select M_∞ and p_0 so that the reflected shock waves from the upper and lower tunnel walls did not interfere with topological flow features occurring in the exhaust plume region.

Table 5.1 provides a test matrix for this investigation. Only one nozzle configuration ($L/D = 1.2$) without exhaust plume was tested for a range of M_∞ and p_0, as shown in Table 5.1. For the subsonic case, it is found that the wind tunnel starts properly when freestream Mach number of $M_\infty = 0.70$ and total pressure of $p_0 = 2.0$ bar are selected. Figure 5.6 show instantaneous Schlieren snapshot for $M_\infty = 2.0$ for two different total pressures, namely $p_0 = 1.5$ bar and $p_0 = 2.5$ bar. Figure 5.6(a) show the case in which the tunnel is set to nominal Mach number of $M_{nom} = 2.0$ and total pressure of $p_0 = 1.5$ bar. Clearly, in this case due to the low total pressure the tunnel does not start properly, resulting in a flow field without presence of shock/expansion waves. Figure 5.6(b) show the instantaneous Schlieren snapshot for $M_\infty = 2.0$ but with a total pressure of $p_0 = 2.5$ bar. As can be observed, in this case the tunnel starts properly, resulting in a typical flow field with shock/expansion waves. As can be seen in Figure 5.6(b), the shock waves reflecting from the tunnel walls are now directed towards the region where the supersonic jet exhausts. In order to avoid that these reflected shock waves interfere with the exhaust plume, the freestream Mach number is increased to 2.2. The results of this increased Mach number is shown in Figure 5.7, where the reflected shock waves are now further away from the exhaust plume compared to $M_\infty = 2.0$ case . As a result of this investigation, all the Schlieren experiments and the planar PIV experiments were conducted with $M_\infty = 0.70$ and $p_0 = 2.0$ bar for the subsonic cases and with $M_\infty = 2.20$ and $p_0 = 2.5$ for the supersonic cases.

p_0 [bar]	Config. (L/D)	$p_{0,jet}$ [bar]	M_∞ [-]
1.5	1.2	Off	2.0
2.0			0.7, 1.5, 1.6, 1.7, 1.8, 1.9, 2.0, 2.1, 2.5
2.3			2.2
2.5			2.0, 2.1, 2.2, 2.3
3.0			2.5
3.5			2.5

Table 5.1: Schlieren experimental test matrix for wind tunnel start-up investigation

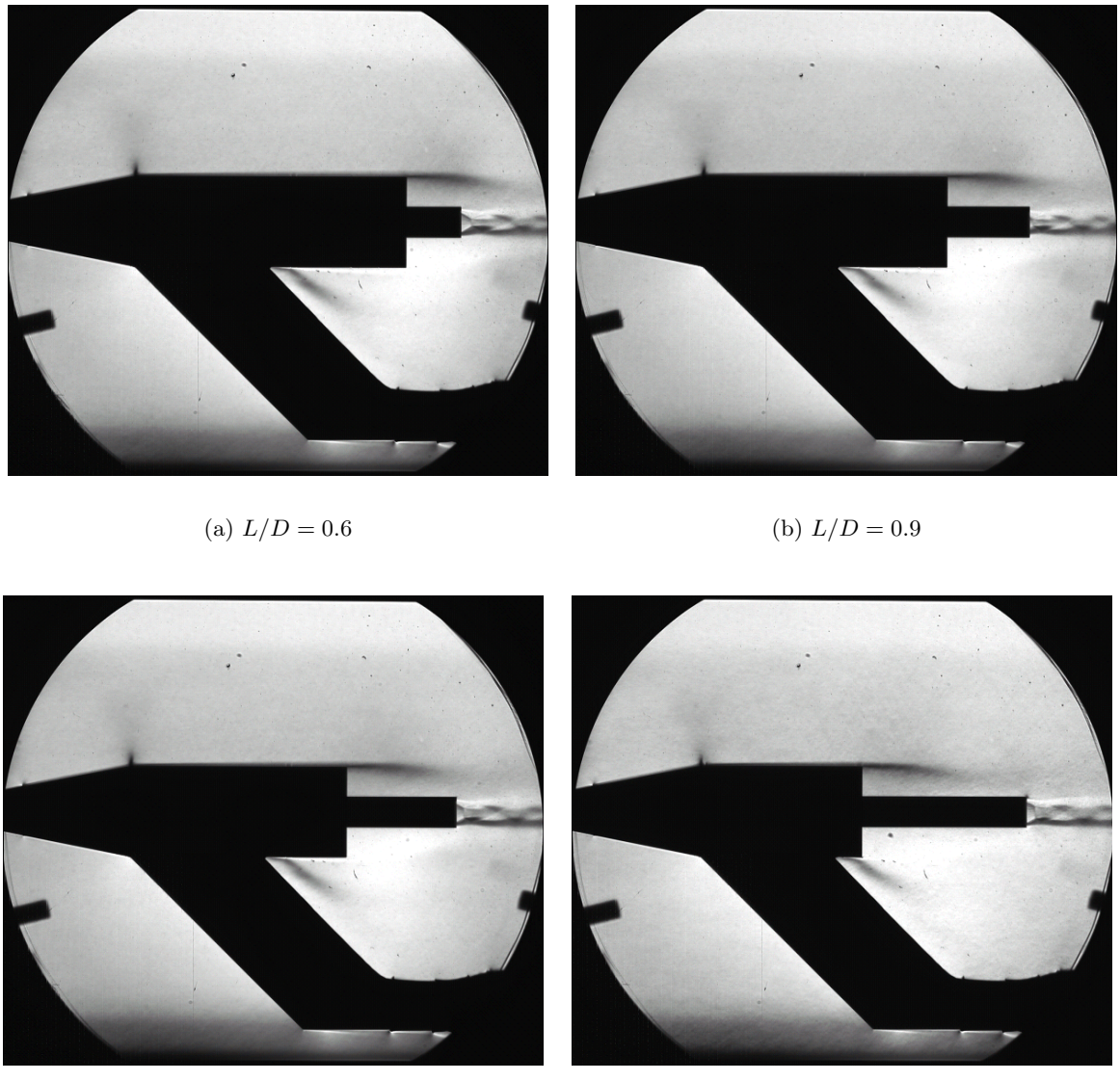

(a) $L/D = 0.6$ (b) $L/D = 0.9$

(c) $L/D = 1.2$ (d) $L/D = 1.8$

Figure 5.4: Schlieren mean flow field results for $M_\infty = 0.76$, $p_0 = 2.0$ bar and $p_{0,jet} = 22$ bar

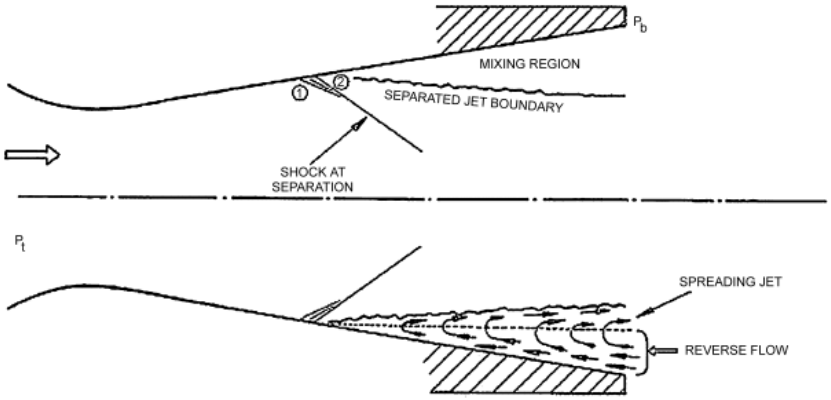

Figure 5.5: Flow separation inside a nozzle (Herbert and Herd, 1964)

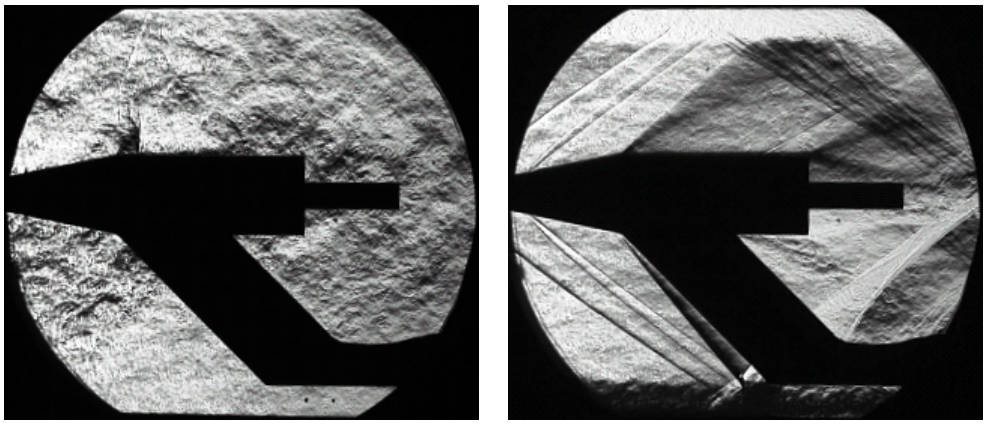

(a) $M_{nom} = 2.0$, $p_0 = 1.5$ bar (b) $M_\infty = 2.0$, $p_0 = 2.5$ bar

Figure 5.6: Instantaneous Schlieren snapshots for $L/D = 1.2$, without exhaust plume

Figure 5.7: Instantaneous Schlieren snapshots for $L/D = 1.2$ at $M_\infty = 2.2$, $p_0 = 2.5$ bar, without exhaust plume

5.2 PIV Results

5.2.1 Instantaneous Flow Organization

The wake region of an axisymmtric BFS is linked to a large-scale periodic fluctuations induced by the instability of the shear layer. The mean velocity field results, which will be discussed in the coming sections, does not provide sufficient approximation of the instantaneous conditions in the wake region. Therefore, present section provides instantaneous velocity distributions in order to show the presence of the turbulent structures in the wake of an axisymmetric BFS. Figures 5.8 and 5.9 presents two separate, non-correlated snapshots of the streamwise

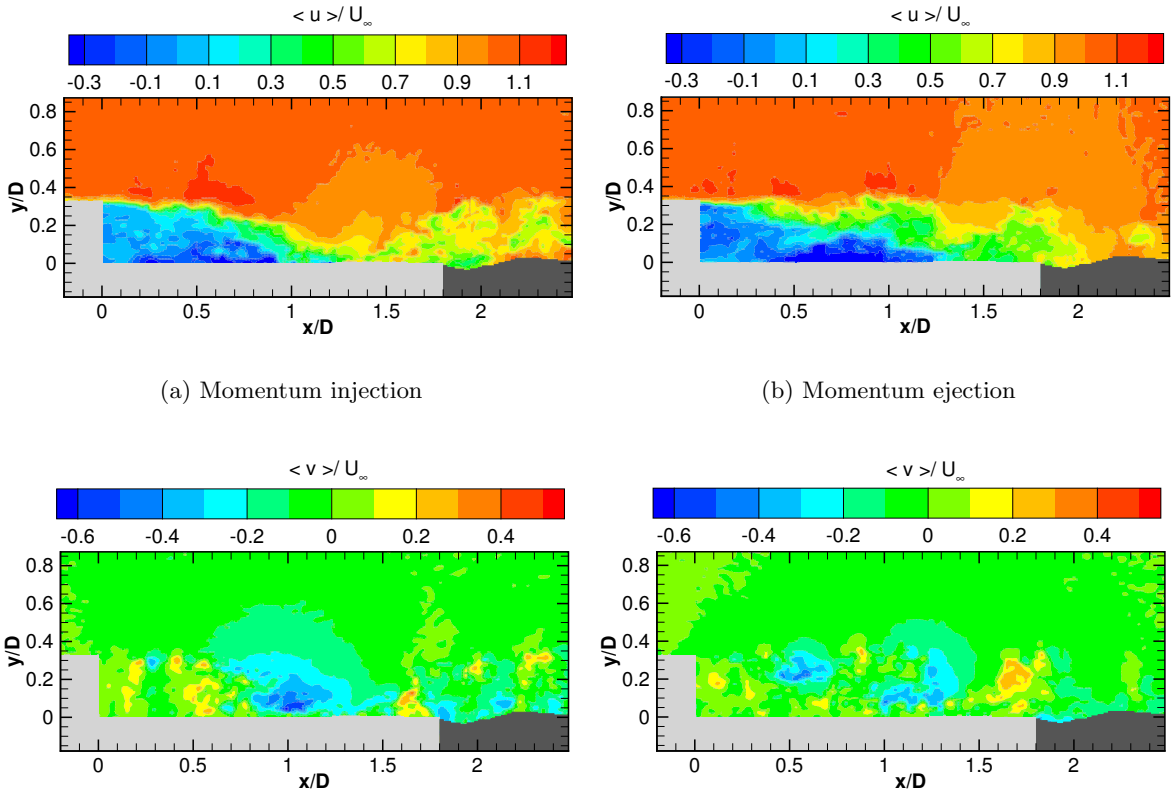

(a) Momentum injection

(b) Momentum ejection

(c) Momentum injection

(d) Momentum ejection

Figure 5.8: Instantaneous velocity distribution snapshots of $L/D = 1.8$ at $M_\infty = 0.76$, with plume

(u) and radial (v) instantaneous velocity distributions, at different time instances for $L/D = 1.8$ and $L/D = 0.6$ at $M_\infty = 0.76$ with exhaust plume, respectively. These instantaneous velocity distribution, which are more chaotic than the mean velocity distribution, illustrate the deviation of the unsteady shear layer from its mean. As shown in Figure 5.8(b), a significant increase of the recirculation region can be observed for $L/D = 1.8$ compared to the first streamwise instantaneous velocity distribution snapshot (Figure 5.8(a)). For

$L/D = 0.6$, however, this increase in recirculation region is not clearly visable. From all the 500 instantaneous snapshots of the flow field that was obtained from DaVis for $L/D = 1.8$, it is observed that the recirculation region grows and shrinks in a quasi-cyclic manner as a result of fluctuating reattachment point of the shear layer. As discussed in section 2.2.3, this periodic increase and decrease of the recirculation region can be linked to the momentum injection and ejection, which is identified by Schrijer et al. (2014) as the second unsteady mode (see Figure 2.7).

Figures 5.8(c), 5.8(d), 5.9(c) and 5.9(d) show the radial (v) instantaneous velocity distributions for $L/D = 1.8$ and $L/D = 0.6$, respectively. The radial (v) instantaneous velocity distributions seems to be more choatic than the streamwise (u) distribution. From both, the radial and streamwise instantaneous velocity distributions, large-scale vortical structures can be observed in the base region and further downstream, for both the momentum injection and ejection cases. As can be seen from Figure 5.8(b), during the momentum ejection, the reattachment length gets longer and the recirculation region burst sending the momentum downstream. As shown in Table 5.2, an increase in reattachment length result in decrease of maximum backflow velocity. 5.9.

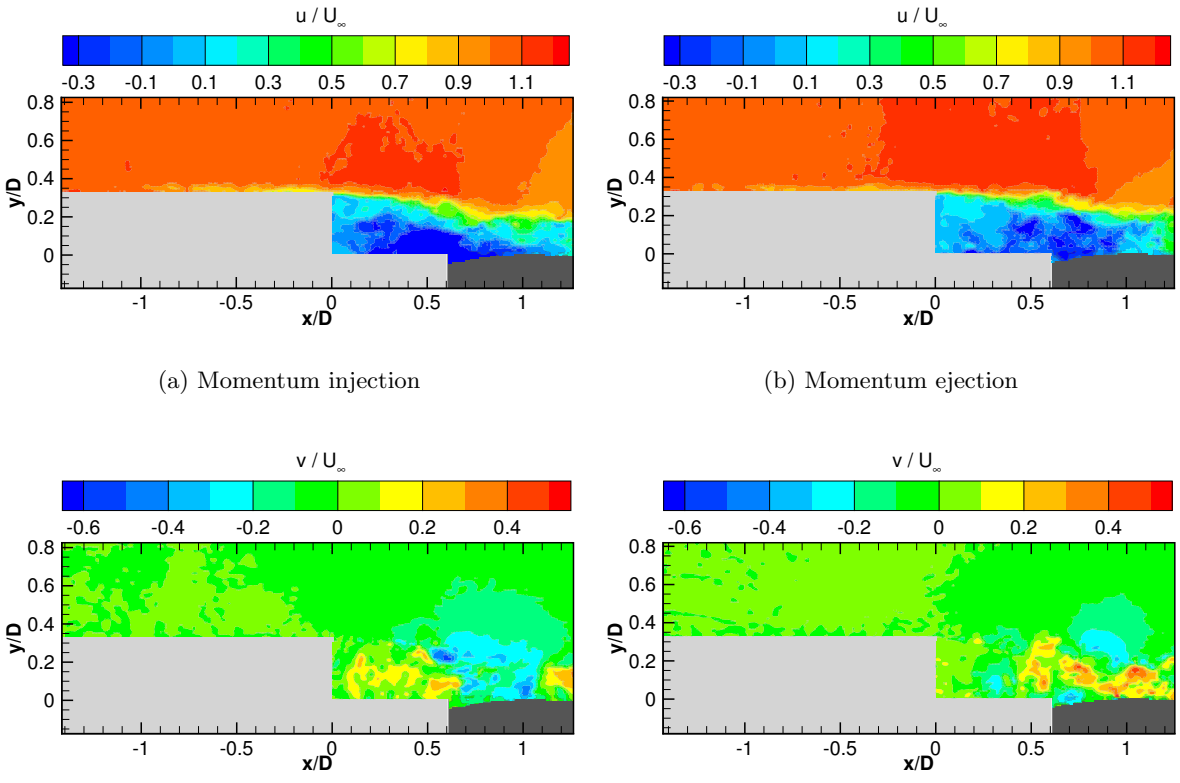

(a) Momentum injection

(b) Momentum ejection

(c) Momentum injection

(d) Momentum ejection

Figure 5.9: Instantaneous velocity distribution snapshots of $L/D = 0.6$ at $M_\infty = 0.76$, with plume

5.2.2 Mean Flow Results

Inflow Conditions

The inflow conditions have been investigated to verify the state of the boundary layer and the freestream velocity (U_∞) upstream of the edge of BFS. This is done by plotting the mean streamwise velocity profile at $x = -0.1D$ for $M_\infty = 0.76$ and $M_\infty = 2.20$ for $L/D = 0.6, 0.9, 1.2, 1.8$, with and without exhaust plume, as shown in Figure 5.10.

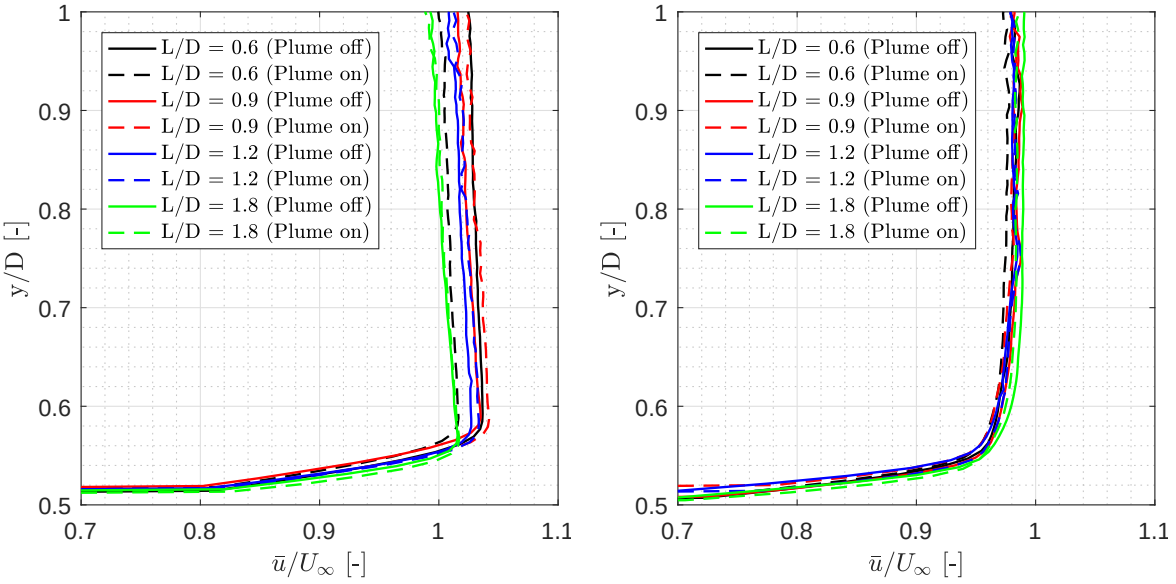

(a) Subsonic case ($M_\infty = 0.76$)

(b) Supersonic case ($M_\infty = 2.20$)

Figure 5.10: Mean streamwise velocity profiles at x = -0.1D (upstream of separation point)

It is noted that the used PIV setup was not able to capture the velocity exactly at the model surface due to the limitations in spatial resolution and practical difficulties to view close to the wall surface. As such, the velocities were measured slightly above the surface of the model. As result, only the outer part of the boundary layer over the cylindrical main body was measured. With the obtained velocity profiles, the boundary layer thickness at $x = -0.1D$ is estimated by taking a point in velocity profile where the velocity has reached 99% of the freestream velocity. For the subsonic cases this boundary layer thickness was approximately $\delta_{99\%}/D \approx 0.06$ or $\delta_{99\%} \approx 3\ mm$ and $\delta_{99\%}/D \approx 0.11$ or $\delta_{99\%} \approx 5.5\ mm$ for the supersonic cases. Since the conical forebody of the model is equipped with a tripping wire, it can be assumed that the boundary layer over the upper surface of the cylindrical main body is turbulent. Furthermore, by comparing the typical velocity profile of laminar and turbulent boundary layers, as shown in Figure 5.11, with the mean streamwise velocity profile as shown in Figure 5.10, it can be concluded that the velocity profile of boundary layer for both subsonic and supersonic cases are indeed turbulent.

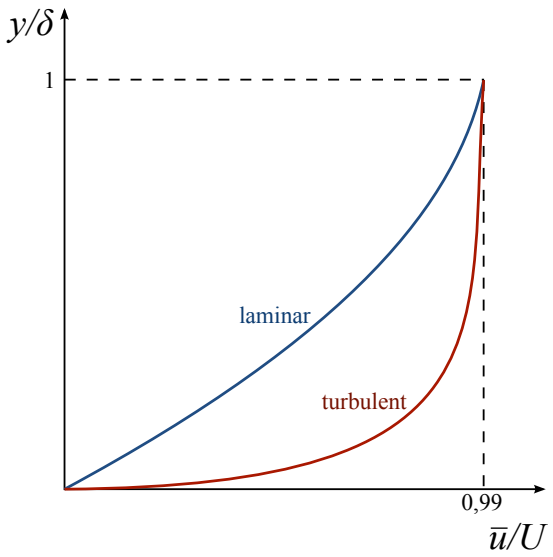

Figure 5.11: A comparison of a typical laminar and turbulent boundary layer velocity profiles

In Figure 5.10, the mean streamwise velocity, $\bar{u}$ is nondimensionalized with the freestream velocity, U_∞ which is computed using isentropic relations and the measured local static pressure (p_∞), total temperature (T_0) and pressure (p_0) in the settling chamber. As can be seen in Figure 5.10, small variation in inflow velocity can be observed between different cases. A variation of no more than $0.01U_\infty$ can be seen in inflow velocity between the cases with and without exhaust plume, except for $L/D = 0.6$ at $M_\infty = 0.76$. With different nozzle lengths this variation is no more than $0.02U_\infty$.

Mean Velocity Distribution

Figures 5.12 and 5.13 display the mean streamwise velocity contours, $\bar{u}$ for $M_\infty = 0.76$ and $M_\infty = 2.20$, respectively. In both figures, the cases without and with the presence of exhaust plume are shown at left and right side, respectively. The four different nozzle lengths increases from top to bottom from $L/D = 0.6$ to 0.9, 1.2 and 1.8. As shown in both figures, the origin for all nozzle configuration is located at the edge of the cylindrical main body ($x/D = 0$) and at the center line of afterbody ($y/D = 0$). The streamwise velocity, $\bar{u}$ is nondimensionalized with the freestream velocity of $U_\infty = 239\ ms^{-1}$ for subsonic case and with $U_\infty = 534\ ms^{-1}$ for supersonic case. For the sake of comparison, the figures have one common color bar for all the cases shown. These colors specify the magnitude of the mean streamwise velocity, $\bar{u}$. The black arrows and contour lines, in both figures indicate the vectors and the zero streamwise velocity, respectively. The location of the model and the shape of the exhaust plume are indicated with light and dark grey colors, respectively. Due to insufficient seeding particles in the plume region, no velocity data could be acquired in at least 20% of the instantaneous velocity fields, resulting in a region with outliers. As such, during post-processing the plume region has been masked with DaVis in order to avoid the region with outliers, which can be problematic for the subsequent analysis of mean pressure fields. Figure 5.14 show average Reynolds stress ($< Re_{xy} >$) vector field of the plume region obtained with one of the 4

cameras. It is used to estimate the shape of the plume for masking. The reason for using average Reynolds stress vector field is that it is easier to see where approximately the plume region is compared to mean velocity vector fields. As shown in Figure 5.14 (right), the plume region with outliers is masked by applying a geometric mask. It should be noted that the masked plume region is an approximation, it possible that the actual plume region is slightly above or below the masked region.

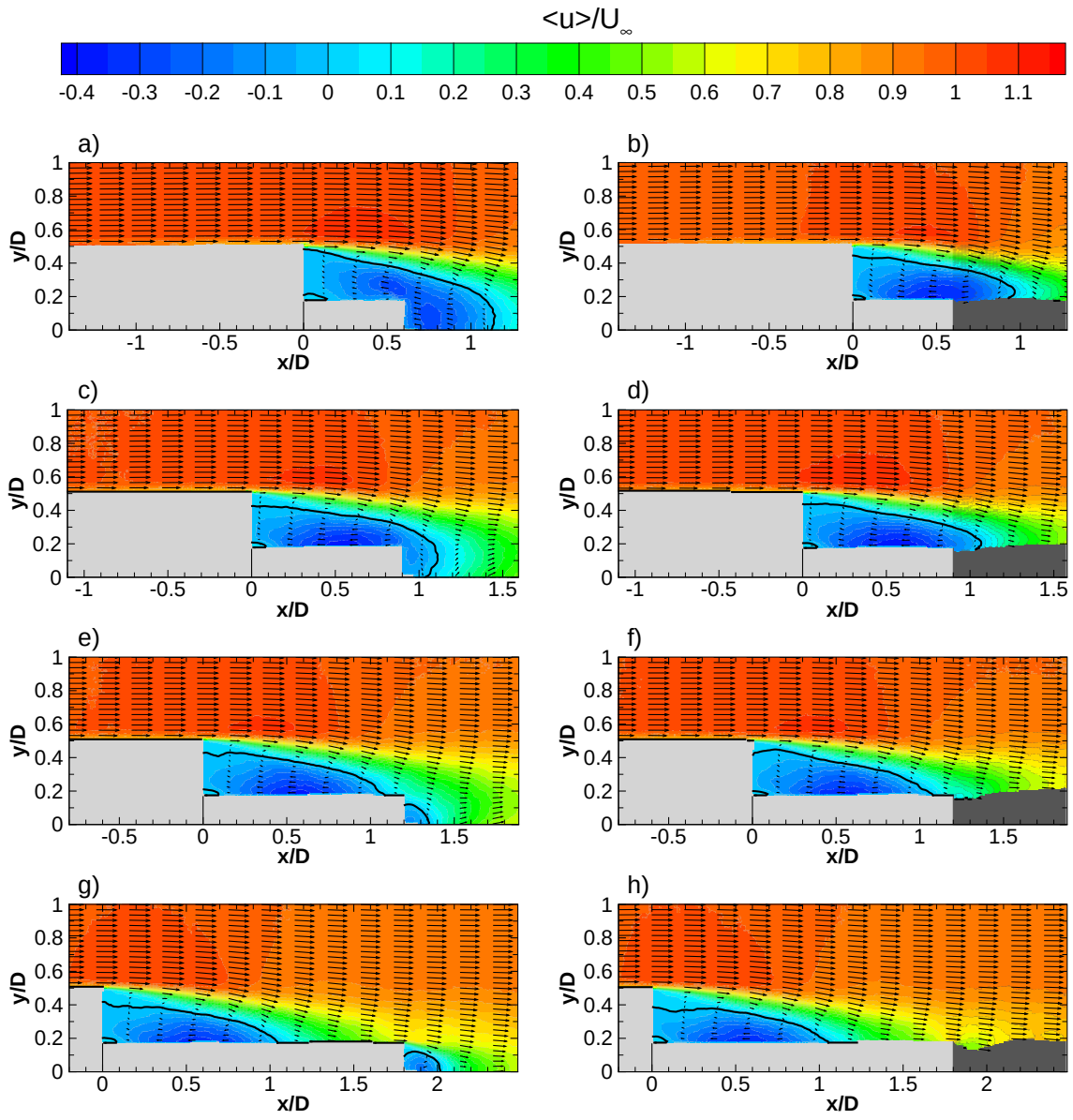

Figure 5.12: Mean streamwise velocity for $M_\infty = 0.76$ case for increasing nozzle length (top to bottom); without plume (left) and with plume (right); Solid black line indicates zero streamwise velocity

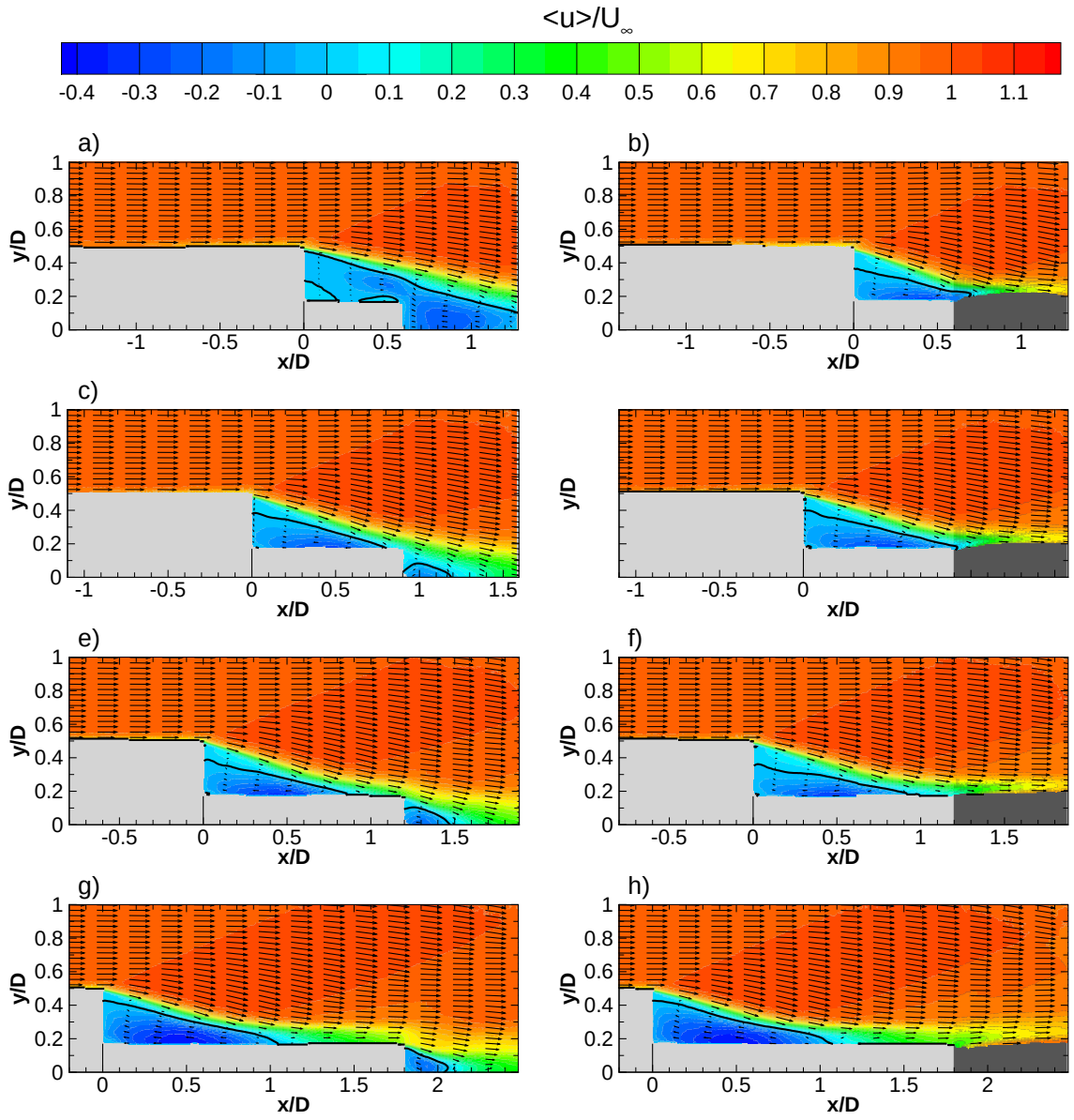

Figure 5.13: Mean streamwise velocity for $M_\infty = 2.20$ case for increasing nozzle length (top to bottom); without plume (left) and with plume (right); Solid black line indicates zero streamwise velocity

Table 5.2 show the result of the mean shear layer reattachment length (L_R) and the absolute value of the maximum mean back flow velocity ($|\bar{u}_{\min}|$) for $M_\infty = 0.76$ and $M_\infty = 2.20$ for four different nozzle configurations, respectively. The mean shear layer reattachment length is determined from Figures 5.12 and 5.13 by taking the streamwise location where the zero streamwise velocity, as indicated by black contour line, meet the solid afterbody (nozzle) or the exhaust plume. The mean shear layer reattachment length is nondimensionalized with the diameter ($D = 50\ mm$) of the cylindrical main body.

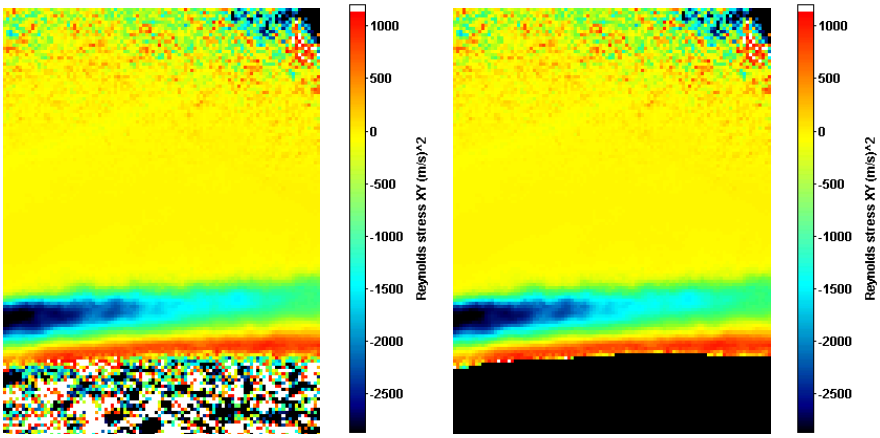

Figure 5.14: Average Reynolds stress ($< Re_{xy} >$) without masked exhaust plume (left) and with masked exhaust plume (right)

	$M_\infty = 0.76$ (no plume)		$M_\infty = 0.76$ (plume)		$M_\infty = 2.2$ (no plume)		$M_\infty = 2.2$ (plume)	
	L_R/D	$\lvert\bar{u}_{\min}\rvert/U_\infty$	L_R/D	$\lvert\bar{u}_{\min}\rvert/U_\infty$	L_R/D	$\lvert\bar{u}_{\min}\rvert/U_\infty$	L_R/D	$\lvert\bar{u}_{\min}\rvert/U_\infty$
$L/D = 0.6$	n.a	n.a	0.9	0.40	n.a	n.a	0.6	0.28
$L/D = 0.9$	n.a	n.a	1.0	0.42	0.8	0.27	0.9	0.28
$L/D = 1.2$	1.1	0.39	1.1	0.38	0.9	0.31	1.0	0.29
$L/D = 1.8$	1.1	0.36	1.1	0.37	1.1	0.39	1.1	0.39

Table 5.2: Mean reattachment length (L_R) and absolute value of maximum mean back flow velocity in the recirculation region over the nozzle ($|\bar{u}_{\min}|$)

As shown in Figures 5.12 and 5.13, the step at $x/D = 0$ causes the incoming subsonic and supersonic flow to separate and deflect towards the afterbody. As a result, a recirculation region with significant back flow is formed, as shown in Table 5.2. As can be observed from both figures, the outer external flow and recirculation region in the wake of BFS is divided by a shear layer. Depending on the nozzle length (L/D), the shear layer impinges on the nozzle (solid reattachment), on the flow further downstream (fluidic reattachment) or on the nozzle and the flow downstream (hybrid reattachment). These three reattachment cases were also discussed in section 2.2.2 and schematically illustrated in Figure 2.4. Furthermore, for the cases without exhaust plume, a secondary recirculation downstream of the nozzle can be observed. The formation of this secondary recirculation downstream of the nozzle is also observed by Weiss and Deck (2011), as shown in Figure 5.15. As the nozzle exit remained open during the tests without exhaust plume, the recirculation region downstream of the nozzle is likely to extent inside the nozzle. Moreover, due to the separation of the back flow over the nozzle, a secondary recirculation region for the majority of the cases can be observed at the corner of the base ($x/D = 0$), especially for the subsonic case. The observation of the secondary recirculation region was possible thanks to the high spatial resolution of the PIV system.

As can be observed from Figure 5.12 and Table 5.2, for $M_\infty = 0.76$ an increase in nozzle length does not result in significant change in shear layer reattachment length, but it does decreases the maximum backflow velocity. For $L/D = 0.6$ and $L/D = 0.9$, the shear layer

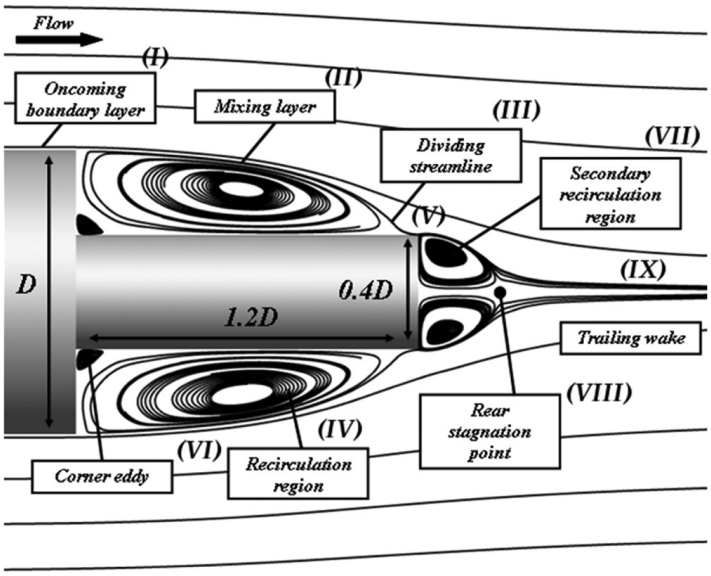

Figure 5.15: Axisymmetric BFS with $L/D = 1.2$ without presence of an exhaust plume (Weiss and Deck, 2011)

does not impinge on the nozzle. For the cases with exhaust plume, the shear layer impinges on the plume. The cases without exhaust plume leads to a merger of the recirculation regions downstream of the base and downstream of the nozzle. For $L/D = 1.2$ and $L/D = 1.8$, with and without exhaust plume, the mean shear layer reattachment occur on the nozzle at $L_R/D = 1.1$. This mean reattachment point is in accordance with the numerical studies of Deck and Thorigny (2007) and Weiss et al. (2009), where a mean reattachment point of $L_R/D \approx 1.1$ was found for an axisymmtric BFS with $L/D = 1.2$ at $M_\infty = 0.70$, with and without exhaust plume. Furthermore, in their paper, Deprés et al. (2004) indicate a reattachment length of $L_R/D \approx 1.3$ for an axisymmetric rearward facing step ($L/D \gg 1$) at $M_\infty = 0.80$ and a reattachment length of $L_R/D \approx 1.2$ for $L/D = 1.2$ at $M_\infty = 0.70$. As can be seen in Figure 5.12, $L/D = 1.2$ and $L/D = 1.8$ cases look remarkably similar up to the reattachment point, however downstream of this point, the flow looks clearly different. For $L/D = 1.8$, it can be seen that after the reattachment of the shear layer the flow has the chance recover. As a result, a higher streamwise velocity can be observed over the nozzle and further downstream. Moreover, without exhaust plume, the longest nozzle length ($L/D = 1.8$) display a more pronounced recirculation region downstream of the nozzle.

As shown in Figure 5.13, due to the expansion fan at the edge ($x/D = 0$), a sharp deflection of the shear layer towards the nozzle can be observed for $M_\infty = 2.20$ compared to $M_\infty = 0.76$ case. As a result of this sharp deflection, the recircultation region is smaller compared to $M_\infty = 0.76$ case. For the cases without exhaust plume, the reattachment occurs on the nozzle, except for $L/D = 0.6$ (Figure 5.13 (a)), which per definition does not have a reattachment location. This case also displays a small separation zone on the nozzle at $x/D \approx 0.5$, which is induced by separation of backflow over the trailing edge of the nozzle. For $L/D = 0.6$ and $L/D = 0.9$ with presence of exhaust plume, the mean reattachment occur on the plume while for $L/D = 1.2$ and $L/D = 1.8$ the reattachment occurs on the nozzle, regardless of the presence of plume. Furthermore, as can be observed from Figure 5.13 (d) and (f), the presence

Author	Technique	M_∞	L/D	L_R/D
Current	Experimental	0.76	0.6	n.a (without plume)/0.9 (with plume)
-	-	-	0.9	n.a (without plume)/1.1 (with plume)
-	-	-	1.2	1.1 (without plume)/1.1 (with plume)
-	-	-	1.8	1.1 (without plume)/1.1 (with plume)
Deprés et al. (2004)	Experimental	0.70	1.2	1.2 (without plume)
-	-	0.80	$\gg 1.0$	$\approx$1.3 (without plume)
Gentile et al. (2016)	Experimental	20 m/s	2.0	1.2
Deck and Thorigny (2007)	ZDES (numerical)	0.70	1.2	$\approx$1.1
Weiss et al. (2009)	ZDES (numerical)	0.70	1.2	$\approx$1.1
Le (2005)	-	0.70	1.22	1.1
Herrin and Dutton (1994)	Experimental	2.46	>2.5	1.335
Loth et al. (1992)	Large eddy (numerical)	2.09	$h/R = 0.28$	$L_R/h = 3.2$

Table 5.3: Normalized reattachment lengths (L_R/D) for axisymmetric BFS

of exhaust plume appears to make the reattachment length slightly longer for $L/D = 0.9$ and $L/D = 1.2$. As shown in Table 5.2, the reattachment length for $L/D = 1.8$ at $M_\infty = 2.20$ and $M_\infty = 0.76$ are similar, while a slight increase in backflow can be observed for $M_\infty = 2.20$. For $L/D = 0.9$ and $L/D = 1.2$, the reattachment occur further upstream of the nozzle compared to $M_\infty = 0.76$ case.

Table 5.3 provide an overview of the reattachment length found for the current cases and in the literature. A good agreement with Deprés et al. (2004), Deck and Thorigny (2007), Weiss et al. (2009) and Le (2005) is found for the subsonic axisymmetric case with $L/D = 1.2$. Also $L/D = 1.8$ case show good agreement with Deprés et al. (2004) and Gentile et al. (2016), with a slight difference in the reattachment length of 0.1-0.2. The reattachment length (L_R/D) for the supersonic axisymmetric case shows a difference of approximately 0.25 with respect to the values reported by Herrin and Dutton (1994).

Turbulent Kinetic Energy

Turbulent kinetic energy (TKE) is a measure of intensity of turbulence, which can be determined according to:

$$TKE = \frac{\left\langle (u')^2 \right\rangle + \left\langle (v')^2 \right\rangle}{2} \tag{5.1}$$

where $\langle u' \rangle$ and $\langle v' \rangle$ are the RMS of the streamwise and radial velocity fluctuations. For the present investigation the TKE is used to assess the unsteadiness of the flow in the wake of an axisymmetric BFS, where the most of turbulent structures appear. Figures 5.16 and 5.17 display the organization of the TKE levels for $M_\infty = 0.76$ and $M_\infty = 2.20$, respectively. Additionally, for comparison of different flow cases and nozzle lengths, in Table 5.4 the maximum TKE levels in the shear layer are provided. The TKE levels in Figures 5.16 and 5.17 and in Table 5.4 are normalized with the squared of the free stream velocity, U_∞^2. It is worth mentioning that the flow, especially in shear layer near to the base, contains structures with length-scales comparable or smaller than the spatial resolution of the PIV system used

during measurements. Processing of the these small structures results in modulation of the determined velocity distributions and hence underestimation of the *TKE* levels.

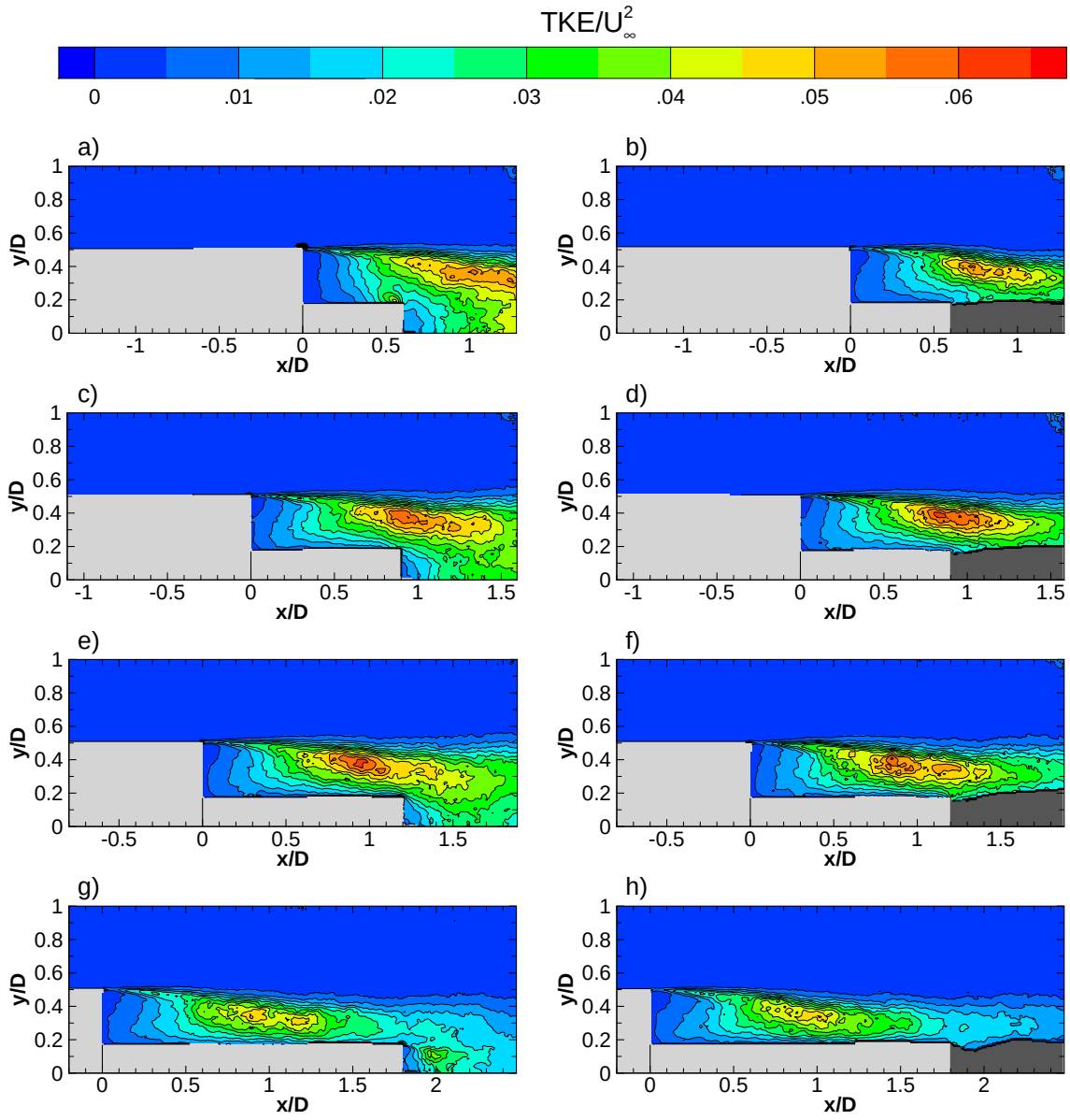

Figure 5.16: Turbulent kinetic energy for $M_\infty = 0.76$ case for increasing nozzle length (top to bottom); without plume (left) and with plume (right)

In Figures 5.16 and 5.17, low levels of *TKE* can be observed in the outer flow region, while shear layer and reattachment region show high levels of *TKE*. The high *TKE* levels in wake are enclosed by the outer boundary of the shear layer. Typical *TKE* levels in the freestream region related to turbulence intensity levels is in the range 1-2% U_∞ . From an hot-wire anemometry measurements conducted by Giepman et al. (2015) at a freestream Mach number

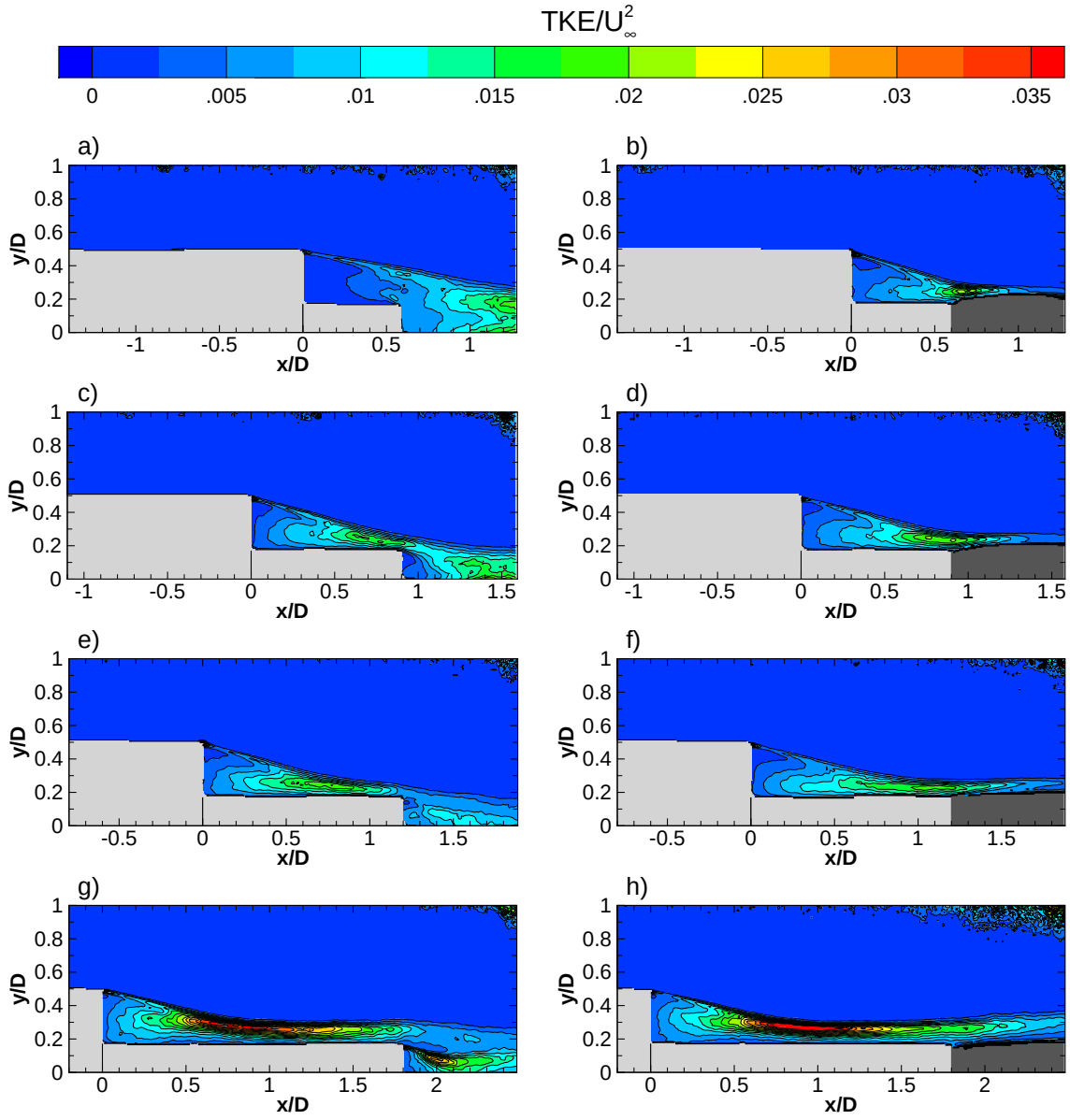

Figure 5.17: Turbulent kinetic energy for $M_\infty = 2.20$ case for increasing nozzle length (top to bottom); without plume (left) and with plume (right)

of $M_\infty = 1.70$, a turbulence intensity of approximately 0.5% U_∞ is found. At the top of the domain high *TKE* levels can be observed, especially for the supersonic case (Figure 5.17). These high *TKE* levels are due to higher measurement errors arising from insufficient flow seeding conditions. In order to avoid the propagation of these higher measurement errors to the pressure computation, the fluctuation levels in the region $y/D > 0.75$ are adjusted to a typical levels in the freestream. The high levels of *TKE* in shear layer and reattachment region can be associated to the presence of small-scale structures in the instantaneous flow organization as well as the large-scale unsteadiness in the base, which arises due to the

flapping motion of the shear layer, vortex shedding of large-scale turbulent structures and enlargement/shrinkage of the separated region (Deprés et al., 2004). As can be observed

	$M_\infty = 0.76$ (no plume)	$M_\infty = 0.76$ (plume)	$M_\infty = 2.2$ (no plume)	$M_\infty = 2.2$ (plume)
	TKE/U_∞^2	TKE/U_∞^2	TKE/U_∞^2	TKE/U_∞^2
$L/D = 0.6$	0.056	0.058	0.018	0.022
$L/D = 0.9$	0.060	0.064	0.018	0.021
$L/D = 1.2$	0.062	0.061	0.020	0.019
$L/D = 1.8$	0.051	0.049	0.038	0.042

Table 5.4: Values for the maximum turbulent kinetic energy in the shear layer

from Figure 5.16 and Table 5.4, for $M_\infty = 0.76$, the presence of exhaust plume does not show notable impact on the TKE organization or the maximum TKE levels, except for $L/D = 0.6$ case, where the reattachment occur on the plume. Notable differences in the TKE levels can be observed between the flow cases with different nozzle lengths. The highest TKE levels can be observed for $L/D = 0.9$ and $L/D = 1.2$ configurations, for which the reattachment of the shear layer occur on the nozzle and the flow downstream (hybrid reattachment) (compare Table 5.2). The high TKElevels and the increased unsteadiness for these two nozzle configurations can be attributed to the unsteadiness of the reattachment region, which moves back and forth. For $L/D = 0.6$, the reattachment always occur on the downstream flow (fluidic reattachment) while for $L/D = 1.8$ it always occur on the nozzle. A slightly lower TKE levels can be observed for $L/D = 0.6$ compared to $L/D = 0.9$ and $L/D = 1.2$ cases. The lowest TKE levels, however, is found for $L/D = 1.8$, which can be attributed to steady reattachment region compared to other nozzle configurations. For comparison, in Figure 5.18 (left) the turbulent kinetic energy distribution as obtained by Statnikov et al. (2013) for $M_\infty = 0.70$ and $L/D \gg 1.0$, is provided. The the TKE organization for $L/D = 1.8$ (Figure 5.16 (g-h)) appears to be in good agreement with the TKE distribution shown in Figure 5.18 (left). Small difference of approximately 0.003 in TKE levels can be observed between the current case (Figure 5.16 (g-h)) and the literature.

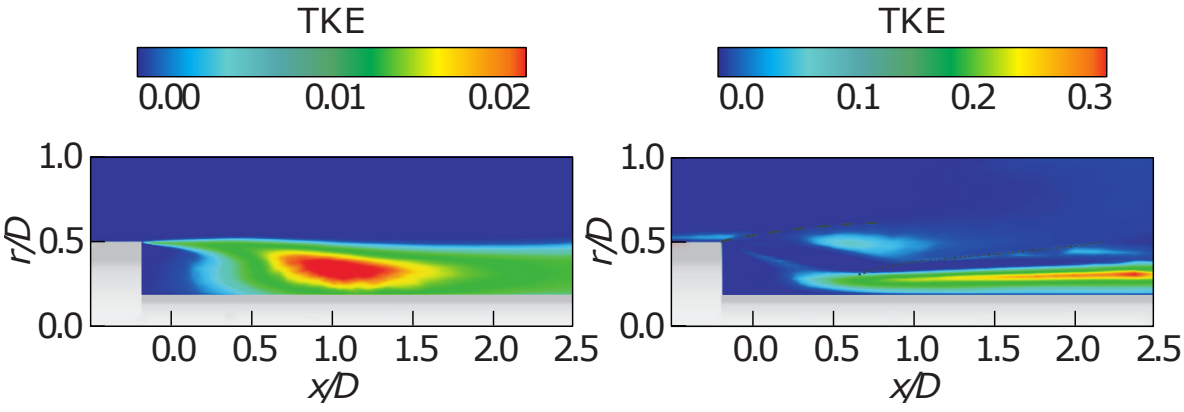

Figure 5.18: Turbulent kinetic energy distribution for transonic ($M_\infty = 0.70$) (left) and supersonic ($M_\infty = 6.0$) (right) flows according to Statnikov et al. (2013)

The TKE levels for the supersonic flow cases at $M_\infty = 2.20$ is shown in Figure 5.17 and

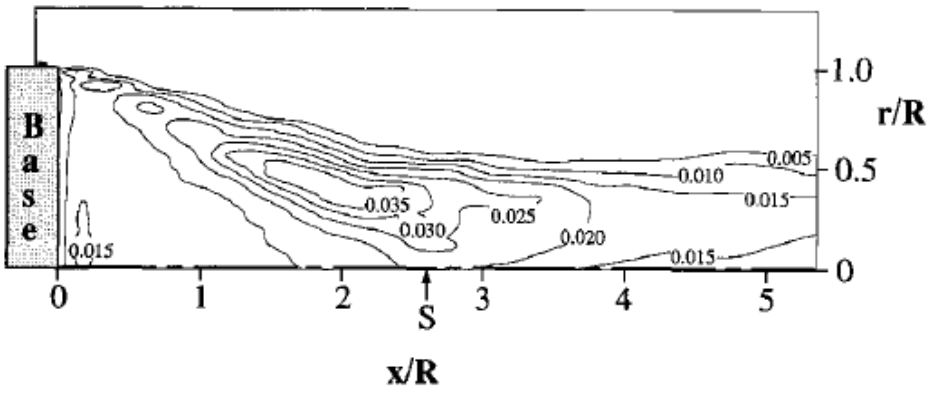

Figure 5.19: Turbulent kinetic energy distribution for $M_\infty = 2.50$. Adapted from Herrin and Dutton (1994)

Table 5.4. Much smaller *TKE* levels relative to U_∞^2 can be observed for the supersonic cases compared to subsonic one. In addition, especially for $L/D = 0.9$, 1.2 and 1.8, it can be observed that the regions with highest *TKE* levels occur much closer to the nozzle surface compared to subsonic cases. The flow cases with $L/D = 0.6$, 0.9 and 1.2 show similar maximum *TKE* levels, while twice as high *TKE* levels can be observed for $L/D = 1.8$ (Figure 5.17 (g-h)). For comparison, in Figure 5.18 (right), the *TKE* distribution for the supersonic flow case, as obtained by Statnikov et al. (2013) is provided. In general the *TKE* topology of the current $L/D = 1.8$ is more of less similar to the literature (Figure 5.18 (right)), however, the overall TKE values are not comparable. Figure 5.19 show the *TKE* distrribution as obtained by Herrin and Dutton (1994) for $M_\infty = 2.50$ (axisymmetric). The TKE levels for the current $L/D = 1.8$ case is in good agreement with the TKE results as shown in Figure 5.19, both show a maximum *TKE* level of 0.035. For all nozzle lengths at $M_\infty = 2.20$, the presence of exhaust plume seems to extend the elevated *TKE* levels in streamwise direction. According to Statnikov et al. (2013), due to the acceleration of the flow, the expansion fan at edge of an axisymmetric BFS result in a decrease of the *TKE*, whereas the presence of recompression shock increases the *TKE* again, as shown in Figure 5.18 (right). As seen in Figure 5.1, the recompression shock is present in all nozzle configuration. The twice as high *TKE* levels obtained for $L/D = 1.8$ cannot be attributed to the presence of recompression shocks because from the *TKE* results the recompression shocks seems to be steady in all cases because of the low *TKE* (<0.001). A possible mechanism for this increased *TKE* levels could be the convection of the vortical structures in the shear layer upon impingement. These vortical structures, which are formed due to Kelvin-Helmholz instabilities in the upstream part of the shear layer, may leave the shear layer and shed downstream, while other vortical structures may follow the shear layer and break down into smaller structures towards impingement. After impingement, some of these small structures may convect downstream while others may convect upstream into the recirculation region, where they may interact with the structures in the shear layer. The interaction of these small structures in the shear layer may lead to more turbulent shear layer, which in turn may attribute to higher *TKE* levels. From the mean streamwise velocity distribution, as shown in Figure 5.13, it can be observed that for $L/D = 1.8$ the zero streamwise velocity (black contour line) is slightly curved before meeting the nozzle surface compared to other nozzle configurations. This may indicate that more

structures are convected upstream into the recirculation region which in turn may interact with the structures in the shear layer. This interaction may lead to more turbulent shear layer, which in turn may result in higher *TKE* levels.

From the comparison of cases with a long nozzle configuration without exhaust plume and the cases with a short nozzle configuration but with an exhaust plume, it is observed that the presence of exhaust plume cannot be accurately modelled by replacing the exhaust plume with a solid geometry.

Mean Pressure Field

The procedure for computing the mean pressure fields from the obtained PIV data is outlined in section 3.3. This paragraph discusses the mean pressure results as obtained by the PIV based pressure reconstruction technique. In addition, these mean pressure results are compared with the literature.

Figure 5.20 and Figure 5.21 display the mean pressure field organization for $M_\infty = 0.76$ and $M_\infty = 2.20$ flow cases, respectively. In order to represent the relative pressure at a certain point in the flow field, the mean pressure results for both flow cases are normalized according to:

$$C_p = \frac{2\,(p - p_\infty)}{(\gamma M_\infty^2)} \tag{5.2}$$

where γ is specific heat ratio, p is the static pressure at a point in flow field and p_∞ and M_∞ are freestream pressure and Mach number, which are obtained from the isentropic flow relations. Comparison of the exact pressure levels is hampered by a systematic uncertainty in the overall pressure level for each case that is introduced by uncertainty of the boundary condition used during pressure reconstruction. As such, the current discussion will focus on the relative distribution.

Generally, from Figures 5.20 and 5.21, a low mean pressure region directly downstream of base can be observed for all nozzle lengths. As can be seen, the center of this low pressure region is situated at the core of the recirculation region where the velocity obtains a zero value (compare Figures 5.12 and 5.13). Strong pressure gradients can be noticed between high and low pressure region. In addition, from the bottom figures, it can be observed that downstream of the location where the pressure reaches it maximum value, the pressure starts to decrease again.

By comparing the mean pressure field of subsonic and supersonic flow cases, a considerable differences can be observed. For the subsonic flow cases ($M_\infty = 0.76$), it can be seen that the low pressure region develops upstream of the base step. While the supersonic flow cases ($M_\infty = 2.20$) display a more oblique mean pressure field organization and higher pressure gradients as a result of expansion waves at the base step and also recompression shocks at reattachment location. For comparison, in Figure 5.22 the mean pressure distribution as obtained by Statnikov et al. (2013) for $M_\infty = 0.70$ and $M_\infty = 6.0$ for $L/D \gg 1.0$ is provided. The mean pressure organization of the current $L/D = 1.8$ case at $M_\infty = 0.70$

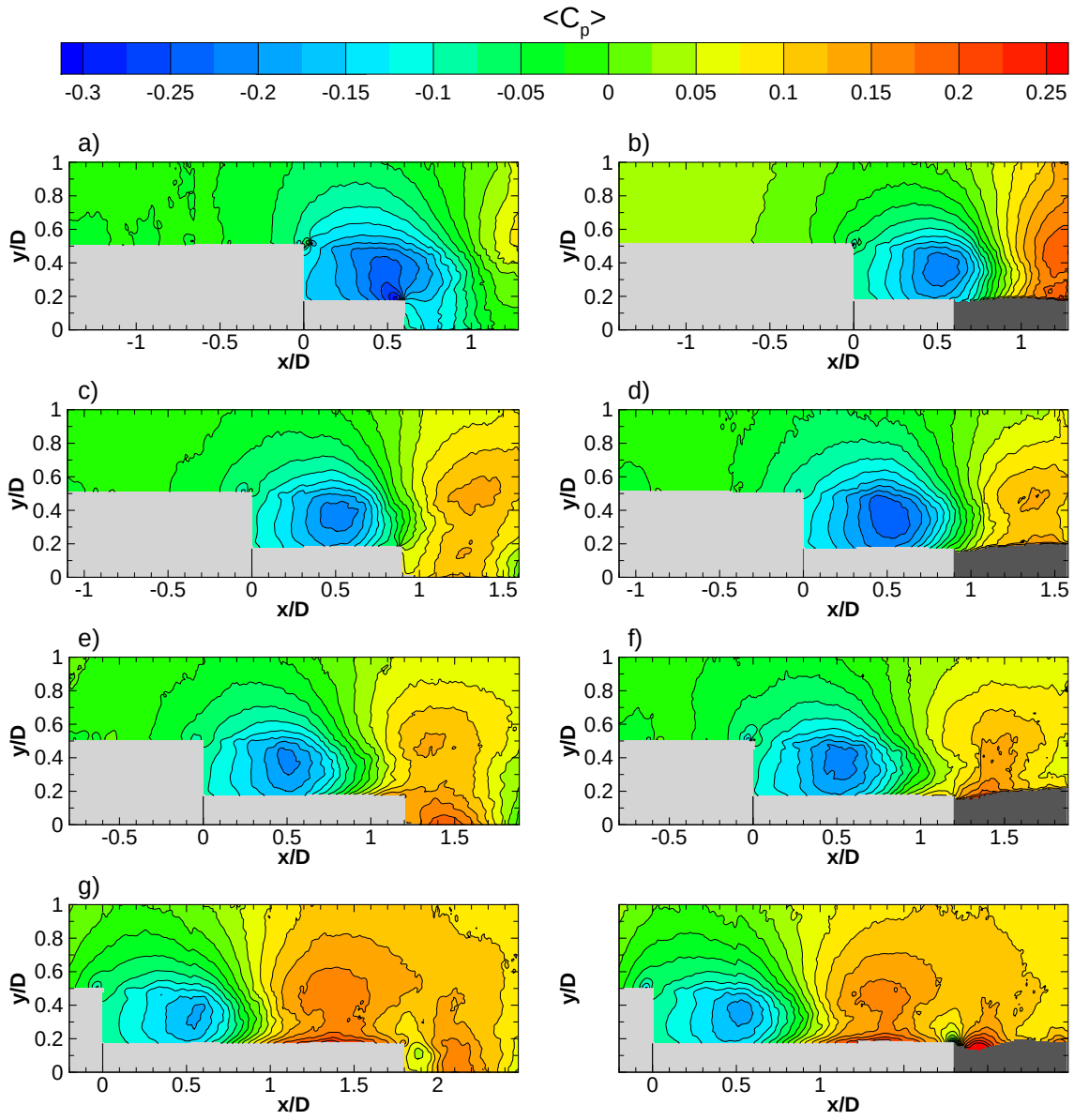

Figure 5.20: Mean pressure for $M_\infty = 0.76$ case for increasing nozzle length (top to bottom); without plume (left) and with plume (right)

and $M_\infty = 2.20$ (Figure 5.20(g) and Figure 5.21(g)) are quite similar to the mean pressure distribution as shown in Figure 5.22 (left). Large difference in the C_p values can be seen for the supersonic case (compare Figure 5.21(g) and Figure 5.22 (right)), which can be attributed to different free stream Mach numbers used.

From comparison of the subsonic and supersonic flow cases with and without presence of exhaust plume and for different nozzle lengths, a number of interesting observations can be drawn. Firstly, it can observed that the location of the low pressure region downstream of the

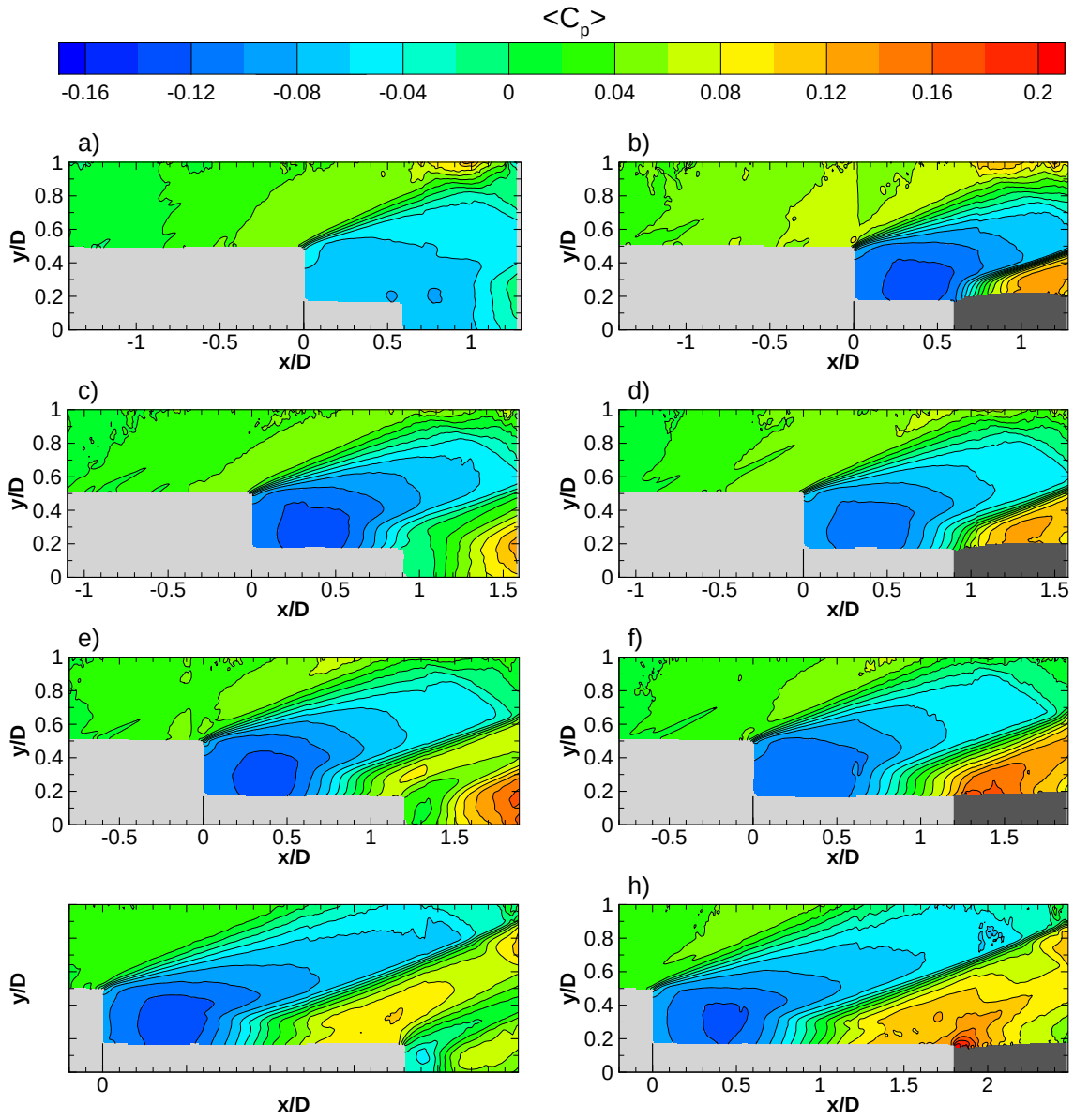

Figure 5.21: Mean pressure for $M_\infty = 2.2$ case for increasing nozzle length (top to bottom); without plume (left) and with plume (right)

base stays at the same location for different flow cases. Secondly, an increase in nozzle length causes the nozzle to move downstream into the high pressure region. As a result of this high pressure region, the shape the exhaust plume directly downstream of the nozzle exit is more over-expanded for the subsonic case or less under-expanded for the supersonic case, as shown at the bottom of Figures 5.20 and 5.21. The difference in the shape of exhaust plume have been validated by means of Schlieren visualization, as discussed in section 5.1.1.

The mean pressure field results as shown in both figures, display a number of artifacts which

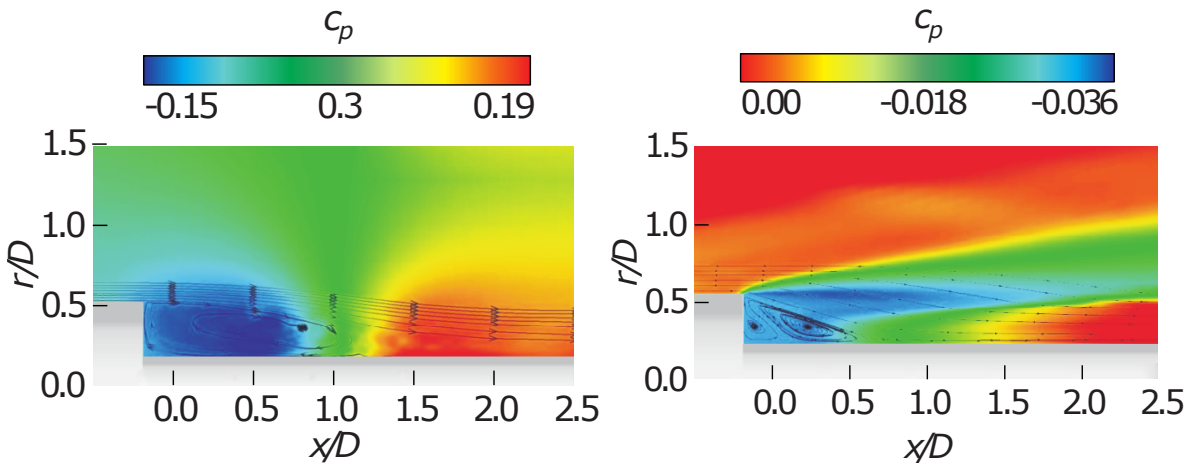

Figure 5.22: Mean pressure distribution for transonic ($M_\infty = 0.70$) (left) and supersonic ($M_\infty = 6.0$) (right) flows according to Statnikov et al. (2013)

can be related to the measurement errors during experiments, specifics of the experimental arrangements and data processing with DaVis software. Firstly, for the supersonic flow cases an increase in mean pressure can be noticed over the cylindrical main body before encountering the expansion fan emanating from the edge. This increase in mean pressure can be related to a series of weak shock waves created by pressure taps at the upper part of the cylindrical main body. Due to the supersonic nature of the flow this increase in mean pressure over the main body is not expected to arise from the flow dynamics downstream of the base. Secondly, the mean pressure field for supersonic case display a number of vertical features (e.g. Figure 5.21(b) at $x/D = 0$) which occur due to the stitching of the average vector field obtained from the PIV recording. Lastly, the mean pressure fields for the subsonic flow cases display small features near the edge of the step resulting from measurement errors in that area due to reflections of laser light. The contribution of these measurement errors also resulted in hot-spots of *TKE* levels near the step edge (compare Figure 5.16(a) and Figure 5.20(a)).

Table 5.5 show the minimum mean pressure ($C_{p_{\min}}$) values and its corresponding locations (x/D, y/D) for $M_\infty = 0.76$ and $M_\infty = 2.20$ and all nozzle lengths. The $L/D = 0.6$ case, for which fluidic reattachment occur, show a noticeable difference in $C_{p_{\min}}$ between the cases with and without exhaust plume, for both subsonic and supersonic flow cases. For the subsonic flow cases the presence of exhaust plume for $L/D = 0.6$ result in an increase of $C_{p_{\min}}$ value. This is not expected because according to Deprés et al. (2004) the presence of exhaust plume would rather decrease the pressure due the jet suction effect. The supersonic case on the other hand show a decrease of $C_{p_{\min}}$ value for $L/D = 0.6$ with exhaust plume, which can be linked to the jet suction effect. Moreover, Table 5.5 show that the streamwise location of $C_{p_{\min}}$ does not vary much, it remains at approximately $x/D \approx 0.5$. In order to show the dynamic effect of the recirculation region on the base and the nozzle structure, the mean pressure distributions coefficient (C_p) along the base and the nozzle surfaces are presented here. Figure 5.23 show mean C_p distribution along the nozzle surface for $M_\infty = 0.76$ and $L/D = 0.6$, with and without exhaust plume. Since $L/D = 0.6$, the mean C_p data only extends to $x/D = 0.6$. For comparison, Figure 5.23 also show the mean C_p distribution as reported by Deprés et al.

	$M_\infty = 0.76$ (no plume)			$M_\infty = 0.76$ (plume)			$M_\infty = 2.2$ (no plume)			$M_\infty = 2.2$ (plume)		
	$C_{p_{\min}}$	x/D	y/D	$C_{p_{\min}}$	x/D	y/D	$C_{p_{\min}}$	x/D	y/D	$C_{p_{\min}}$	x/D	y/D
$L/D = 0.6$	-0.309	0.547	0.186	-0.222	0.514	0.362	-0.081	0.520	0.208	-0.132	0.463	0.287
$L/D = 0.9$	-0.211	0.493	0.386	-0.246	0.545	0.346	-0.130	0.444	0.263	-0.114	0.466	0.30
$L/D = 1.2$	-0.207	0.522	0.385	-0.220	0.530	0.392	-0.131	0.395	0.267	-0.117	0.392	0.284
$L/D = 1.8$	-0.184	0.570	0.376	-0.186	0.545	0.390	-0.137	0.460	0.356	-0.127	0.428	0.298

Table 5.5: $C_{p_{\min}}$ values with corresponding locations

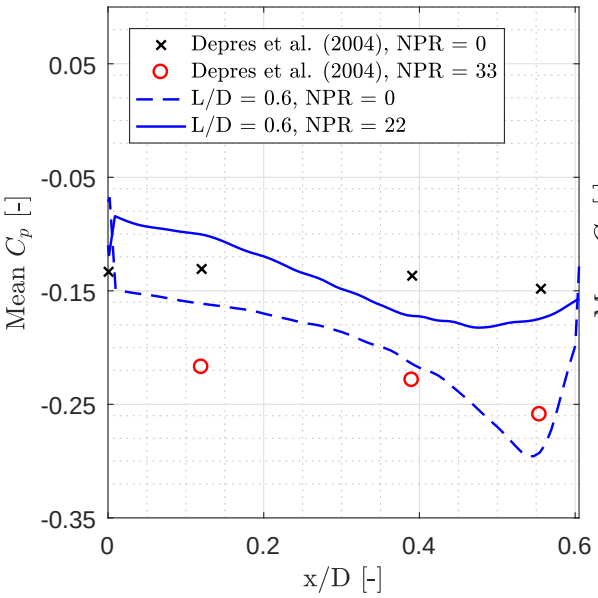

Figure 5.23: Mean C_p distribution for $M_\infty = 0.76$ and $L/D = 0.6$

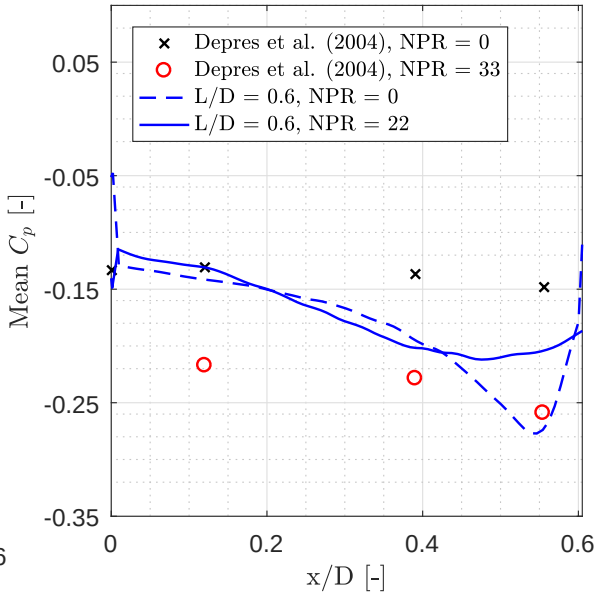

Figure 5.24: Mean C_p distribution for $M_\infty = 0.76$ for $L/D = 0.6$, with BC set to constant value

(2004) for $L/D = 0.6$ case with and without exhaust plume. As shown, an almost constant difference in mean C_p distribution up to approximately $x/D \approx 0.55$ can be observed between the cases with and without exhaust plume. After $x/D \approx 0.55$, the current $L/D = 0.6$ case without exhaust plume show a sudden increase of mean C_p distribution. This sudden increase is not physical and can be attributed to the presence of small structure at $x/D \approx 0.55$ (see Figure 5.20(a)), which probably occur due to the processing or laser light reflection. Also at $x/D = 0$, where the mean C_p distribution suddely decreases for the case without plume or increases for the case with plume, presence of small structures can be observed. Accoring to Deprés et al. (2004), for the fluidic reattachment case ($L/D = 0.6$), the presence of exhaust plume causes the static pressure all along the nozzle surface to decrease due to the jet-suction effect. However, as shown in Figure 5.23, the mean C_p distribution for the current case increases when exhaust plume is present. Also as reported by Bergman (1970), due to the presence of plume there is entrainment which acts to decrease the pressure. This increase can be attributed to the value of the boundary condition set at the upper left corner of the frame when computing the pressure. The value of this boundary condition is not constant and it may cause the mean C_p value to shift. A possible solution is to set a constant value for the

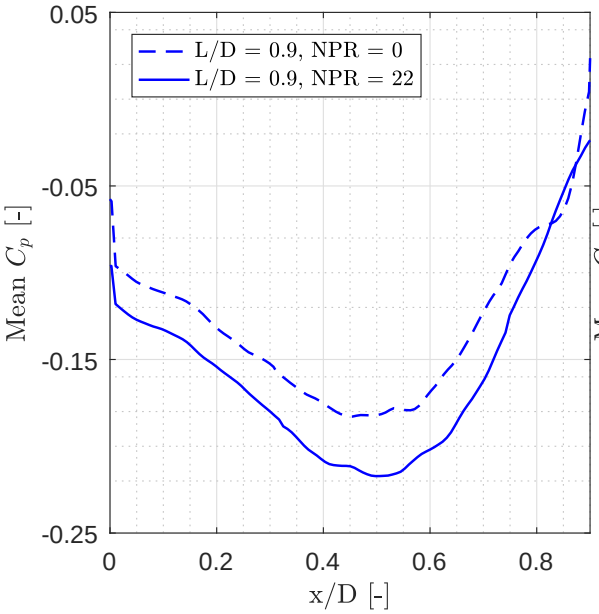

Figure 5.25: Mean C_p distribution for $M_\infty = 0.76$ and $L/D = 0.9$

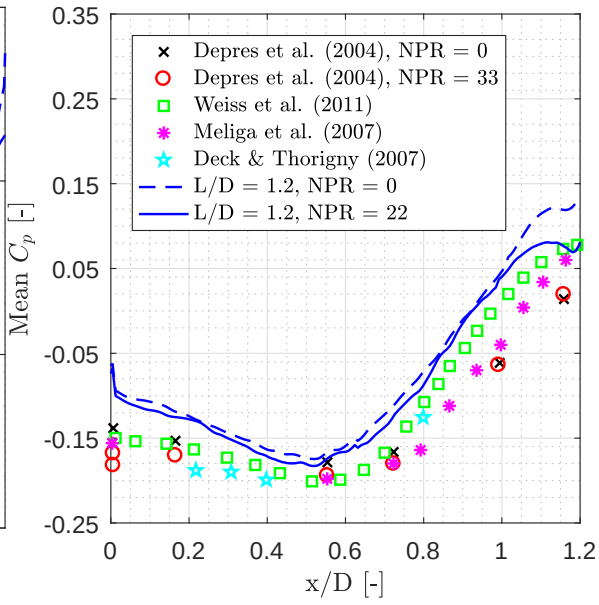

Figure 5.26: Mean C_p distribution for $M_\infty = 0.76$ and $L/D = 1.2$

boundary condition, the result of which is shown in Figure 5.24. The mean C_p results for the cases with and without exhaust plume as reported by Deprés et al. (2004), show a larger difference than the current cases. A difference of approximately 0.1 is observed for the data points from Deprés et al. (2004) whereas the current data show a difference of approximately 0.05 between the cases with and without exhaust plume.

Figure 5.25 show the mean C_p distribution for $M_\infty = 0.76$ and $L/D = 0.9$ with and without exhaust plume. This case is similar to fluidic reattachment case ($L/D = 0.6$). However, in contrast to $L/D = 0.6$ case, the presence of plume results in decrease of mean C_p distribution (see Figure 5.25 and Table 5.5), which is also in agreement with Deprés et al. (2004). A sharp decrease in mean C_p distribution can be observed at $x/D = 0$, similar to the $L/D = 0.6$ case. Figure 5.26 show the mean C_p distribution for $M_\infty = 0.76$ and $L/D = 1.2$ with and without exhaust plume. For comparison, Figure 5.26 also show the results as reported by Deprés et al. (2004), Deck and Thorigny (2007), Weiss and Deck (2011) and Meliga and Reijasse (2007) for $L/D = 1.2$. The current results are in agreement with these reported results. Initially the mean C_p distribution decreases up to $x/D \approx 0.55$ which is then followed by an increase indicating the onset of reattachment process further downstream. The difference between plume on and plume off cases is small, which can be attributed to the fact that the jet-suction effect as reported by Deprés et al. (2004) is absent for this hybrid case. As shown, the case with exhaust plume display a slight decrease in mean C_p compared to the case without plume, which is in agreement with the results from Deprés et al. (2004). However, after the reattachment ($x/D \approx 1.1$), the decrease in pressure seems to be larger, which can be linked to the bigger impact of the plume in that region due to entertainment. By comparing the C_p values of the present experiment with Deprés et al. (2004), a poor agreement can be observed, especially close at the base corner and towards the reattachment point, with an approximate

deviation of 0.05. Better agreement can be seen at approximately $x/D \approx 0.6$.

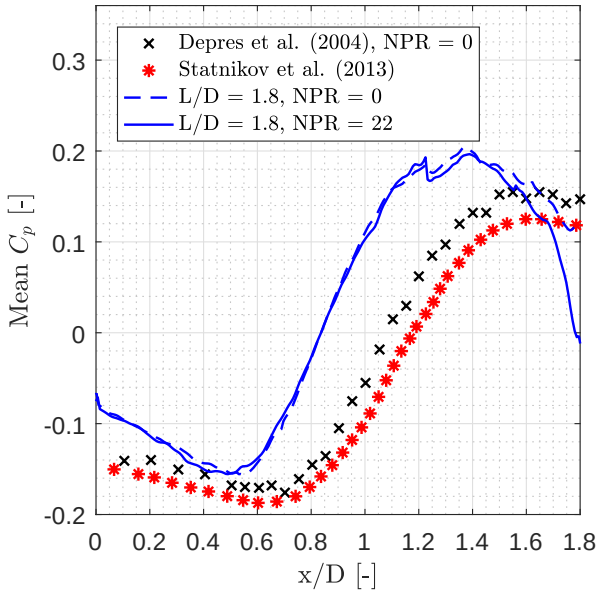

Figure 5.27: Mean C_p distributions for $M_\infty = 0.76$ and $L/D = 1.8$

Figure 5.27 show a comparison of the mean wall C_p distribution for $M_\infty = 0.76$ and $L/D = 1.8$ with and without exhaust plume with the results obtained by Deprés et al. (2004) and Statnikov et al. (2013). In this case the reattachment is on the nozzle (solid reattachment). The mean C_p distribution for present measurements with and without exhaust plume are almost similar up $x/D \approx 1.4$. After this point due to the influence of the plume the wall pressure distribution start to deviate. The result from present measurement without exhaust plume is in agreement with the result for $L \gg D$ obtained by Deprés et al. (2004) and Statnikov et al. (2013). A slight decrease in mean C_p distribution can be observed at $x/D \approx 0.6$ for the case without plume.

Figure 5.29 show mean C_p distribution for $M_\infty = 2.20$ and for all nozzle lengths. For the comparison also the mean C_p distribution for $M_\infty = 0.76$ and all nozzle lengths is provided. By comparing Figure 5.29 with Figure 5.28 and Table 5.5, a lower pressure can be observed for the supersonic case, which can be expected as a result of higher Mach number. Moreover, Figure 5.29 display a sharp pressure drop at $x/D = 0$ which can be attributed to the presence of an expansion fan at the edge. This expansion fan causes the flow to accelerate and hence reduce the pressure. Since the expansion fan is isentropic, the pressure computation can still be performed. The only issues for the pressure computation is oblique shock waves, which are not isentropic and which can disrepute the validity of the used pressure reconstruction technique. The current supersonic pressure results are not compared with the literature due lack of investigation on the supersonic pressure in the wake of an axisymmetric BFS flows.

Due to shock wave the total pressure and the Mach number downstream of the shock are different. These downstream properties are obtained by using Schlieren images and the following

oblique shock wave relations (Nasa, 2017):

$$\cot(\theta) = \tan(\mu)\left(\frac{(\gamma+1)M^2}{2\left(M^2\sin^2(\mu)-1\right)} - 1\right) \tag{5.3}$$

$$M_1^2\sin^2(\mu-\theta) = \left(\frac{(\gamma-1)M^2\sin^2(\mu)+2}{2\gamma M^2\sin^2(\mu)-(\gamma-1)}\right) \tag{5.4}$$

$$\frac{p_{t1}}{p_{t0}} = \left(\frac{(\gamma+1)M^2\sin^2(\mu)}{(\gamma-1)M^2\sin^2(\mu)+2}\right)^{\frac{\gamma}{\gamma-1}}\left(\frac{(\gamma+1)}{2\gamma M^2\sin^2(\mu)-(\gamma-1)}\right)^{\frac{1}{\gamma-1}} \tag{5.5}$$

where θ is the deflection angle, μ is the shock angle, M and M_1 are the upstream and downstream Mach number and finally p_{t0} and p_{t1} are the upstream and downstream total pressures, respectively. The shock angle, μ in Equation (5.3) is determined from the Schlieren images, which than is used to estimate the Mach number upstream of the shock ($M = 1/\sin\mu$) and also the deflection angle, θ. Knowing the deflection and shock angle, Equation (5.4) is then used to determine the Mach number downstream of the shock. From the Schlieren image a shock angle of $\mu = 30.8°$ is found. Finally, using Equation (5.5) result in a total pressure of $p_{t0} = p_{t1} \cdot 0.999$ downstream of the shock. This show that the total pressure does not change that much after the shock.

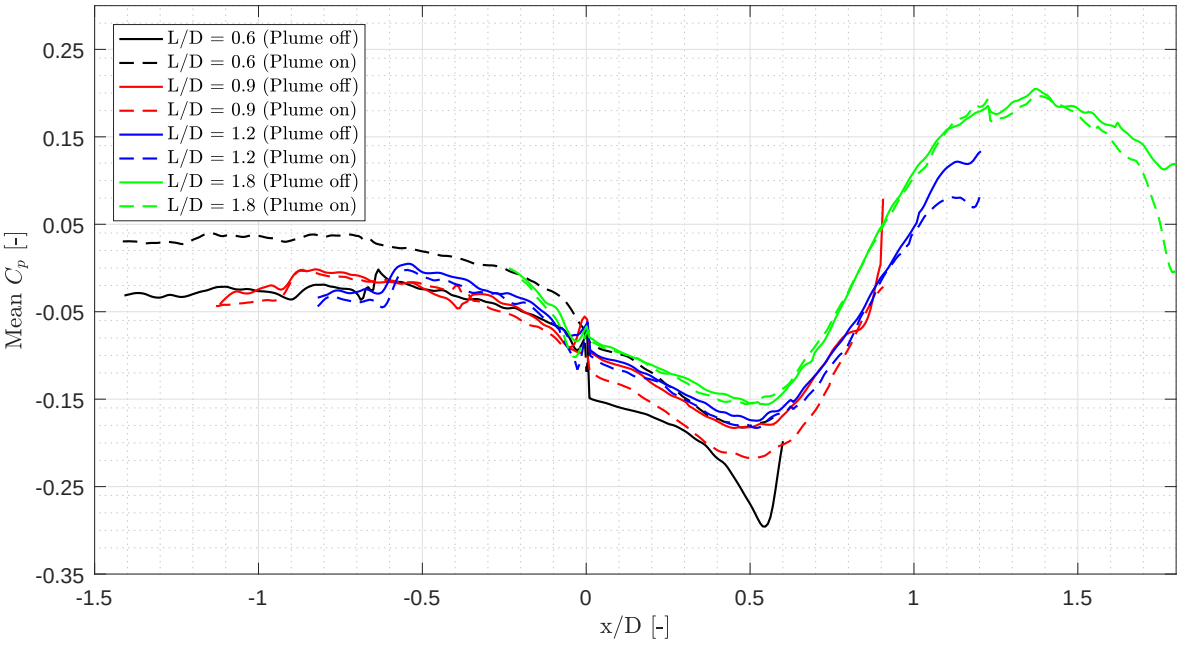

Figure 5.28: Mean C_p distributions for $M_\infty = 0.76$

Figure 5.30 and Figure 5.31 show the mean C_p distribution along the base for $M_\infty = 0.76$ and $M_\infty = 2.20$ flow cases, respectively. Both flow cases show a nearly homogeneous base

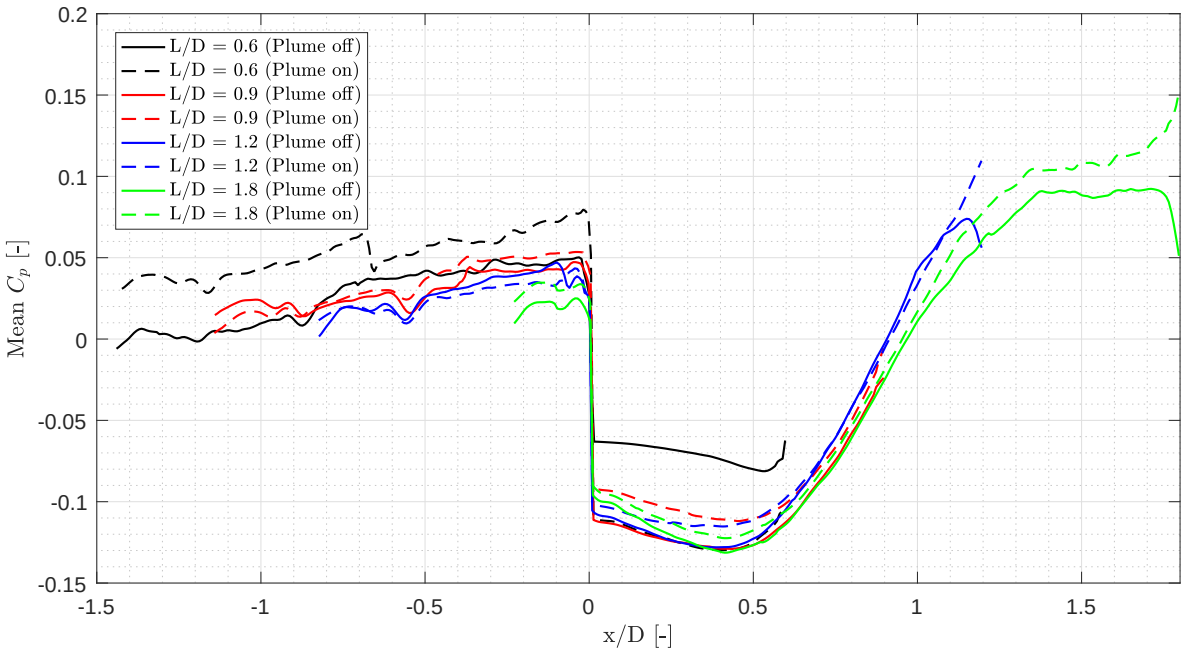

Figure 5.29: Mean C_p distributions for $M_\infty = 2.20$

C_p distribution up to $y/D \approx 0.45$ for all nozzle lengths, with and without exhaust plume. For subsonic cases, as shown in Figure 5.30, similar to the mean C_p distribution along the nozzle surface, the $L/D = 0.6$ case without exhaust plume show a large decrease in base C_p distribution compared to plume on case. Similar explanation for this decrease as given before for C_p distribution along the nozzle also applies for the base C_p distribution. Furthermore, from Figure 5.30 it can be seen that for increasing nozzle length the base pressure slightly increases. For $L/D = 0.9$, 1.2 and 1.8 with exhaust plume, the pressure seems to decrease slightly compared to plume on cases.

Reverse Flow Probability

According to Spazzini et al. (2001), reverse flow probability (RFP) can be obtained by analyzing the percentage of time a vector is directed upstream. RFP can be useful in determining the unsteadiness of the flow but also the mean position of the reattachment point (Spazzini et al., 2001), which for the current investigation have been obtained by taking the streamwise location where the zero streamwise velocity contour meets the geometry or the plume, as discussed in section 5.2.2.

Figures 5.32 and 5.33 show the RFP organization for $M_\infty = 0.76$ and $M_\infty = 2.20$, respectively. For RFP = 1, the flow (vectors) is always directed upstream, while for RFP = 0, the the flow (vectors) is directed downstream 100% of the time. For both subsonic and supersonic flow cases it can be observed that the presence of exhaust plume does not seems to affect the overall RFP organization, except for the $L/D = 0.6$ case where the fluidic reattachment

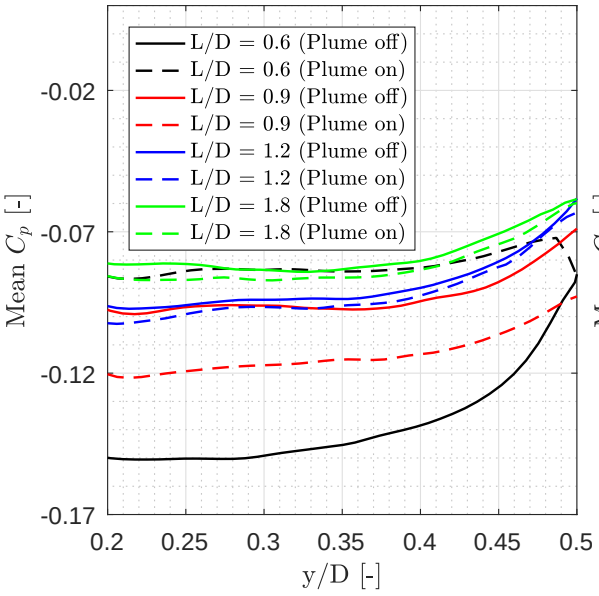

Figure 5.30: Mean base C_p distribution for $M_\infty = 0.76$

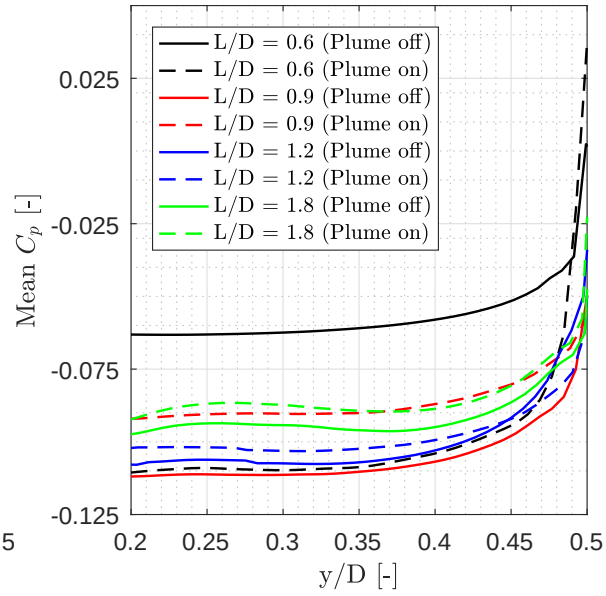

Figure 5.31: Mean radial C_p distributions for $M_\infty = 2.2$

occur. For the subsonic flow cases the region where the flow is essentially directed upstream (RFP = 1) appears to be located approximately between $x/D = 0.2$ - $x/D = 0.9$ for all flow cases, except for the $L/D = 0.6$. Without exhaust plume, a large region where the flow is essentially directed upstream (RFP = 1) can be observed at the nozzle exit for the $L/D = 0.6$ compared to other cases. This suggest that the flow (recirculation region) may extent to inside the nozzle, as previously mentioned in section 5.2.2. When the exhaust plume is present, the location of the region with RFP = 1 is moved to the nozzle surface. In all flow cases a secondary recirculation region can be observed at the corner of step ($x/D = 0$). For $L/D = 0.6$ at $M_\infty = 0.76$, also very small recirculation can be seen at x/D = 0.5 when the plume is absent. When plume is present this small recirculation disappear and the secondary recirculation region at the corner reduces in size. This can be attributed to jet-suction which has a stabilizing effect, as mentioned previously in sections 5.2.2 and 5.2.2. For the supersonic flow cases, the region where the flow is essentially directed upstream (RFP = 1), are moved slightly upstream towards the corner. Also for the supersonic small secondary recirculation region can be observed at the corner, however these are much smaller compared to subsonic flow cases. For $L/D = 1.8$, the region where the flow is essentially directed upstream is bigger and longer compared to other flow cases.

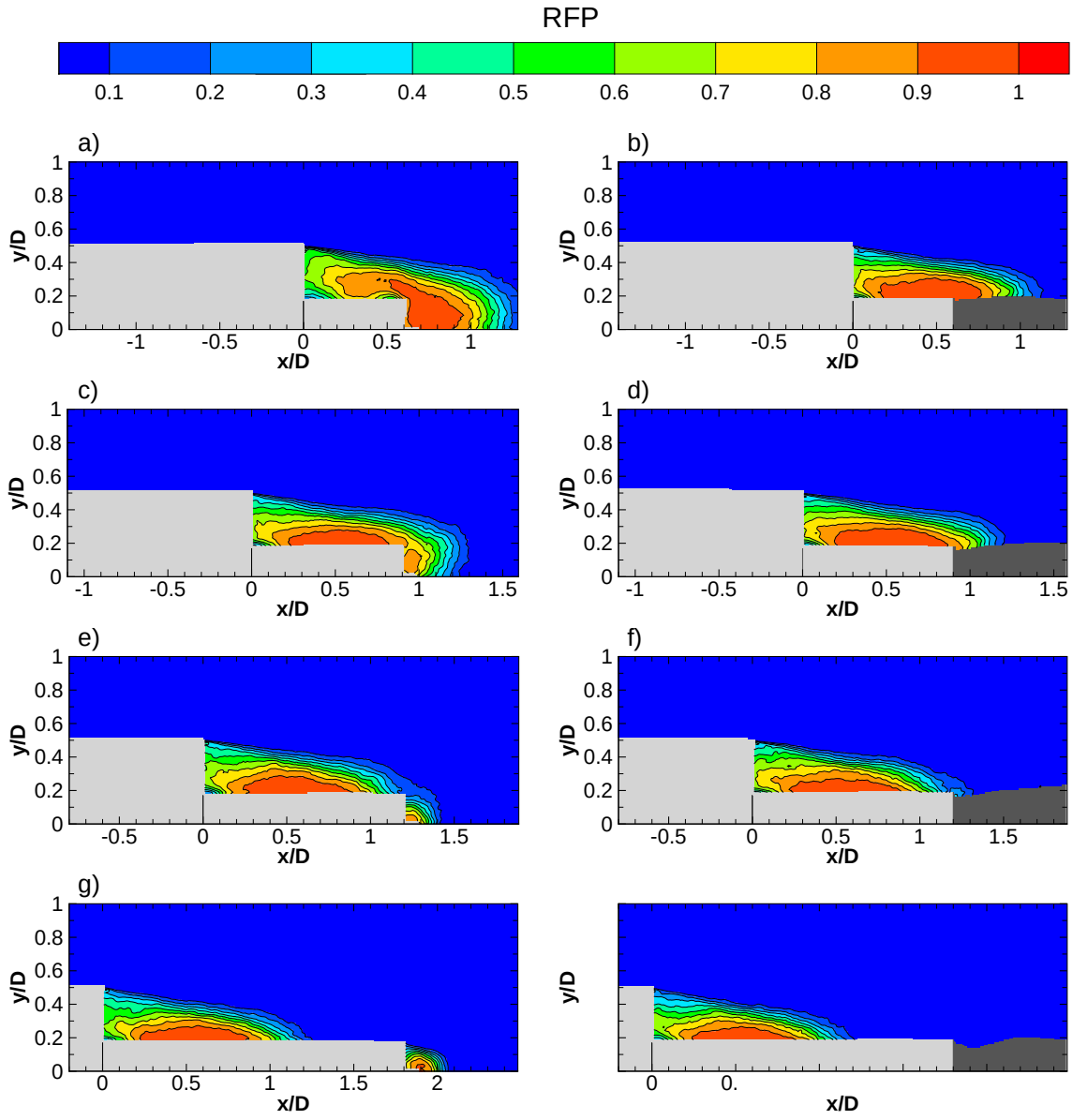

Figure 5.32: Reverse flow probabily for $M_\infty = 0.76$ case for increasing nozzle length (top to bottom); without plume (left) and with plume (right)

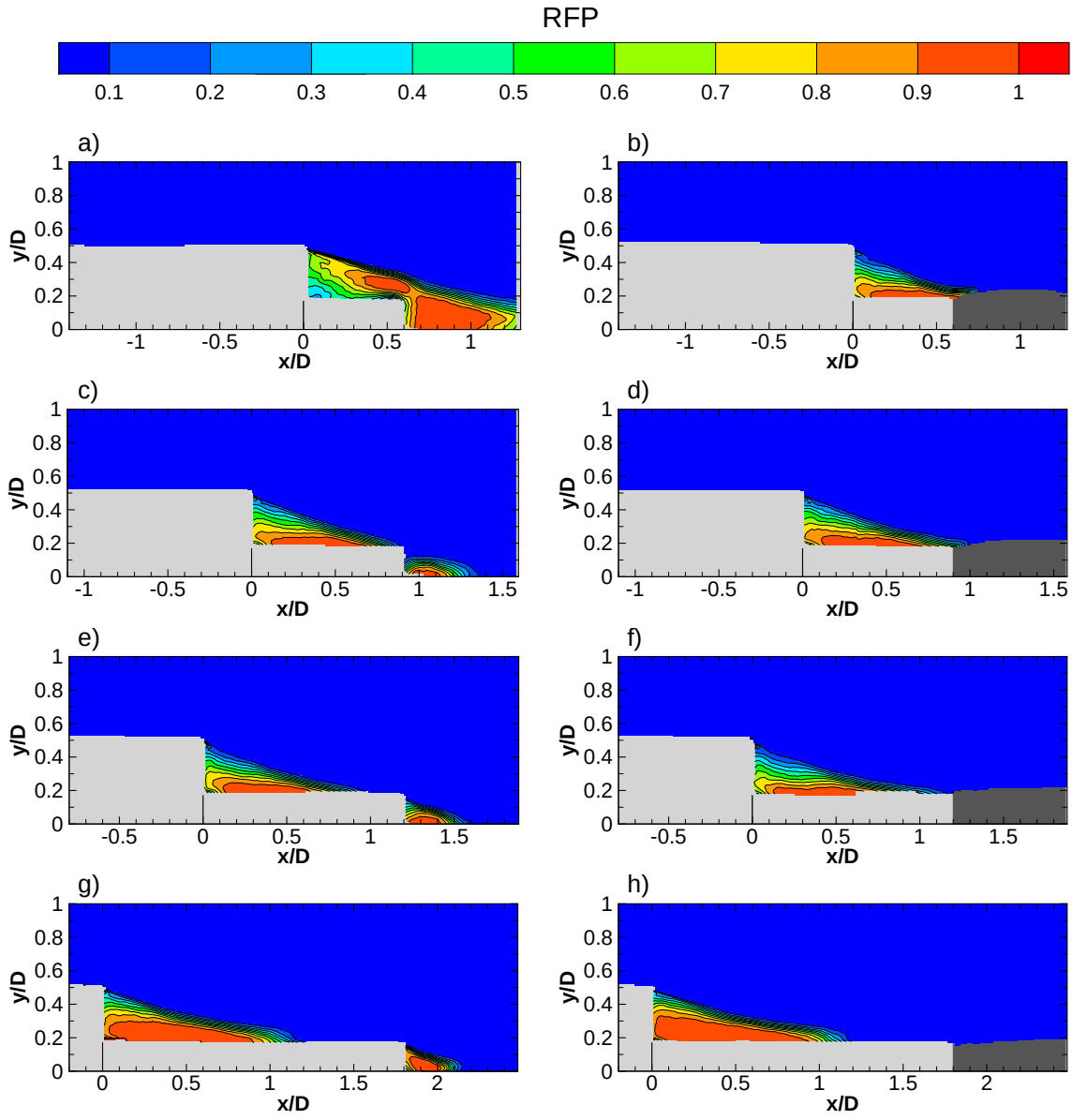

Figure 5.33: Reverse flow probability for $M_\infty = 2.20$ case for increasing nozzle length (top to bottom); without plume (left) and with plume (right)

Chapter 6

Conclusions and Recommendations

This chapter provides conclusions and recommendation for the future work that are drawn from the work presented in chapter 5.

6.1 Conclusions

PIV and Schlieren experiments have been carried out to investigate the effect of varying nozzle length and the presence of exhaust plume on the flow topology and mean pressure distribution in the wake of an axisymmetric BFS at freestream Mach numbers of $M_\infty = 0.76$ and $M_\infty = 2.20$, respectively. For this investigation four different nozzle configurations with the lengths of $L/D = 0.6$, 0.9, 1.2 and 1.8 with and without the presence of exhaust plume have been tested. These tests showed that, depending on the nozzle length, the shear layer will impinge on the nozzle (solid reattachment), on the flow downstream of the nozzle (fluidic reattachment) and intermittently on the nozzle and on the flow downstream (hybrid reattachment).

The wake of an axisymmetric BFS at freestream Mach numbers of $M_\infty = 0.76$ and $M_\infty = 2.20$ differ significantly. For $M_\infty = 0.76$ flow cases, it is found that an increase in nozzle length and presence of exhaust plume did not cause considerable change in mean reattachment length (L_R). In contrast to reattachment length, the absolute maximum backflow velocity ($|\bar{u}_{\min}|$) was found to decrease for longer nozzles. From the relative turbulent kinetic energy (TKE/U_∞^2) results, it is noticed that the presence of exhaust plume for $M_\infty = 0.76$ cases did not affect the organization of the TKE levels except for $L/D = 0.6$ case. The cases with hybrid reattachment ($L/D = 0.9$ and 1.2) show higher TKE levels due to an increased unsteadiness. Furthermore, the $L/D = 1.8$ case with solid reattachment has shown a considerably lower TKE/U_∞^2 compared to other cases.

For $M_\infty = 2.20$ flow cases, the mean velocity results showed a longer reattachment length

for an increase in nozzle length and presence of exhaust plume compared to $M_\infty = 0.76$ flow cases. In contrast to $M_\infty = 0.76$ flow cases, an increase in the absolute maximum backflow velocity ($|\bar{u}_{\min}|$) was found for longer nozzles. In general, for $M_\infty = 2.20$ flow cases lower TKE/U_∞^2 levels have been observed compared to $M_\infty = 0.76$ flow cases. For $L/D = 1.8$ case, where the shear layer impinges on the nozzle (solid reattachment), significantly higher TKE/U_∞^2 levels were found compared to other supersonic flow cases. Moreover, the presence of exhaust plume caused elongation of the region with elevated TKE/U_∞^2 levels.

From mean pressure results large differences in pressure fields were found for $M_\infty = 0.76$ and $M_\infty = 2.20$ flow cases. Results showed a fixed location of the low-pressure region downstream of the base for different flow cases with and without exhaust plume and for different nozzle lengths. Furthermore, an increase in nozzle length was found to result in a higher local pressure region at the nozzle exit. As result of this, the exhaust plume of the subsonic case was more over-expanded, whereas for supersonic case the exhaust plume was less under-expanded.

From the comparison of cases with a long nozzle configuration without exhaust plume and the cases with a short nozzle configuration but with an exhaust plume, it is observed that the presence of exhaust plume cannot be accurately modelled by replacing the exhaust plume with a solid geometry.

6.2 Recommendations

Due to time constrain, the exhaust plume for the present investigation was not seeded. However, for better characterization of the complex turbulent interaction developing in the wake of the model between the external flow and the supersonic exhaust plume, for the future work it is recommended to introduce seeding particles ($TiO2$ particles) in the exhaust plume. Furthermore, seeding the exhaust plume will also solve the problems related to occurrence of outliers in the plume region due to the absent of seeding particle in that region, which can be problematic for the subsequent analysis of pressure.

During the experiments with exhaust plume on, due to the control system of the compressed air supply, the total jet pressure that was set, dropped about 10% over the duration of each run (approximately 30 seconds). In order to avoid that total pressure drop during each run, it is recommended to revise the system that controls the jet pressure or another option is to reduce the pressure in the tanks from 300 bar to approximately 100 bar. From the Schlieren results, it is evident that for $M_\infty = 0.76$ flow cases the flow in the nozzle of over-expanded plume separates. The flow separation in the nozzle may reduce the jet Mach number. In order to avoid flow separation in the nozzle for over-expanded plume, it recommended to use higher total jet pressure or use bell shaped (contoured) nozzle instead.

For the present investigation a pressure tap located 65 mm upstream of the step is used to measure the static pressure during a run. This pressure tap is outside of the FOV that is investigated. In order to validated the reconstructed pressure field, it is highly recommended

to measure the reference pressure in the FOV. For the current investigation this mean using the most downstream pressure tap, which is in the FOV that has to be investigated. Finally, it also is recommended to use fully closed nozzle exit when conducting experiments without exhaust plume since there is possibility that the flow moves inside the nozzle.

Bibliography

D. E. Abbott and S. J. Kline. Experimental Investigation of Subsonic Turbulent Flow Over Single and Double Backward Facing Steps. *Journal of Basic Engineering*, 84(3):317, 1962. ISSN 00219223. doi: 10.1115/1.3657313.

E. W. Adams and J. P. Johnston. Effects of the separating shear layer on the reattachment flow structure part 2: Reattachment length and wall shear stress. *Experiments in Fluids*, 6(7):493–499, Jan 1988. ISSN 1432-1114. doi: 10.1007/BF00196511.

J.D. Anderson. *Introduction to Flight (McGraw-Hill Series in Aeronautical and Aerospace Engineering)*. McGraw-Hill Science/Engineering/Math, 5 edition, March 2004. ISBN 0072990716.

Arianespace. Ariane 5 Users Manual. October 2016.

W.J. Bannink and M.M.J. Schoones. *Base flow and exhaust plume interaction. Part 1: Experimental study*. Delft University Press, 1998.

W.J. Bannink, P.J. Bakker, and E.M. Houtman. *Festip aerothermodynamics: experimental investigation of base flow and exhaust plume interaction*. Delft University of Technology, Faculty of Aerospace Engineering, 1997.

L. H. Benedict and R. D. Gould. Towards better uncertainty estimates for turbulence statistics. *Experiments in Fluids*, 22:129–136, 1996. ISSN 0723-4864. doi: 10.1007/s003480050030.

D. Bergman. Effects of engine exhaust flow on boattail drag. *8th Aerospace Sciences Meeting*, 8(6):434–439, 1970. ISSN 00218669. doi: 10.2514/6.1970-132.

M. Bitter, S. Scharnowski, R. Hain, and C.J. Kähler. High-repetition-rate PIV investigations on a generic rocket model in sub- and supersonic flows. *Experiments in Fluids*, 50(4): 1019–1030, 2011. ISSN 07234864. doi: 10.1007/s00348-010-0988-8.

M. Bitter, T. Hara, R. Hain, D. Yorita, K. Asai, and C.J. Kähler. Characterization of pressure dynamics in an axisymmetric separating/reattaching flow using fast-responding pressure-sensitive paint. *Experiments in Fluids*, 53(6):1737–1749, Dec 2012. ISSN 1432-1114. doi: 10.1007/s00348-012-1380-7. URL https://doi.org/10.1007/s00348-012-1380-7.

P. Blinde, K. Lynch, B. van Oudheusden, J. Schneiders, and F.F.J. Schrijer. Assessment of instantaneous pressure determination in a transonic base flow based on four-pulse tomographic PIV. *17th International Symposium on Applications of Laser Techniques to Fluid Mechanics*, 2014.

P. Bradshaw and F.Y.F. Wong. The reattachment and relaxation of a turbulent shear layer. *Journal of Fluid Mechanics*, 52(01):113–135, 1972. ISSN 0022-1120. doi: doi:10.1017/S002211207200299X.

F. K. Browand. An experimental investigation of the instability of an incompressible, separated shear layer. *Journal of Fluid Mechanics*, 26(2):281307, 1966. doi: 10.1017/S0022112066001241.

Z. Chen, S.H. Yi, L. He, L.F. Tian, and Y.Z. Zhu. An experimental study on fine structures of supersonic laminar/turbulent flow over a backward-facing step based on NPLS. *Chinese Science Bulletin*, 57(6):584–590, 2012. ISSN 10016538. doi: 10.1007/s11434-011-4888-y.

D Coulon. Vulcain-2 cryogenic engine passes first test with new nozzle extension. *ESA Bulletin*, pages 123–124, 2000. URL http://www.esa.int/esapub/bulletin/bullet102/Coulon102.pdf.

R. de Kat. *Instantaneous planar pressure determination from particle image velocimetry*. Phd thesis, Delft University of Technology, 2012.

R. de Kat and B. W. van Oudheusden. Instantaneous planar pressure determination from piv in turbulent flow. *Experiments in Fluids*, 52(5):1089–1106, May 2012. ISSN 1432-1114. doi: 10.1007/s00348-011-1237-5. URL https://doi.org/10.1007/s00348-011-1237-5.

S. Deck and P. Thorigny. Unsteadiness of an axisymmetric separating-reattaching flow: Numerical investigation. 19(6), 2007. ISSN 10706631. doi: 10.1063/1.2734996.

S. Deck, F. Simon, A. Merlen, P. Guillen, and P. Sagaut. Numerical simulation of the compressible mixing layer past an axisymmetric trailing edge. *Journal of Fluid Mechanics*, 591(2007):215–253, 2007. ISSN 0022-1120. doi: 10.1017/S0022112007008129.

D. Deprés, P. Reijasse, and J. P. Dussauge. Analysis of Unsteadiness in Afterbody Transonic Flows. *AIAA Journal*, 42(12):2541–2550, dec 2004. ISSN 0001-1452. doi: 10.2514/1.7000.

M. Dharavath, P.K Sinha, and D. Chakraborty. Simulation of supersonic base flow: Effect of computational grid and turbulence model. *Proceedings of the Institution of Mechanical Engineers, Part G: Journal of Aerospace Engineering*, 224(3):311–319, 2010. doi: 10.1243/09544100JAERO600. URL https://doi.org/10.1243/09544100JAERO600.

D. M. Driver, H. L. Seegmiller, and J. G. Marvin. Time-dependent behaviour of a reattaching shear layer. *Aiaa J.*, 25(7):914–919, 1987. ISSN 0001-1452. doi: 10.2514/3.9722.

John K. Eaton and James P. Johnston. *Low Frequency Unsteadyness of a Reattaching Turbulent Shear Layer*, pages 162–170. Springer Berlin Heidelberg, Berlin, Heidelberg, 1982. ISBN 978-3-642-95410-8. doi: 10.1007/978-3-642-95410-8_16.

M. Frey and G. Hagemann. Restricted Shock Separation in Rocket Nozzles. *Journal of Propulsion and Power*, 16(3):478–484, 2000. doi: 10.2514/2.5593.

V. Gentile, F. F. J. Schrijer, B. W. van Oudheusden, and F. Scarano. Afterbody effects on axisymmetric base flows. *AIAA Journal*, 54(8):2285–2294, June 2016. doi: 10.2514/1.J054733. URL https://doi.org/10.2514/1.J054733.

R. H. M. Giepman, F. F. J. Schrijer, and B. W. van Oudheusden. High-resolution piv measurements of a transitional shock wave–boundary layer interaction. *Experiments in Fluids*, 56(6):113, May 2015. ISSN 1432-1114. doi: 10.1007/s00348-015-1977-8. URL https://doi.org/10.1007/s00348-015-1977-8.

R. Gurka, A. Liberzon, and D. Hefetz. Computation of pressure distribution using PIV velocity data. *Workshop on Particle*, 106(2):1–6, 1999. ISSN 16726820. doi: 10.1115/1.1631009.

R. Hain, C.J. Kähler, and C. Tropea. Comparison of ccd, cmos and intensified cameras. *Experiments in Fluids*, 42(3):403–411, Mar 2007. ISSN 1432-1114. doi: 10.1007/s00348-006-0247-1.

S. D. Hall, M. Behnia, C. A J Fletcher, and G. L. Morrison. Investigation of the secondary corner vortex in a benchmark turbulent backward-facing step using cross-correlation particle imaging velocimetry. *Experiments in Fluids*, 35(2):139–151, 2003. ISSN 07234864. doi: 10.1007/s00348-003-0626-9.

K. Hannemann, H. Lüdeke, and J.F. Pallegoix. Launch Vehicle Base Buffeting-Recent Experimental and Numerical Investigations. In *7th European Symposium on Aerothermodynamics for Space Vehicles*, Brugge, Belgium, 2011.

M. V. Herbert and R. J. Herd. Boundary-layer separation in supersonic propelling nozzles. *Aeronautical Research Council Reports And Memoranda*, (3421), August 1964.

J. L. Herrin and J. C. Dutton. Supersonic Base Flow Experiments in the Near Wake of a Cylindrical Afterbody. *AIAA Journal*, 32(1):77–83, 1994.

E. Hirschel. Vehicle Design and Critical Issues; FESTIP Technology Development Work in Aerothermodynamics for Reusable Launch Vehicles. In *ESA/ESTEC FESTIP Workshop*, Noordwijk, The Netherlands, 1996.

L.M. Hudy and A. Naguib. Stochastic estimation of a separated-flow field using wall-pressure-array measurements. *Physics of Fluids*, 19(2):1–22, 2007. ISSN 10706631. doi: 10.1063/1.2472507.

R.A. Humble. *Unsteady Flow Organization of a Shock Wave/Boundary Layer Interaction*. 2009. ISBN 9781600867712.

J. R. Janssen and J. C. Dutton. Time-series analysis of supersonic base-pressure fluctuations. *AIAA Journal*, 42(3):605–613, 3 2004. ISSN 0001-1452.

Y. J. Jeon, L. Chatellier, A. Beaudoin, and D. Laurent. Least-square reconstruction of instantaneous pressure field around a body based on a directly acquired material acceleration in time-resolved PIV. *11th International Symposium on Particle Image Velocimetry - PIV15*, (September), 2015.

U. K. Kaul and W. Frost. Turbulent atmospheric flow over a backward-facing step. *NASA Contractor Report 2749*, 1976.

J. Kim, S. J. Kline, and J. P. Johnston. Investigation of a reattaching turbulent shear layer Flow over a backward-facing step. 102:302–308, 1979.

LaVision GmbH. FlowMaster. 2012. URL http://www.lavision.de/de/download.php?id=317.

R.A. Lawrence. Symmetrical and unsymmetrical flow separation in supersonic nozzles. Research report number 67-1, Southern Methodist University, 1967.

T.H.H. Le. *Etude experimentale du couplage entre lecoulement transonique darriere-corps et les charges laterales dans les tuyeres propulsives*. Phd thesis, University of Poitiers, Dpt of Engineering Sciences,, 2005.

E. Loth, K. Kailasanath, and R. Loehner. Supersonic flow over an axisymmetric backward-facing step. *Journal of Spacecraft and Rockets*, 3:352–359, 1992.

P. Meliga and P. Reijasse. Unsteady Transonic Flow Behind An Axisymmetric Afterbody Equipped With Two Boosters. In *25th AIAA Applied Aerodynamics Conference*, Fluid Dynamics and Co-located Conferences, Reston, Virigina, jun 2007. American Institute of Aeronautics and Astronautics. ISBN 978-1-62410-006-2. doi: 10.2514/6.2007-4564.

A. Melling. Tracer particles and seeding for particle image velocimetry. *Measurement Science and Technology*, 8(12):1406, 1997. URL http://stacks.iop.org/0957-0233/8/i=12/a=005.

Nasa. *Oblique Shock Waves*. 2017. URL https://www.grc.nasa.gov/www/k-12/airplane/oblique.html.

NIST. National institute of standards and technology chemistry webbook, srd 69. URL http://webbook.nist.gov/cgi/cbook.cgi?ID=C7727379&Mask=4#Thermo-Phase.

H. Ottens, M. Gerritsma, and W. Bannink. Computational study of support influence on base flow of a model in supersonic flow. In *15th AIAA Computational Fluid Dynamics Conference*. American Institute of Aeronautics and Astronautics, 2001. doi: doi:10.2514/6.2001-2638. URL https://doi.org/10.2514/6.2001-2638.

B.W. van Oudheusden and F. Scarano. *PIV Investigation of Supersonic Base-Flow-Plume Interaction*, pages 465–474. Springer Berlin Heidelberg, Berlin, Heidelberg, 2008b. ISBN 978-3-540-73528-1. doi: 10.1007/978-3-540-73528-1_25. URL https://doi.org/10.1007/978-3-540-73528-1_25.

M. Pindzola. *Jet simulation in ground test facilities*, volume 79 of *AGARDograph ; 79*. North Atlantic Treaty Organization, Advisory Group for Aeronautical Research and Development, [Paris], 1963.

M. Raffel, C.E. Willert, S.T. Wereley, and J. Kompenhans. *Particle Image Velocimetry: A Practical Guide*. Springer-Verlag Berlin Heidelberg, second edition, 2007. ISBN 9783540723073.

D. Ragni, F. Schrijer, B. W. Van Oudheusden, and F. Scarano. Particle tracer response across shocks measured by PIV. *Experiments in Fluids*, 50(1):53–64, 2011. ISSN 07234864. doi: 10.1007/s00348-010-0892-2.

Daniele Ragni. *PIV-based load determination in aircraft propellers*. Phd thesis, Delft University of Technology, 2012.

P. Reijasse and J. Delery. Investigation of the Flow past the ARIANE 5 Launcher Afterbody. *Journal of Spacecraft and Rockets*, 31(2):208–214, 1994.

S. K. Robinson. Coherent Motions in the Turbulence Boundary Layer. *Annual Reviews of Fluid Mechanics*, 23:601–639, 1991. ISSN 00664189. doi: 10.1146/annurev.fluid.23.1.601.

F. Scarano. Experimental Aerodynamics. Course reader February, Delft University of Technology, Delft, 2013.

F. Scarano and M. L. Riethmuller. Iterative multigrid approach in PIV image processing with discrete window offset. *Experiments in Fluids*, 26(6):513–523, 1999. ISSN 07234864. doi: 10.1007/s003480050318.

F. Scarano, B.W. van Oudheusden, W.J. Bannink, and M. Bsibsi. Experimental investigation of supersonic base flow plume interaction by means of particle image velocimetry. In *Fifth European Symposium on Aerothermodynamics for Space Vehicles*, ESA Special Publication, page 601, 2005.

S. Scharnowski, V. Statnikov, M. Meinke, W. Schrder, and C. J. Khler. Combined experimental and numerical investigation of a transonic space launcher wake. In *EUCASS Proceedings Series Advances in AeroSpace Sciences*, volume 7, pages 311–328, 2015. doi: 10.1051/eucass/201507311.

S. Scharnowski, I. Bolgar, and C.J. Kähler. Investigation of a generic space launcher wake in sub- , trans- and supersonic conditions. *International Workshop on Non-intrusive Optical Flow Diagnostics*, (October), 2016a.

S. Scharnowski, I. Bolgar, and C.J. Khler. Characterization of Turbulent Structures in a Transonic Backward-Facing Step Flow. *Flow, Turbulence and Combustion*, 2016b.

F. F. J. Schrijer and F. Scarano. Effect of predictor–corrector filtering on the stability and spatial resolution of iterative piv interrogation. *Experiments in Fluids*, 45(5):927–941, Nov 2008. ISSN 1432-1114. doi: 10.1007/s00348-008-0511-7. URL https://doi.org/10.1007/s00348-008-0511-7.

F. F. J. Schrijer, F. Scarano, and B. W. van Oudheusden. Application of piv in a mach 7 double-ramp flow. *Experiments in Fluids*, 41(2):353–363, Aug 2006. ISSN 1432-1114. doi: 10.1007/s00348-006-0140-y.

F. F. J. Schrijer, A. Sciacchitano, and F. Scarano. Experimental investigation of flow control devices for the reduction of transonic buffeting on rocket afterbodies. *15th Int Symp on Applications of Laser Techniques to Fluid Mechanics*, July 2010.

F. F. J. Schrijer, A. Sciacchitano, and F. Scarano. Spatio-temporal and modal analysis of unsteady fluctuations in a high-subsonic base flow. *Physics of Fluids*, 26(8):086101, aug 2014. ISSN 1070-6631. doi: 10.1063/1.4891257.

F.F.J. Schrijer, A. Sciacchitano, F. Scarano, K. Hannemann, J.F. Pallegoix, J.E.J. Maseland, and R. Schwane. Experimental Investigation of Base Flow Buffeting on the Ariane 5 Launcher Using High Speed PIV. *7th European Symposium on Aerothermodynamics*, 7(1): 1689–1699, 2011. ISSN 1098-6596. doi: 10.1017/CBO9781107415324.004.

A. Sciacchitano and F. Scarano. Elimination of PIV light reflections via a temporal high pass filter. *Measurement Science and Technology*, 25(8):084009, 2014. ISSN 0957-0233. doi: 10.1088/0957-0233/25/8/084009.

A. Sciacchitano and B. Wieneke. Piv uncertainty propagation. *Measurement Science and Technology*, 27(8):084006, 2016. URL http://stacks.iop.org/0957-0233/27/i=8/a=084006.

G. S. Settles. *Schlieren and Shadowgraph Techniques: Visualizing Phenomena in Transparent Media*. Springer-Verlag Berlin and Heidelberg GmbH & Co, Berlin, 1st edition, 2001. ISBN 9783642630347. doi: 10.1007/978-3-642-56640-0.

F. Simon, S. Deck, A. Merlen, P. Guillen, and P. Sagaut. Numerical simulation of the compressible mixing layer past an axisymmetric trailing edge. *Journal of Fluid Mechanics*, 591(2007):215–253, 2007. ISSN 0022-1120. doi: 10.1017/S0022112007008129.

L. J. Souverein, B. W. van Oudheusden, and F. Scarano. Particle Image Velocimetry Based Loads Determination in Supersonic Flows. *AIAA Paper 2007 - 0050*, (January), 2007. doi: 10.2514/6.2007-50.

SpaceFlight101.com. Ariane 5 - va226 - launch profile. URL http://spaceflight101.com/ariane-5-va226/ariane-5-va226-launch-profile/.

P. G. Spazzini, G. Iuso, M. Onorato, N. Zurlo, and G. M. Di Cicca. Unsteady behavior of back-facing step flow. *Experiments in Fluids*, 30(5):551–561, 2001. ISSN 07234864. doi: 10.1007/s003480000234.

V. Statnikov, C. Glatzer, J.-H. Meis, M. Meinke, and W. Schroder. Numerical investigation of the near wake of generic space launcher systems at transonic and supersonic flows. In Array, editor, *EUCASS Proceedings Series Advances in AeroSpace Sciences*, volume 5, pages 191–208, 2013. doi: 10.1051/eucass/201305191. URL https://doi.org/10.1051/eucass/201305191.

V. Statnikov, S. Stephan, K. Pausch, M. Meinke, R. Radespiel, and W. Schröder. Experimental and numerical investigations of the turbulent wake flow of a generic space launcher at $M_\infty = 3$ and $M_\infty = 6$. *CEAS Space Journal*, 8(2):101–116, 2016. ISSN 1868-2510. doi: 10.1007/s12567-016-0112-x.

Fred Stern, Marian Muste, Maria-laura Beninati, and William E Eichinger. Summary of Experimental Uncertainty. (406):37, 1999.

M. Summerfield, C. Foster, and W. Swan. Flow Separation in Overexpanded Supersonic Exhaust Nozzles. *Jet Propulsion*, 24(9):319321, 1954.

Z. Sun. *Micro Ramps in Supersonic Turbulent Boundary Layers: An experimental and numerical study*. 2014. ISBN urn:isbn:9789461919243. URL http://repository.tudelft.nl/view/ir/uuid:6e1a39dd-1581-4d87-b623-97d1dc39fb78/.

G.P. Sutton and O. Bibarz. *Rocket Propulsion Elements*. John Wiley & Sons Inc, seventh edition, 2001. ISBN 0-471-32642-9.

C. Tropea, A.L. Yarin, and J.F. Foss. *Springer handbook of experimental fluid mechanics*, volume 53. Springer-Verlag Berlin Heidelberg, 2007. ISBN 9783540251415; 3540251413. doi: 10.1007/978-3-540-30299-5.

T. R. Troutt, B. Scheelke, and T. R. Norman. Organized structures in a reattaching separated flow field. *Journal of Fluid Mechanics*, 143:413427, 1984. doi: 10.1017/S0022112084001415.

P. L. van Gent, D. Michaelis, B. W. van Oudheusden, P. É. Weiss, R. de Kat, A. Laskari, Y. J. Jeon, L. David, D. Schanz, F. Huhn, S. Gesemann, M. Novara, C. McPhaden, N. J. Neeteson, D. E. Rival, J. F. G. Schneiders, and F. F. J. Schrijer. Comparative assessment of pressure field reconstructions from particle image velocimetry measurements and lagrangian particle tracking. *Experiments in Fluids*, 58(4):33, Mar 2017. ISSN 1432-1114. doi: 10.1007/s00348-017-2324-z. URL https://doi.org/10.1007/s00348-017-2324-z.

P.L. van Gent, F.F.J. Schrijer, and B.W. van Oudheusden. Determination of mean pressure from PIV in compressible flows using the Reynolds-averaging approach. 2017b.

B. W. Van Oudheusden. Principles and application of velocimetry-based planar pressure imaging in compressible flows with shocks. *Experiments in Fluids*, 45(4):657–674, 2008a. ISSN 07234864. doi: 10.1007/s00348-008-0546-9.

B. W. van Oudheusden. PIV-based pressure measurement. *Measurement Science and Technology*, 24(3):032001, 2013. ISSN 0957-0233. doi: 10.1088/0957-0233/24/3/032001.

B. W. van Oudheusden, F. Scarano, E. W. M. Roosenboom, E. W. F. Casimiri, and L. J. Souverein. Evaluation of integral forces and pressure fields from planar velocimetry data for incompressible and compressible flows. *Experiments in Fluids*, 43(2-3):153–162, aug 2007. ISSN 0723-4864. doi: 10.1007/s00348-007-0261-y.

S.B. Verma. Study of Flow Separation in Truncated Ideal Contour Nozzle. *Journal of Propulsion and Power*, 18(5):1112–1121, 2002. doi: 10.2514/2.6042.

P.-E. Weiss and S. Deck. Control of the antisymmetric mode (m=1) for high Reynolds axisymmetric turbulent separating/reattaching flow. *Physics of Fluids*, (23), 2011. ISSN 10706631. doi: 10.1063/1.3614481.

P.-E. Weiss, S. Deck, J-C. Robinet, and P. Sagaut. On the dynamics of axisymmetric turbulent separating/reattaching flows. *Physics of Fluids*, 21(7):075103, 2009. ISSN 10706631. doi: 10.1063/1.3177352.

J. Westerweel. Fundamentals of digital particle image velocimetry. *Measurement Science and Technology*, 8(12):1379–1392, 1997. ISSN 0957-0233. doi: 10.1088/0957-0233/8/12/002.

F.M. White. *Viscous fluid flow*. McGraw-Hill International Edition, international edition edition, 2005.

C. D. Winant and F. K. Browand. Vortex pairing : the mechanism of turbulent mixing-layer growth at moderate reynolds number. *Journal of Fluid Mechanics*, 63(2):237255, 1974. doi: 10.1017/S0022112074001121.

C.C. Wolf, C.E. Klei, R.M. Buffo, R. Hrnschemeyer, and E. Stumpf. Comparison of rocket near-wakes with and without nozzle simulation in subsonic freestream conditions. In *42nd AIAA Fluid Dynamics Conference and Exhibit*, pages 1–18. American Institute of Aeronautics and Astronautics, 2012. ISBN 978-1-60086-933-4.

B.T.C. Zandbergen. AE4S01-Thermal Rocket Propulsion (version 2.05). Course reader February, Delft University of Technology, Delft, 2016.

Appendix A

Appendix A

A.1 Ariane 5 Velocity Profile

Altitude [m]	Velocity [m/s]	Temperature [K]	Pressure [Pa]	a [m/s]	Mach
0	0	288,15	101325	340,3	0
100	38,6	287,5	100129,4	339,9	0,11
200	56,9	286,85	98945,2	339,5	0,17
300	69,8	286,2	97772,4	339,1	0,21
400	81,4	285,55	96610,9	338,8	0,24
500	91,9	284,9	95460,6	338,4	0,27
600	101,4	284,25	94321,4	338,0	0,3
700	110,0	283,6	93193,2	337,6	0,33
800	117,9	282,95	92076,0	337,2	0,35
900	125,3	282,3	90969,7	336,8	0,37
1000	132,4	281,65	89874,1	336,4	0,39
1100	139,2	281	88789,3	336,0	0,41
1200	145,8	280,35	87715,0	335,7	0,43
1300	152,2	279,7	86651,4	335,3	0,45
1400	158,4	279,05	85598,2	334,9	0,47
1500	164,4	278,4	84555,4	334,5	0,49
1600	170,1	277,75	83522,9	334,1	0,51
1700	175,7	277,1	82500,6	333,7	0,53
1800	181,0	276,45	81488,5	333,3	0,54
1900	186,2	275,8	80486,4	332,9	0,56
2000	191,2	275,15	79494,4	332,5	0,57
2100	196,0	274,5	78512,3	332,1	0,59
2200	200,7	273,85	77540,0	331,7	0,6
2300	205,1	273,2	76577,5	331,4	0,62
2400	209,5	272,55	75624,7	331,0	0,63
2500	213,7	271,9	74681,6	330,6	0,65
2600	217,7	271,25	73747,9	330,2	0,66
2700	221,5	270,6	72823,8	329,8	0,67
2800	225,3	269,95	71909,0	329,4	0,68
2900	228,9	269,3	71003,6	329,0	0,7
3000	232,3	268,65	70107,4	328,6	0,71
3100	235,7	268	69220,5	328,2	0,72
3200	238,9	267,35	68342,6	327,8	0,73
3300	242,1	266,7	67473,7	327,4	0,74
3400	245,1	266,05	66613,9	327,0	0,75
3500	248,1	265,4	65762,9	326,6	0,76
3600	251,0	264,75	64920,7	326,2	0,77
3700	253,8	264,1	64087,3	325,8	0,78
3800	256,5	263,45	63262,6	325,4	0,79
3900	259,2	262,8	62446,5	325,0	0,8
4000	261,7	262,15	61638,9	324,6	0,81
4100	264,3	261,5	60839,8	324,2	0,82
4200	266,7	260,85	60049,2	323,8	0,82
4300	269,1	260,2	59266,8	323,4	0,83
4400	271,4	259,55	58492,8	323,0	0,84
4500	273,7	258,9	57726,9	322,6	0,85
4600	275,9	258,25	56969,2	322,2	0,86
4700	278,1	257,6	56219,6	321,8	0,86
4800	280,3	256,95	55478,0	321,3	0,87

4900	282,5	256,3	54744,3	320,9	0,88
5000	284,6	255,65	54018,5	320,5	0,89
5100	286,7	255	53300,5	320,1	0,9
5200	288,8	254,35	52590,2	319,7	0,9
5300	290,9	253,7	51887,6	319,3	0,91
5400	293,0	253,05	51192,7	318,9	0,92
5500	295,1	252,4	50505,3	318,5	0,93
5600	297,2	251,75	49825,4	318,1	0,93
5700	299,3	251,1	49152,9	317,7	0,94
5800	301,5	250,45	48487,8	317,3	0,95
5900	303,6	249,8	47830,0	316,8	0,96
6000	305,8	249,15	47179,5	316,4	0,97
6100	308,1	248,5	46536,1	316,0	0,97
6200	310,4	247,85	45899,9	315,6	0,98
6300	312,7	247,2	45270,7	315,2	0,99
6400	315,1	246,55	44648,5	314,8	1
6500	317,5	245,9	44033,3	314,4	1,01
6600	320,0	245,25	43424,9	313,9	1,02
6700	322,6	244,6	42823,4	313,5	1,03
6800	325,2	243,95	42228,6	313,1	1,04
6900	327,8	243,3	41640,6	312,7	1,05
7000	330,4	242,65	41059,2	312,3	1,06
7100	333,1	242	40484,3	311,9	1,07
7200	335,8	241,35	39916,1	311,4	1,08
7300	338,5	240,7	39354,3	311,0	1,09
7400	341,2	240,05	38798,9	310,6	1,1
7500	344,0	239,4	38249,8	310,2	1,11
7600	346,7	238,75	37707,1	309,8	1,12
7700	349,5	238,1	37170,7	309,3	1,13
7800	352,3	237,45	36640,4	308,9	1,14
7900	355,1	236,8	36116,3	308,5	1,15
8000	357,9	236,15	35598,2	308,1	1,16
8100	360,8	235,5	35086,2	307,6	1,17
8200	363,6	234,85	34580,2	307,2	1,18
8300	366,5	234,2	34080,1	306,8	1,19
8400	369,4	233,55	33585,9	306,4	1,21
8500	372,3	232,9	33097,5	305,9	1,22
8600	375,2	232,25	32614,8	305,5	1,23
8700	378,2	231,6	32137,9	305,1	1,24
8800	381,1	230,95	31666,6	304,7	1,25
8900	384,1	230,3	31201,0	304,2	1,26
9000	387,1	229,65	30740,9	303,8	1,27
9100	390,1	229	30286,3	303,4	1,29
9200	393,1	228,35	29837,2	302,9	1,3
9300	396,1	227,7	29393,5	302,5	1,31
9400	399,2	227,05	28955,1	302,1	1,32
9500	402,2	226,4	28522,1	301,6	1,33
9600	405,3	225,75	28094,3	301,2	1,35
9700	408,4	225,1	27671,7	300,8	1,36
9800	411,5	224,45	27254,3	300,3	1,37

9900	414,6	223,8	26842,0	299,9	1,38
10000	417,7	223,15	26434,8	299,5	1,39
10100	420,8	222,5	26032,5	299,0	1,41
10200	424,0	221,85	25635,3	298,6	1,42
10300	427,1	221,2	25243,0	298,2	1,43
10400	430,3	220,55	24855,5	297,7	1,45
10500	433,5	219,9	24472,9	297,3	1,46
10600	436,7	219,25	24095,0	296,8	1,47
10700	439,9	218,6	23721,9	296,4	1,48
10800	443,1	217,95	23353,5	296,0	1,5
10900	446,3	217,3	22989,8	295,5	1,51
11000	449,5	216,65	22630,6	295,1	1,52
11100	452,8	216,65	22276,6	295,1	1,53
11200	456,0	216,65	21928,1	295,1	1,55
11300	459,3	216,65	21585,0	295,1	1,56
11400	462,5	216,65	21247,3	295,1	1,57
11500	465,8	216,65	20914,9	295,1	1,58
11600	469,1	216,65	20587,7	295,1	1,59
11700	472,4	216,65	20265,6	295,1	1,6
11800	475,7	216,65	19948,5	295,1	1,61
11900	479,0	216,65	19636,4	295,1	1,62
12000	482,3	216,65	19329,2	295,1	1,63
12100	485,6	216,65	19026,8	295,1	1,65
12200	488,9	216,65	18729,1	295,1	1,66
12300	492,2	216,65	18436,1	295,1	1,67
12400	495,6	216,65	18147,7	295,1	1,68
12500	498,9	216,65	17863,8	295,1	1,69
12600	502,3	216,65	17584,3	295,1	1,7
12700	505,6	216,65	17309,2	295,1	1,71
12800	509,0	216,65	17038,4	295,1	1,72
12900	512,3	216,65	16771,8	295,1	1,74
13000	515,7	216,65	16509,4	295,1	1,75
13100	519,1	216,65	16251,2	295,1	1,76
13200	522,4	216,65	15996,9	295,1	1,77
13300	525,8	216,65	15746,6	295,1	1,78
13400	529,2	216,65	15500,3	295,1	1,79
13500	532,6	216,65	15257,8	295,1	1,8
13600	536,0	216,65	15019,1	295,1	1,82
13700	539,4	216,65	14784,1	295,1	1,83
13800	542,9	216,65	14552,8	295,1	1,84
13900	546,3	216,65	14325,1	295,1	1,85
14000	549,8	216,65	14101,0	295,1	1,86
14100	553,3	216,65	13880,4	295,1	1,88
14200	556,8	216,65	13663,3	295,1	1,89
14300	560,3	216,65	13449,5	295,1	1,9
14400	563,9	216,65	13239,1	295,1	1,91
14500	567,4	216,65	13032,0	295,1	1,92
14600	571,0	216,65	12828,1	295,1	1,94
14700	574,6	216,65	12627,4	295,1	1,95
14800	578,2	216,65	12429,8	295,1	1,96

14900	581,9	216,65	12235,4	295,1	1,97
15000	585,5	216,65	12043,9	295,1	1,98
15100	589,2	216,65	11855,5	295,1	2
15200	592,9	216,65	11670,0	295,1	2,01
15300	596,6	216,65	11487,5	295,1	2,02
15400	600,3	216,65	11307,7	295,1	2,03
15500	604,0	216,65	11130,8	295,1	2,05
15600	607,8	216,65	10956,7	295,1	2,06
15700	611,6	216,65	10785,3	295,1	2,07
15800	615,3	216,65	10616,5	295,1	2,09
15900	619,1	216,65	10450,4	295,1	2,1
16000	623,0	216,65	10286,9	295,1	2,11
16100	626,8	216,65	10126,0	295,1	2,12
16200	630,6	216,65	9967,6	295,1	2,14
16300	634,5	216,65	9811,6	295,1	2,15
16400	638,4	216,65	9658,1	295,1	2,16
16500	642,3	216,65	9507,0	295,1	2,18
16600	646,2	216,65	9358,3	295,1	2,19
16700	650,1	216,65	9211,9	295,1	2,2
16800	654,0	216,65	9067,8	295,1	2,22
16900	657,9	216,65	8925,9	295,1	2,23
17000	661,9	216,65	8786,3	295,1	2,24
17100	665,9	216,65	8648,8	295,1	2,26
17200	669,9	216,65	8513,5	295,1	2,27
17300	673,8	216,65	8380,3	295,1	2,28
17400	677,9	216,65	8249,2	295,1	2,3
17500	681,9	216,65	8120,1	295,1	2,31
17600	685,9	216,65	7993,1	295,1	2,32
17700	690,0	216,65	7868,1	295,1	2,34
17800	694,0	216,65	7745,0	295,1	2,35
17900	698,1	216,65	7623,8	295,1	2,37
18000	702,2	216,65	7504,5	295,1	2,38
18100	706,3	216,65	7387,1	295,1	2,39
18200	710,4	216,65	7271,5	295,1	2,41
18300	714,5	216,65	7157,8	295,1	2,42
18400	718,6	216,65	7045,8	295,1	2,44
18500	722,7	216,65	6935,6	295,1	2,45
18600	726,9	216,65	6827,1	295,1	2,46
18700	731,1	216,65	6720,2	295,1	2,48
18800	735,2	216,65	6615,1	295,1	2,49
18900	739,4	216,65	6511,6	295,1	2,51
19000	743,6	216,65	6409,7	295,1	2,52
19100	747,8	216,65	6309,5	295,1	2,53
19200	752,0	216,65	6210,8	295,1	2,55
19300	756,2	216,65	6113,6	295,1	2,56
19400	760,4	216,65	6017,9	295,1	2,58
19500	764,7	216,65	5923,8	295,1	2,59
19600	768,9	216,65	5831,1	295,1	2,61
19700	773,2	216,65	5739,9	295,1	2,62
19800	777,4	216,65	5650,1	295,1	2,63

19900	781,7	216,65	5561,7	295,1	2,65
20000	786,0	216,65	5474,7	295,1	2,66
20100	790,3	216,75	5389,0	295,1	2,68
20200	794,6	216,85	5304,7	295,2	2,69
20300	798,9	216,95	5221,7	295,3	2,71
20400	803,2	217,05	5140,0	295,3	2,72
20500	807,5	217,15	5059,6	295,4	2,73
20600	811,8	217,25	4980,5	295,5	2,75
20700	816,1	217,35	4902,5	295,5	2,76
20800	820,5	217,45	4825,8	295,6	2,78
20900	824,8	217,55	4750,3	295,7	2,79
21000	829,2	217,65	4676,0	295,8	2,8
21100	833,5	217,75	4602,9	295,8	2,82
21200	837,9	217,85	4530,9	295,9	2,83
21300	842,3	217,95	4460,0	296,0	2,85
21400	846,6	218,05	4390,2	296,0	2,86
21500	851,0	218,15	4321,5	296,1	2,87
21600	855,4	218,25	4253,9	296,2	2,89
21700	859,8	218,35	4187,4	296,2	2,9
21800	864,2	218,45	4121,8	296,3	2,92
21900	868,6	218,55	4057,4	296,4	2,93
22000	873,0	218,65	3993,9	296,4	2,95
22100	877,4	218,75	3931,4	296,5	2,96
22200	881,8	218,85	3869,9	296,6	2,97
22300	886,2	218,95	3809,3	296,6	2,99

Appendix B

Appendix B

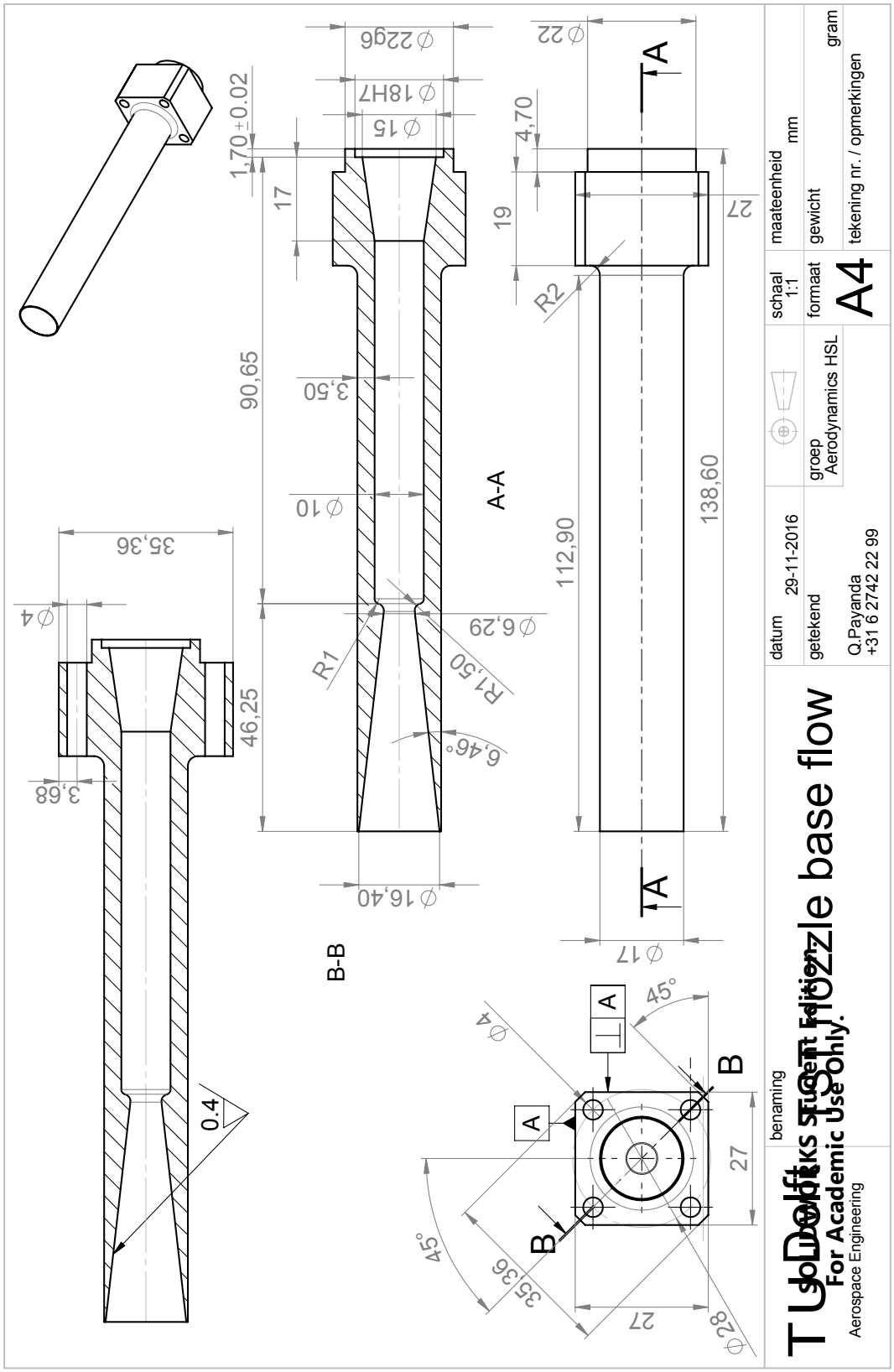
A-A
B-B
90,65
46,25
35,36
3,68
112,90
138,60
27
19
4,70
17
1,70±0.02
3,50
6,46°
R1
R1,50
R2
45°
35,36
0.4
benaming
datum 29-11-2016
getekend Q.Payanda
+31 6 2742 22 99
groep Aerodynamics HSL
schaal 1:1
formaat A4
maateenheid mm
gewicht gram
tekening nr. / opmerkingen
TU Delft
Aerospace Engineering
For Academic Use Only.
Nozzle base flow

Appendix C

Appendix C

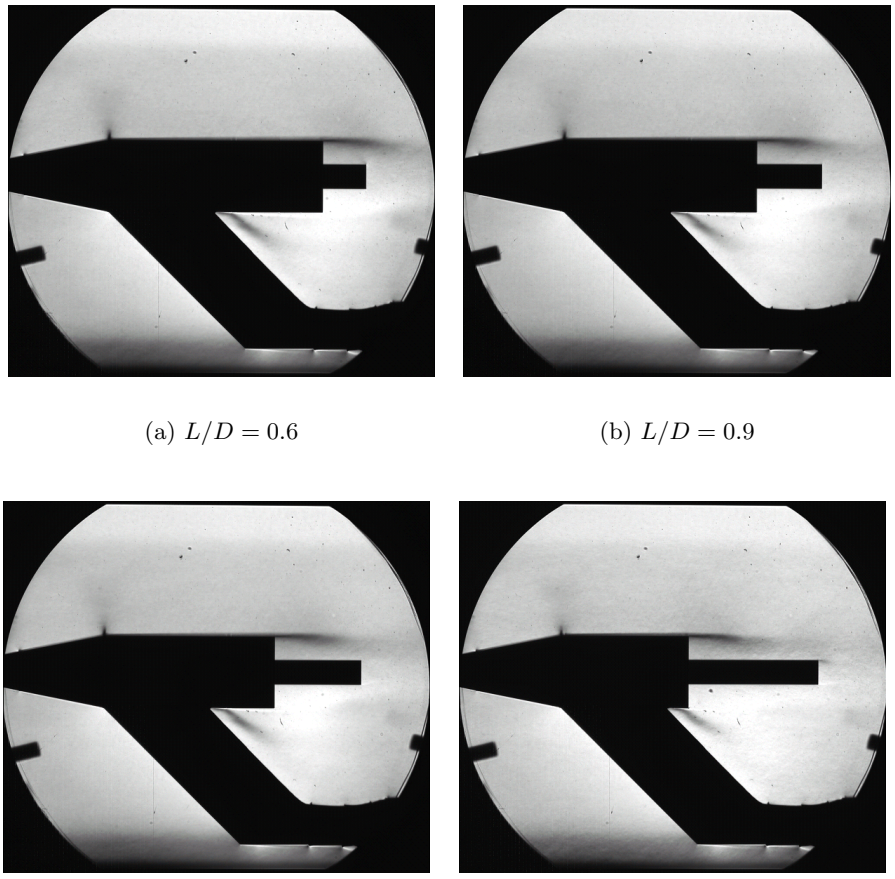

(a) $L/D = 0.6$ (b) $L/D = 0.9$

(c) $L/D = 1.2$ (d) $L/D = 1.8$

Figure C.1: Schlieren mean flow field results at $M_\infty = 0.7$, $p_0 = 2.0$ bar and $p_{0,jet} = 0$ bar

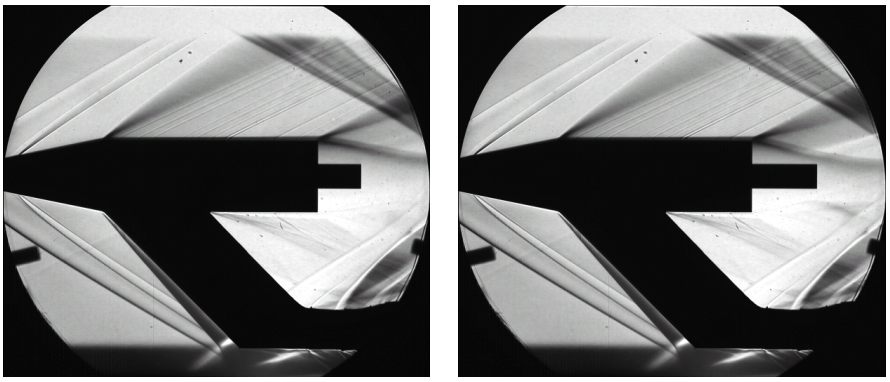

(a) $L/D = 0.6$ (b) $L/D = 0.9$

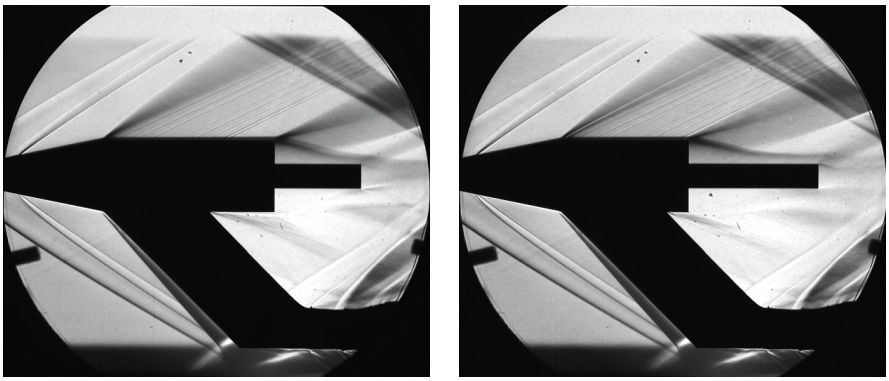

(c) $L/D = 1.2$ (d) $L/D = 1.8$

Figure C.2: Schlieren mean flow field results at $M_\infty = 2.2$, $p_0 = 2.5$ bar and $p_{0,jet} = 0$ bar